UNIVERSITY OF OKLAHOMA
GRADUATE COLLEGE

SUBSURFACE AND EXPERIMENTAL ANALYSES OF FRACTURES AND CURVATURE

A THESIS

SUBMITTED TO THE GRADUATE FACULTY

in partial fulfillment of the requirements for the

Degree of

MASTER OF SCIENCE

By

EVAN RICHARD STAPLES
Norman, Oklahoma
2011

SUBSURFACE AND EXPERIMENTAL ANALYSES
OF FRACTURES AND CURVATURE

A THESIS APPROVED FOR THE
CONOCOPHILLIPS SCHOOL OF GEOLOGY AND GEOPHYSICS

BY

____
Dr. Kurt J. Marfurt, Co-Chair

____
Dr. Ze'ev Reches, Co-Chair

____
Dr. Neil H. Suneson

Acknowledgements

Many people helped me along the path to graduation and I am extremely grateful for all they did to help. First, I acknowledge the love and support of my wife during the entire process and her hours of tireless editing on my thesis. She was beside me the entire way and never complained when I had to pull many "all-nighters." I am also very thankful to my advisors, Dr. Kurt Marfurt and Dr. Ze'ev Reches, for their guidance during the past two years. They have encouraged me to challenge myself and achieve things I never thought were possible. I would also like to acknowledge Oswaldo Davogustto, Roderick Perez, Ana Martins, Marcelo Sanchez, Nabanita Gupta, Debapriya Paul, and all the many other CPSGG fellow students and staff who encouraged and helped me along the way. They are all so talented and have so many different areas of expertise and knowledge, providing a wonderful resource when I did not know the answer. I would like to acknowledge the generous financial support of ConocoPhillips through the ConocoPhillips Fellowship, which funded my tuition and research for the academic years of 2009-2010 and 2010-2011. Pathfinder Exploration, LLC was very kind and provided the subsurface database for this project. Lastly, the Lord has blessed me with strength, wisdom, and the ability to comprehend the subject matter. "Trust in the Lord with all thine heart; and lean not unto thine own understanding. In all thy ways acknowledge him, and he shall direct thy paths" Proverbs 3:5-6.

Table of Contents

List of Tables

List of Figures

ABSTRACT

Layer curvature is often used as a proxy for fracture intensity (FI) in subsurface-seismic analyses. Theoretical beam-bending calculations suggest a linear relationship between curvature and strain (assumed fracture intensity). Clay models, horizontal-borehole-image logs, and 3D-seismic data provide a database to view curvature and fracturing at multiple scales and stages of deformation. Compression (thrust faulting) and extension (normal faulting) were modeled in clay experiments and showed strong linear relationships between fracture intensities (total fracture length/area) and curvature.

I analyzed 3D-seismic data from a nine-mi^2 area in central Oklahoma and the image logs of seven horizontal wells drilled into the Hunton Group in the same area. Curvature calculated from bedding-planes seen on horizontal-borehole-image logs follows similar trends as curvature calculated from 3D-seismic reflectors on wells with bedding-plane measurements. Relative fracture density (number of fractures per length) as determined in the horizontal-borehole-image logs showed correlations with azimuthally-limited curvature measures computed from 3D-seismic data consistent with my hypothesis that high fracture densities are located in areas of high curvature. Results from 3D-seismic data and the clay model experiments support the use of layer curvature as an indicator for FI in subsurface analysis.

INTRODUCTION

The flexural slip/flow folding model (e.g., Van Der Pluijm and Marshak, 2004) indicates that high strain is developed at the top of folded layers (Fig. 1), which can cause tensile fractures to form parallel to the fold axis (Einstein and Dershowitz, 1990). Although fractures are often critical to porosity and permeability in hydrocarbon reservoirs, Al-Dossary and Marfurt (2006) suggest that direct detection of fractures falls below traditional seismic resolution. To overcome this difficulty, the presence of fracture zones in the subsurface is often deduced from 3D-seismic data by structural curvature analysis of the target horizons (Chopra and Marfurt, 2010). Another method to overcome seismic resolution issues is to identify fractures in outcrop studies, calculate curvature from bedding plane orientations, and then use those measurements as an analog for subsurface features (Hennings et al., 2000).

My goal is to develop a workflow to enable fracture zone identification using the curvature attribute calculated from 3D-seismic data. Other methods for fracture detection are important and will be mentioned in the seismic analysis section, but the focus of this thesis is layer curvature and how it applies to fracture density. In order to accomplish this, I used clay models, horizontal-borehole-image logs, and 3D-seismic data to analyze the relationship between fracture density and curvature intensity. Clay models are used to identify fold mechanics and related fracturing in both extensional and compressional structures during which continuous curvature and fracture development can be observed. These models then served as analogs for what I assume is found in the subsurface.

Horizontal-borehole-image logs provided quantitative fracture data in the target horizon. Apparent curvature (curvature in a specified azimuth) calculated from bedding-planes in the horizontal-borehole-image logs allowed me to compare curvature from 3D-seismic data to "real" curvature from rocks. Lastly, cross-correlating curvature calculated from 3D-seismic data and fracture densities from horizontal-borehole-image logs provided an opportunity to calibrate 3D-seismic data with subsurface fracture zones, which overcame the issue of fractures being smaller than seismic resolution.

I first discuss the mechanical behavior of bending plates and beams from crustal scale to laboratory models. The strain associated with layer bending is described in these studies in association with fracturing or damage where it is identified. Next, I review previous studies that identified fractures or fracture zones by applying curvature to either outcrop or 3D-seismic data. I then describe clay model experiments in this study and resulting correlations between fracture intensity and curvature measurements. Next, I explain fracture identification and curvature calculations in the horizontal-borehole-image logs and how borehole curvature relates to 3D-seismic curvature. Then I cross-correlate curvature from 3D-seismic data to fracture densities in the horizontal-borehole-image logs and identify areas where both fracture densities and curvature are high. Lastly, I synthesize all the data from this study (clay models, horizontal-borehole-image logs, and 3D-seismic data) and discuss my results.

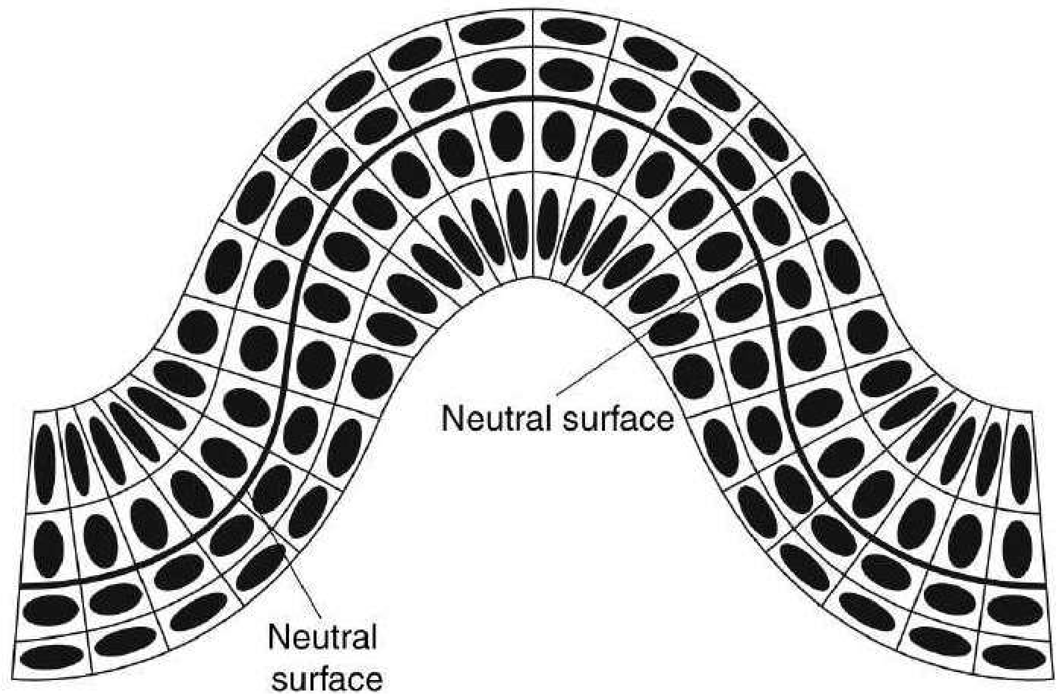

Fig. 1 – Flexural slip/flow folding model where extension occurs on the top of folds (ellipse elongation), while compression occurs in the center of folds (ellipse compression). After Van der Pluijm and Marshak (2004).

EXPERIMENTAL BACKGROUND

Understanding forces that bend and buckle rocks is an important background for layer curvature prediction of tensile-fracture zones in the subsurface. Here I report five experimental studies that illustrate the stresses and strains associated with plate or beam bending, including three that induce tensile fractures. Experimental materials include theoretical plates, rock beams, PMMA (polymethyl methacrylate), and numerical simulations of rock beams.

STRESS/STRAIN BENDING PLATES

Plate and beam bending stresses have been analyzed since Euler days in the 19th century. For the sake of convenience, I follow the derivation of Manaker et al. (2007). They calculated damage associated with bending under a constant moment (Fig. 2) in an infinite plate. Where E is Young's Modulus, v is Poisson's ratio, h is plate thickness, w is deflection (or bending) at any point along the plate, $D = -Ew/12(1-v^2)$ is the modulus of rigidity of the plate, x is the horizontal position along the plate of length L from $0 \leq x \leq L$, and M_o is the moment of the beam. The moment, M_o is then related to the curvature, $k = d^2w/dx^2$ as:

$$M_o = \frac{Eh^2}{12(1-v^2)}\frac{d^2w}{dx^2} = D\frac{d^2w}{dx^2} = Dk \tag{1}$$

where here I have changed the signs of Manaker et al.'s (2007) stress to be positive for compression as used in geology and petroleum engineering. Deflection w or amount of bending along the plate relates to the moment M_o, as:

$$w = \frac{M_o x^2}{2D} \tag{2}$$

Strain (ε_{xx}) in the x direction is related to the bending moment, where y is the vertical distance from the neutral surface in the plate of thickness h between $-h/2 < y < h/2$, by:

$$\varepsilon_{xx} = y\frac{d^2w}{dx^2} = y\frac{M_o}{D} \tag{3}$$

The radius of curvature of the bending plate is:

$$R_c = \frac{1}{\frac{d^2w}{dx^2}} = \frac{1}{k} \tag{4}$$

Substituting eq. 4 into eq. 3 yields:

$$\varepsilon_{xx} = \frac{y}{R_c} = yk \tag{5}$$

Eq. 5 presents the linear dependence of theoretical strain and radii of curvature relative to the position in the plate. It is further observed that the outer area of the bent plate undergoes extension (Fig. 2). In the rest of this study, it is hypothesized that fracture intensity is controlled by high strains generated during this extension.

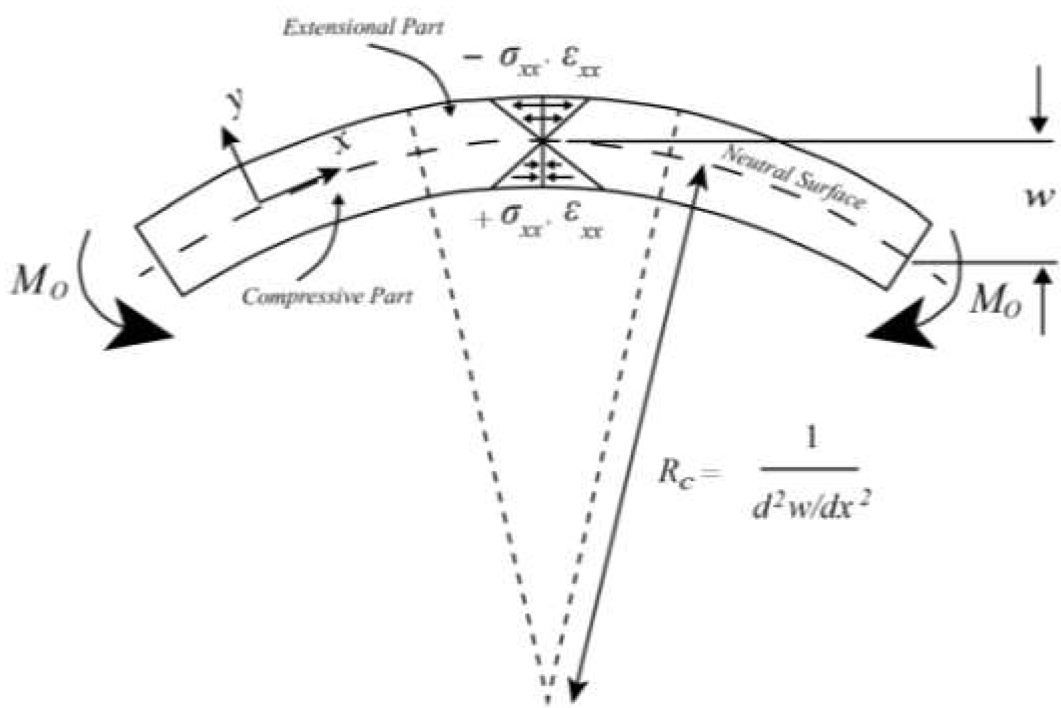

Fig. 2 – Plate bending under constant moment. After Manaker et al. (2007)

ROCK BEAMS

Handin et al. (1972) used a screw-driven rock deformation apparatus to buckle single-layer beams of limestone and sandstone under confining pressure. Sandstone samples did not buckle, but failed by shear fracturing near the end of the beams. Limestone samples folded, and many formed two synclines and a central anticline. Four types of fractures (A, B, C and D) were mapped in deformed beams (Fig. 3), where fracture types A and B were most prevalent. Type A fractures nucleated in compressive zones and eventually propagated to transect the entire beam. Type B fractures only occurred on the tensile zones of the anticlines and synclines. Type C fractures were parallel to or conjugate to faults that developed in a few experiments. Type D fractures occur on the compressive side of thin beams and are inclined at 0° to 30° to the lower surface.

Stearns (1968) identified five fracture types in natural folds (Fig. 4). Handin et al. (1972) correlated the experimental fractures to fractures on natural folds with type B experimental fractures correlating to fracture set 2 and 3 on natural folds (Fig. 4). Type D fractures are parallel to fracture set 3, while type C fractures correlate with fracture set 4 (Fig. 4). Experimental results did not produce fracture sets 1 and 5.

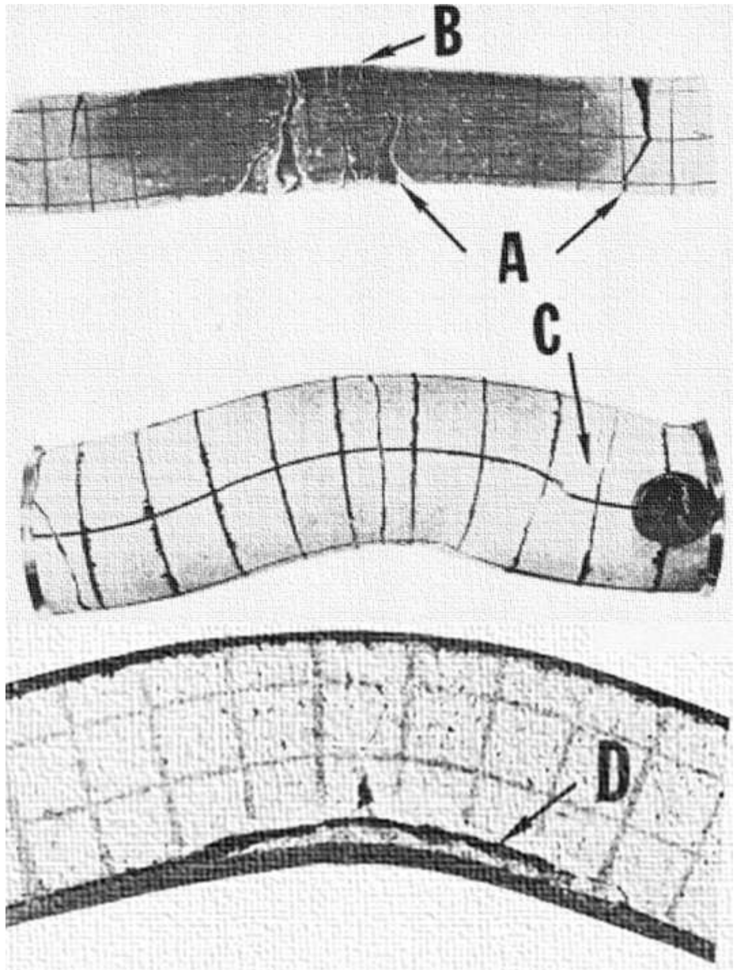

Fig. 3 – Fracture (A, B, C and D) in beams of limestone bent under confining pressure. After Handin et al. (1972).

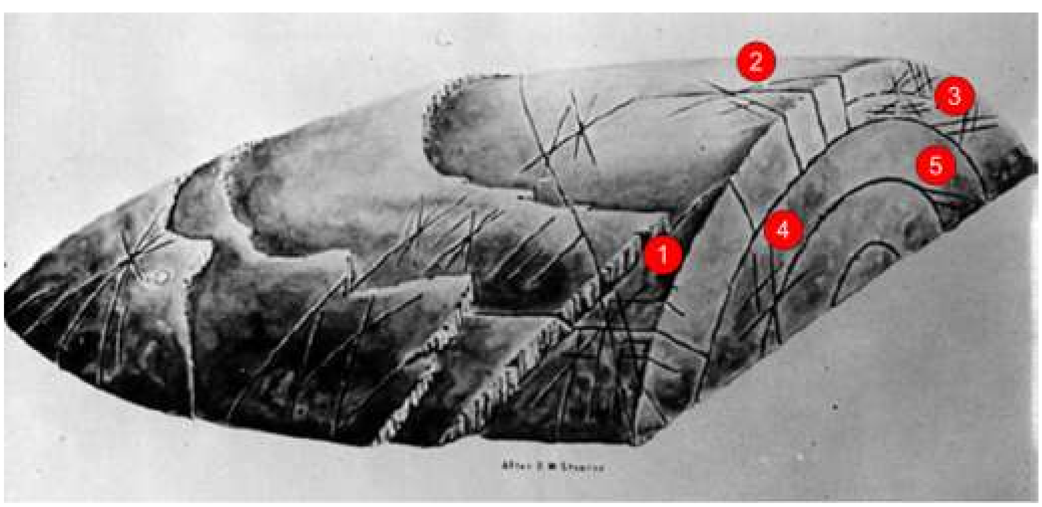

Fig. 4 – Schematic model showing different fracture sets identified in a natural fold. After Stearns (1968).

PLATE BENDING OF PMMA

Wu and Pollard (1995) studied the bending related fracturing in a PMMA (polymethyl methacrylate) plate. They coated the PMMA by brittle methylene chloride and loaded it by a four point-bending apparatus (Fig. 5). This loading is assumed to generate uniform-extensional strain on the top of the brittle coating (Fig. 5). Wu and Pollard (1995) observed that the fractures initiated at the edges and propagated toward the interior of the sample. Fracture distribution appears relatively uniform (Fig. 6) with fracture saturation reached at strain of -3.8×10^{-3}. These fractures in the brittle coating are analog to tensile fractures on top of an anticline in a natural fold (Lisle, 1994).

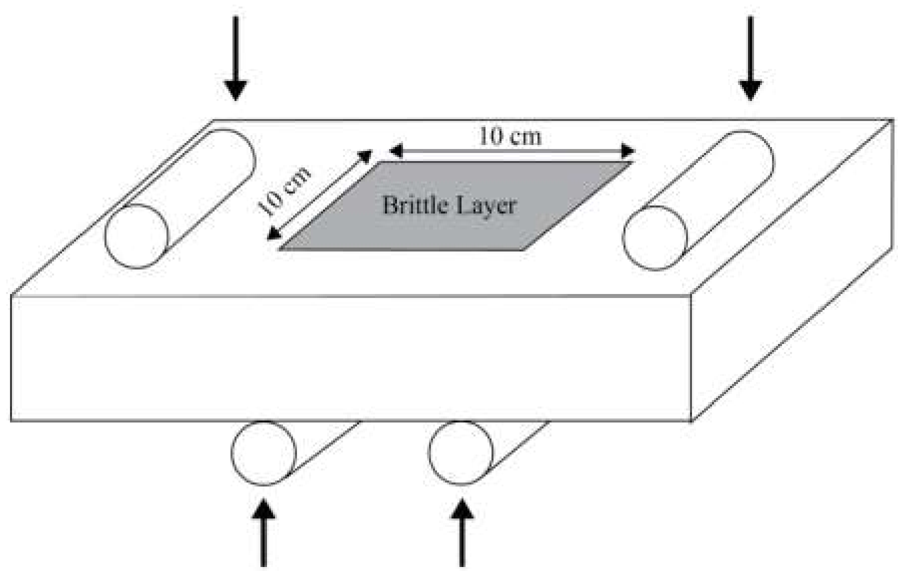

Fig. 5 – Schematic of four-point beam bending apparatus used to deform a brittle layer. After Wu and Pollard (1995).

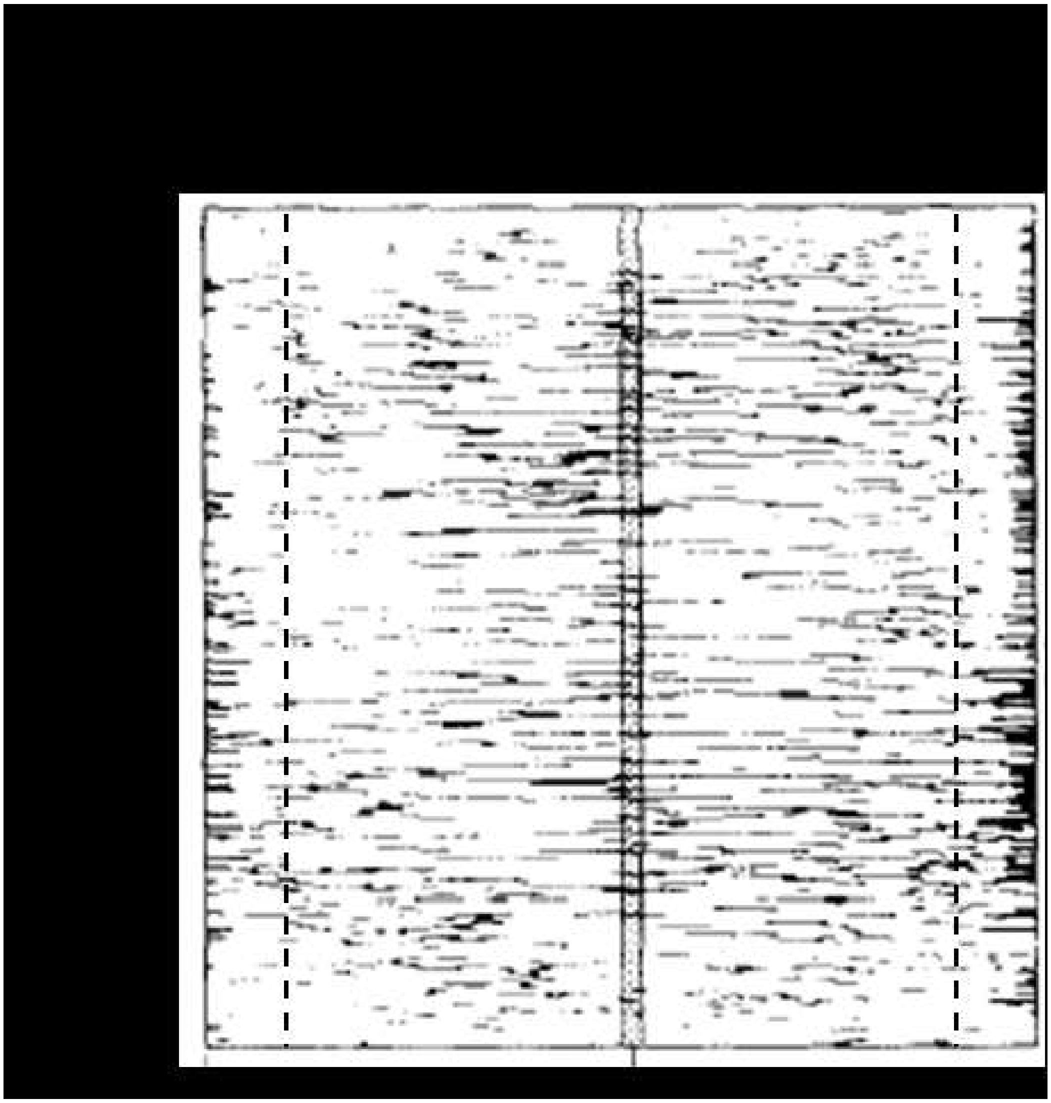

Fig. 6 – Top view of a brittle layer showing fracture deformation from four-point bending. Center box is 2mm wide x 100 cm long window on top of the brittle layer where fracture saturation was calculated. Edge effects diminish 10 mm from the edge of the brittle layer as shown by dashed lines. After Wu and Pollard (1995).

Four-Point Beam Bending of Rocks under Confining Pressure

Weinberger et al. (1994) deformed samples of Berea sandstone, Indiana limestone, and Tennessee sandstone under confining pressures of 5 MPa to 50 MPa using four-point beam bending tests. The four-point bending loading is designed to generate near uniform stress across the central portion of the beam. The tested beams had square cross-sections with dimensions of 1.8 cm x 1.8 cm and were 7.5 cm long. Stress-strain curves calculated during the experiment were generally linear in compressional arcs and non-linear in tensile arcs. The tensile stress-strain curve exhibited irregularities after measurements of $0.0001 < e < 0.0003$ that were interpreted as local fractures that initiated due to high tensile stresses at the surface (Weinberger et al., 1994). Fractures grew and developed until they terminated at the neutral surface of the beam.

NUMERICAL SIMULATION OF FOUR-POINT BEAM TEST

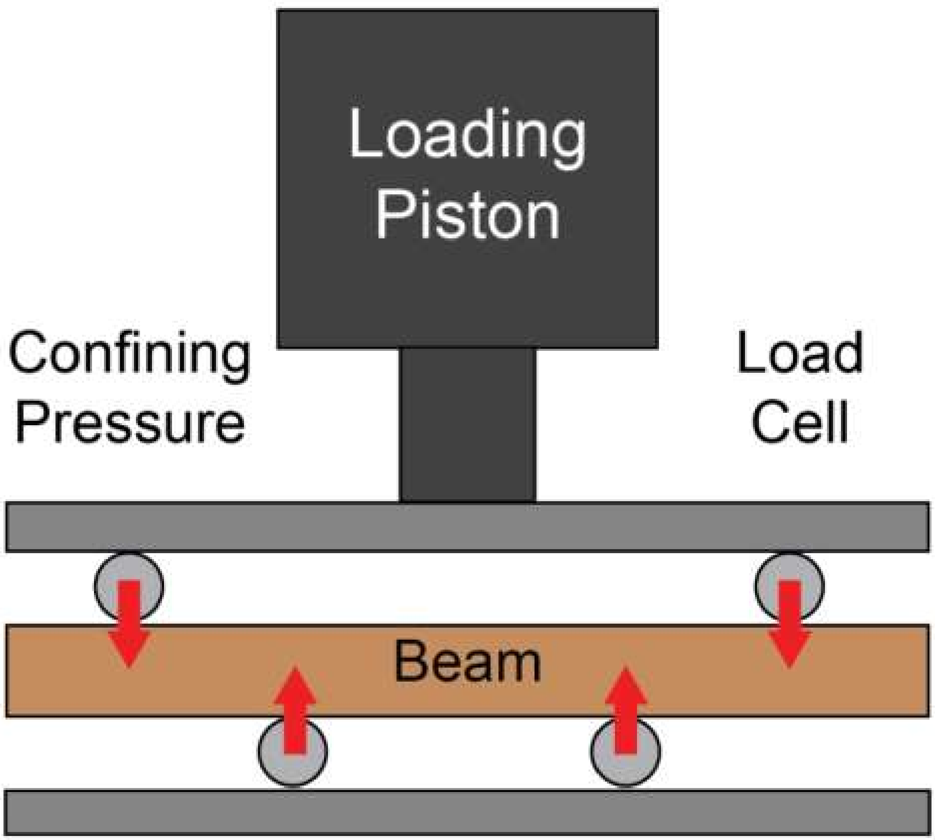

Fig. 7 – Schematic of four-point beam model with red arrows indicating direction of deformation from points. After Busetti (2009).

Busetti (2009) presented numerical simulations of the four-point beam bending setup (Fig. 7) of Weinberger et al. (1994) experiments. He used the rock properties of the Berea sandstone as defined by Weinberger et al. (1994) for an elastic-plastic-damage rheology. Busetti performed 3D finite element numerical simulations of four-point beam bending analysis using dimensions and conditions of laboratory tests, using the mirror of symmetry (Fig. 8).

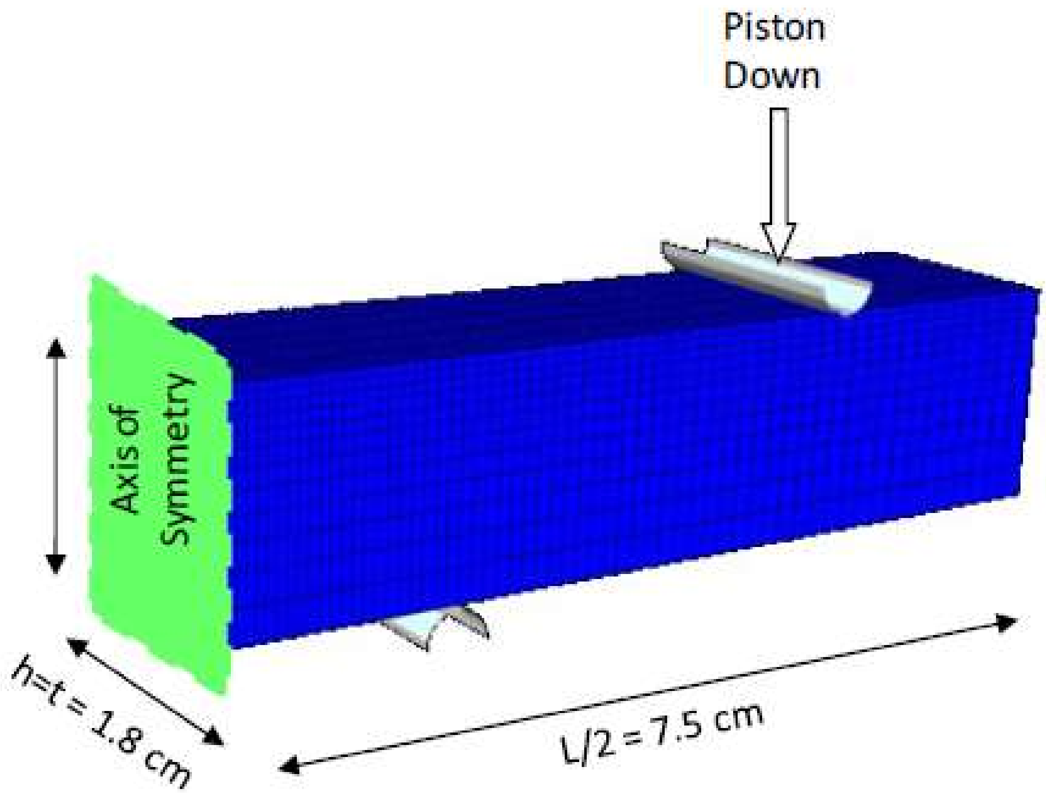

Fig. 8 – Design of beam used in numerical modeling. Only the right half of the beam is shown due to the symmetry of the experiment. After Busetti (2009).

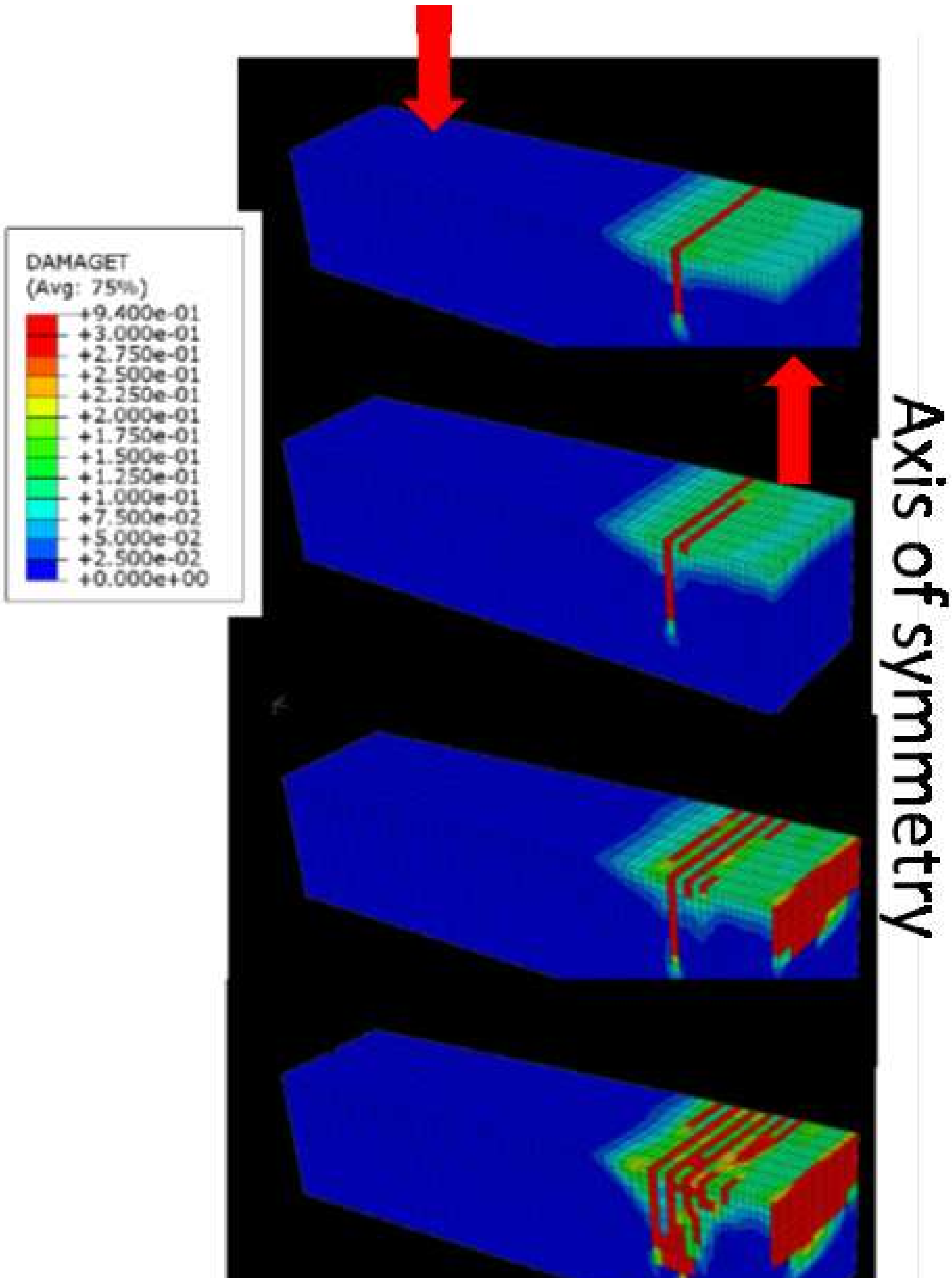

Fig. 9 – Damage intensity in numerical simulations of four-point beam testing on Berea sandstone. Stages of deformation starting at the top and continuing to the bottom. Red arrows indicate points of deformation. Blue colors represent undeformed material, while warm colors represent increasing damage with red indicating areas of potential fracturing. The center of the beam is on the right. After Busetti (2009).

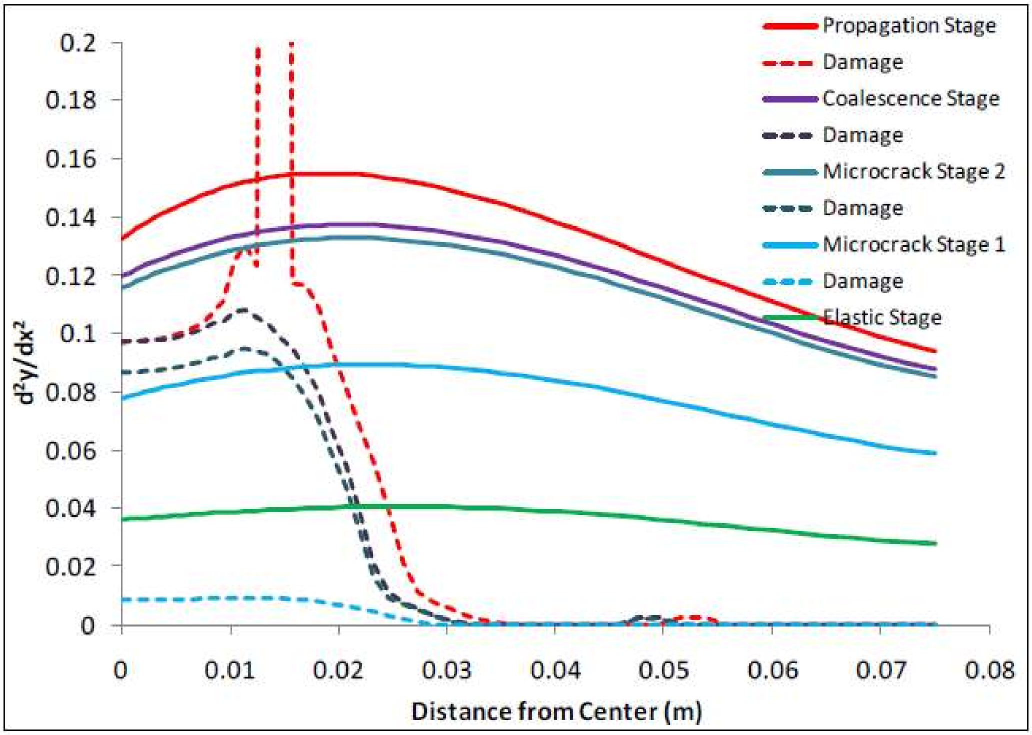

Fig. 10 – Curvature (solid lines) and damage (dashed lines) for five stages in numerical beam bending experiment that were generated due to incremental strain. After Busetti (2009).

Busetti (2009) reported that during the four-point-bending experiment, damage increased to a value of 0.1 prior to the first fracture indicating a 10% stiffness reduction. He defined stiffness reduction as direct scaling of stiffness by the effective load bearing area. Multiple fractures formed in regions of 15-20% stiffness reduction as shown in Fig. 9 where blue colors show little or no damage and warm colors show increasing damage. Red is the highest amount of damage and indicates fractures in the beam. Busetti (2009) noted that major damage and fracturing did not occur in the center of the beam, as would be expected from a uniform bending experiment, rather at a distance of approximately 0.015 m away from the center. He attributed this anomaly to the location of the fixed points at the base of the beam. He calculated and plotted the curvature for his five different stages of the deformation: Elastic, Microcrack 1, Microcrack 2, Coalescence, and Propagation, with corresponding damage in the same graph (Fig. 10). Damage developed in areas of maximum curvature. I correlated the damage (% stiffness reduction) and curvature calculated by Busetti (2009) and found that they are linearly related (Fig. 11).

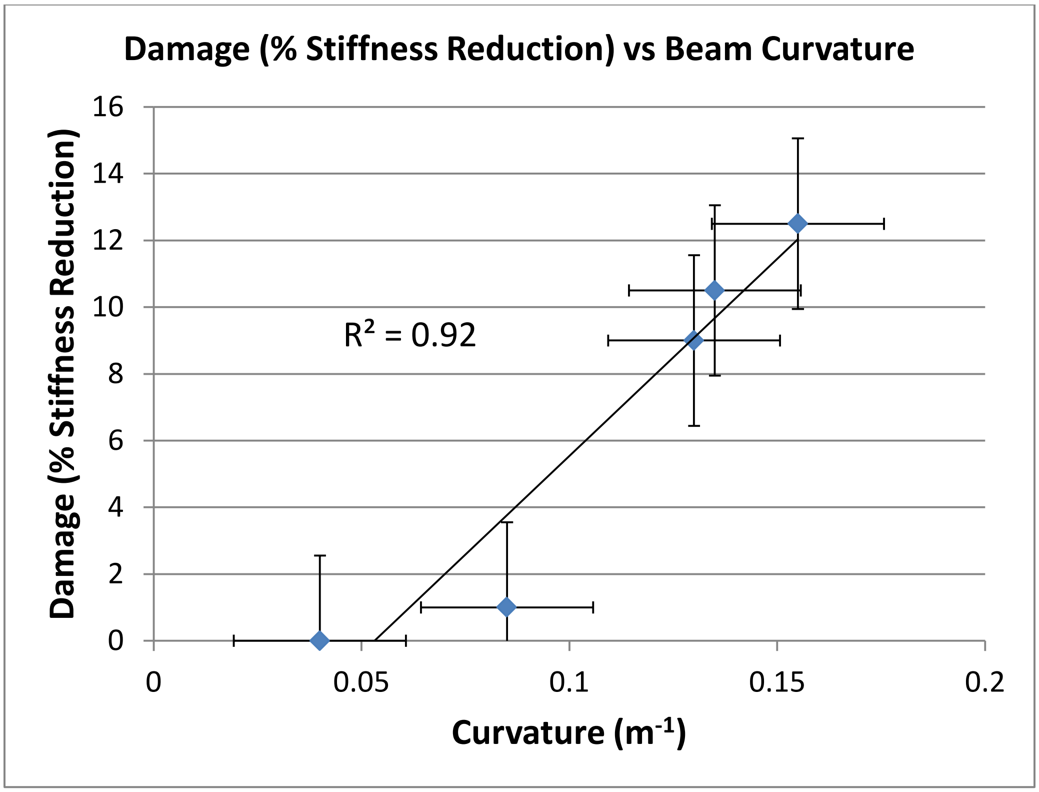

Fig. 11 – Relationship between curvature and damage intensities, validating predictions by Manaker et al. (2007) given by eq. 1 - 5. After Fig. 10 (Busetti, 2009).

Curvature Application in previous studies

Multiple studies link fractures to structural curvature using outcrop measurements, 3D-seismic data, and well logs. Murray (1968) was one of the first to correlate fractures in the subsurface to curvature using core and well log data. Nissen et al. (2009) calibrated 3D-seismic data to fractures using a horizontal well near the 3D survey. Potential fracture zones seen by lineaments in the subsurface were identified using the curvature attribute in 3D seismic surveys by Chopra and Marfurt (2007, 2008, 2010), Narhari et al. (2009), and Hart (2006). Fractures in the outcrop were correlated to curvature by Bergbauer (2007), Bergbauer and Pollard (2003), Hennings et al. (2000), Fischer and Wilkerson (2000), and Lisle (1994). In addition to listing the previous studies, I also report two studies that use 3D-seismic curvature to identify fracture zones in the subsurface and correlate curvature with horizontal-borehole-image logs, similar to the technique I used in this study

HORIZONTAL-BOREHOLE-IMAGE LOG CORRELATION WITH CURVATURE

Hunt et al. (2010) used 3D-seismic data and two horizontal-borehole-image logs to correlate fracture densities to curvature. Image log data are recorded with resolution of approximately 0.2 in (see Appendix B for description of image logs) while seismic data are recorded in data bins from 55 to 110 ft. Hunt et al. (2010) interpreted the image logs and created image-log-data bins every 32 ft along the horizontal wellbore paths in an attempt to scale the image log data closer to seismic data. They stated that the curvature attribute and amplitude variation with azimuth (AVAz) correlated multilinearly to fracture density with a correlation coefficient of 0.74.

Ericsson et al. (1998) used 3D-seismic data and ~10 miles of horizontal-borehole-image log data to identify fracture mechanisms in the reservoir rock. They found that grain-supported-rock textures in the reservoir were more brittle than matrix-supported-rock textures. In addition to rock textures, areas of flexure and faulting had high fracture densities. Fig. 12 shows the empirical distribution of fractures in the study as calculated by Ericsson et al. (1998). Areas of high curvature account for 68% of all fractures in the study with most of those fractures occurring in areas of grainstone facies.

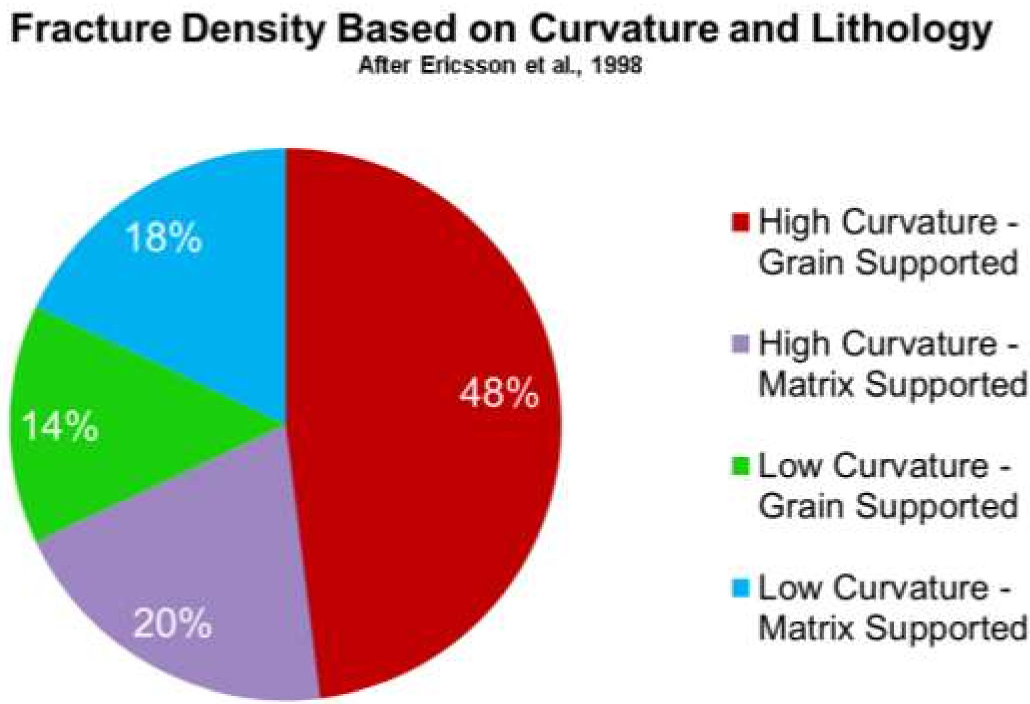

Fig. 12 – Empirical percentages calculated from over 12,000 fractures in ~10 miles of horizontal-borehole-image log data. After Ericsson et al. (1998).

PRESENT STUDY

The main purpose of this study is to identify fracture zones using 3D-seismic data. Clay models, horizontal-borehole-image logs, and 3D-seismic data provide a database to view curvature and fracturing at multiple scales and stages of deformation. The clay models were critical because they captured folding and fracturing as it developed from undeformed to the final stage of high curvature and fracture intensity. They were models that showed the ideal situation for fracture generation due to folding. Horizontal-borehole-image logs provided fracture data and apparent curvature, providing "ground" truth for 3D-seismic data. Cross-correlations between areas of high curvature in 3D-seismic data and high fracture density from the image logs helped illuminate fracture patterns in the subsurface and allow for prediction of other zones of high fracture density. Using this rationale, I linked clay experiments to actual field data to quantitatively identify curvature values that generate fracture zones.

CLAY MODEL EXPERIMENTS

Clay models are important because they show folding and fracturing in "real-time," providing analogs for subsurface structures. Reches (1988) indicated that clay models exhibit fault patterns similar to those in the field and previous clay experiments have illuminated our understanding of faulting mechanics and fault-related deformation. He also stated it is difficult to observe continuous growth of stable faults in unconfined rock samples because they tend to yield unstably. Lastly, he suggested that despite rheology differences between clay and rocks, the strain fields accompanying faulting in clay are similar to those predicted by displacement calculations in other studies (e.g., Hildebrand-Mittelfeldt, 1979) (See Appendix A). Following the rationale of Reches (1988) for clay models, I tested curvature predictions in clay models while monitoring continuous fracture and curvature development.

The experimental apparatus consisted of a horizontal table with one moveable side-wall, one stationary side-wall and a deforming base. I ran four experiments, one extensional and three compressional. In the extensional experiment, the clay cake was placed on top of two rigid, thin metal plates that were moved away from each other (Fig. 13, left). In the compressional experiments, the clay cake was placed on two metal wedges with inclinations 45°, 30°, and 15° that moved toward each other to generate reverse basement faulting (Fig. 13, right). Rate of displacement was 0.08 cm/min in all experiments and was measured rather than strain in the clay models.

In the clay experiments, I began by constructing homogenous clay cakes of 1.22 g/cm^3 density measuring 20 cm long, 15 cm wide, and 5 cm thick. A laser scanner positioned above the clay cakes captured 3D-surface images at vertical and horizontal resolutions of 75 DPI (~0.0381 cm point density) every two minutes. A typical experiment lasted approximately 30 min providing 15 stages of deformation. The short duration of the experiments eliminated clay drying as a variable.

The curvature of the clay surface was calculated from the laser scans using commercial software, and the fractures were mapped on digital photographs of the clay surface. Curvature over the deformation area was calculated in each stage by placing three polygons at fixed locations and averaging the curvature within each polygon. The fracture intensity (FI) was calculated for these polygons by dividing total measured fracture length in each polygon by the polygon area.

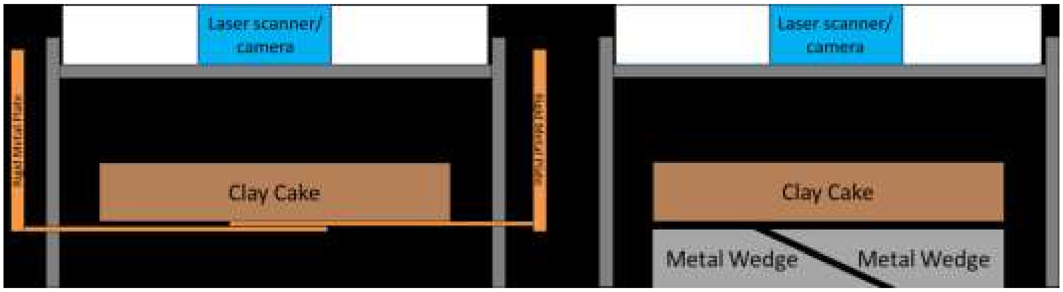

Fig. 13 – Setup for the clay experiements, extensional (left) and compressional (right). Metal wedge angles used included 45°, 30°, and 15°.

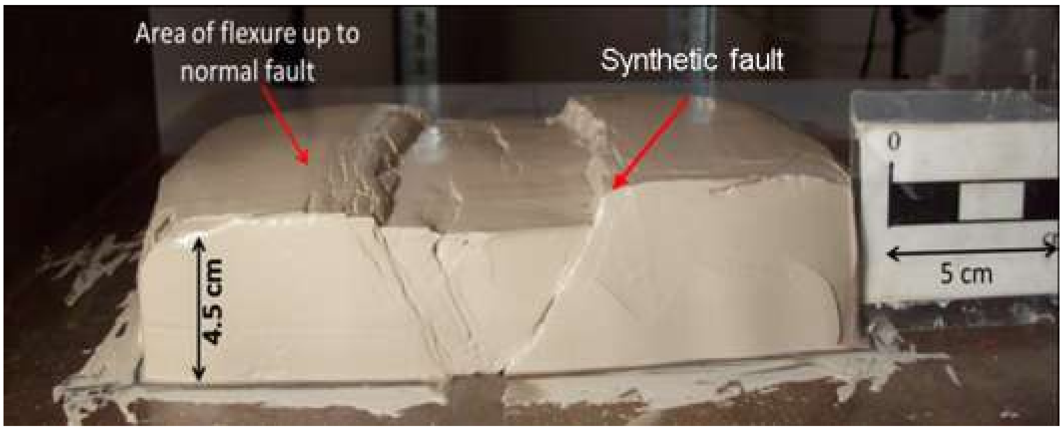

Fig. 14 – General view of extesional experiment. Note flexure on graben left side where the curvature was correlated to fracture density.

Results

In the extensional experiment, a basin formed in the center of the clay cake with a synthetic-listric-normal fault on the right side. Antithetic-normal faulting, fracturing, and flexure occurred on the left side of the basin giving rise to structural curvature anomalies (Fig. 14). Fig. 15 shows a suite of positive curvature images from undeformed to the final stage. Fractures were first visible at a clay surface curvature of $2.53x10^{-3}$ cm^{-1} and FI measurements conducted on the left side of the basin, total extension, and curvature values are shown for each stage of deformation in Table 1. Fractures measured in the extensional experiment were tensile fractures.

Table 1 – Observations during extensional experiment

Stage of Deformation	Ave Extension (cm)	Ave Curvature (cm^{-1})	Ave FI (total measured fracture length/area)
1	0.16	0.0025	---
2	0.32	0.0025	---
3	0.48	0.0025	0.03
4	0.64	0.0038	0.62
5	0.80	0.0038	1.32
6	0.96	0.0075	1.51

Table 2 – Observations during compressional experiment, 45° ramp

Stage of Deformation	Ave Compression (cm)	Ave Curvature (cm^{-1})	Ave FI (total measured fracture length/area)
1	0.16	0.0014	---
2	0.32	0.0026	---
3	0.48	0.0026	---
4	0.64	0.0026	---
5	0.8	0.0027	---
6	0.96	0.0027	---
7	1.12	0.0027	---
8	1.28	0.0028	---
9	1.44	0.0204	---
10	1.6	0.0203	---
11	1.76	0.0213	0.19
12	1.92	0.0224	1.05
13	2.08	0.0228	1.17

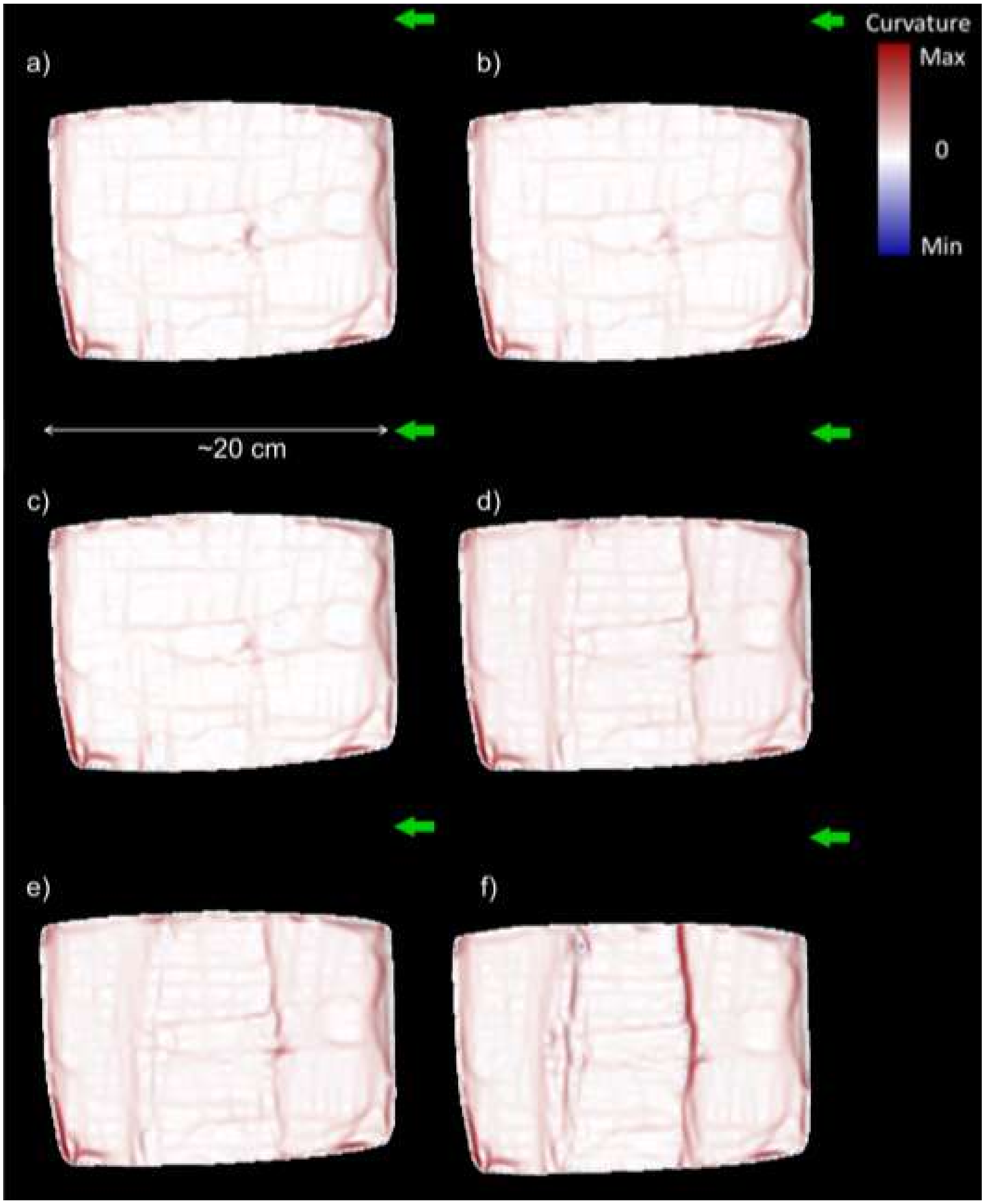

Fig. 15 – Most-positive curvature computed from the undeformed to final stage (a, b, c, d, e, and f) of extension experiment (Fig. 14). Subtle curvature anomalies parallel and perpendicular to the fault correlate to tool marks made in the initial clay model construction. Fracture intensity calculations occurred on the left side of the central graben.

In all three compressional experiments, an anticline developed with fractures on the crest sub-parallel to the axial plane (Fig. 16). Fractures were first visible at a clay surface curvature of 1.40×10^{-2} cm^{-1} to 2.13×10^{-2} cm^{-1}. Fractures measured in all compressional experiments were tensile fractures. Tables 2, 3, and 4 shows FI measurements conducted on the top of the anticlines, total compression, and curvature values for each stage of deformation for fault ramps of 45°, 30°, and 15°, respectively. Fig. 17 shows a suite of positive curvature images for all even numbered stages of deformation from undeformed to the final stage of deformation for the 30° ramp. Positive curvature images from the 15° and 45° ramp are located in Appendix A. Curvature values increased with the fault ramp steepness, 15°, 30°, and 45°, as show in Fig. 18.

Table 3 – Observations during compressional experiment, 30° ramp

Stage of Deformation	Ave Compression (cm)	Ave Curvature (cm^{-1})	Ave FI (total measured fracture length/area)
1	0.16	0.0010	---
2	0.32	0.0011	---
3	0.48	0.0015	---
4	0.64	0.0022	---
5	0.8	0.0029	---
6	0.96	0.0035	---
7	1.12	0.0055	---
8	1.28	0.0075	---
9	1.44	0.0075	---
10	1.6	0.0102	---
11	1.76	0.0123	---
12	1.92	0.0144	---
13	2.08	0.0162	0.18
14	2.24	0.0174	0.36
15	2.4	0.0181	0.87
16	2.56	0.0193	1.49
17	2.72	0.0198	1.67
18	2.88	0.0203	1.78
19	3.04	0.0207	1.96

Table 4 – Observations during compressional experiment, 15° ramp

Stage of Deformation	Ave Compression (cm)	Ave Curvature (cm^{-1})	Ave FI (total measured fracture length/area)
1	0.16	0.0014	---
2	0.32	0.0016	---
3	0.48	0.0018	---
4	0.64	0.0019	---
5	0.8	0.0021	---
6	0.96	0.0025	---
7	1.12	0.0037	---
8	1.28	0.0044	---
9	1.44	0.0055	---
10	1.6	0.0064	---
11	1.76	0.0074	---
12	1.92	0.0082	---
13	2.08	0.0091	---
14	2.24	0.0098	---
15	2.4	0.0108	---
16	2.56	0.0108	---
17	2.72	0.0123	---
18	2.88	0.0130	---
19	3.04	0.0140	0.07
20	3.2	0.0148	0.16
21	3.36	0.0155	0.27
22	3.52	0.0161	0.52
23	3.68	0.0163	0.57
24	3.84	0.0169	0.61
25	4	0.0174	0.73
26	4.16	0.0178	1.14

Fig. 16 – Photograph from above demonstrating fractures on the top of the deformed anticline in the 30° compressional experiment.

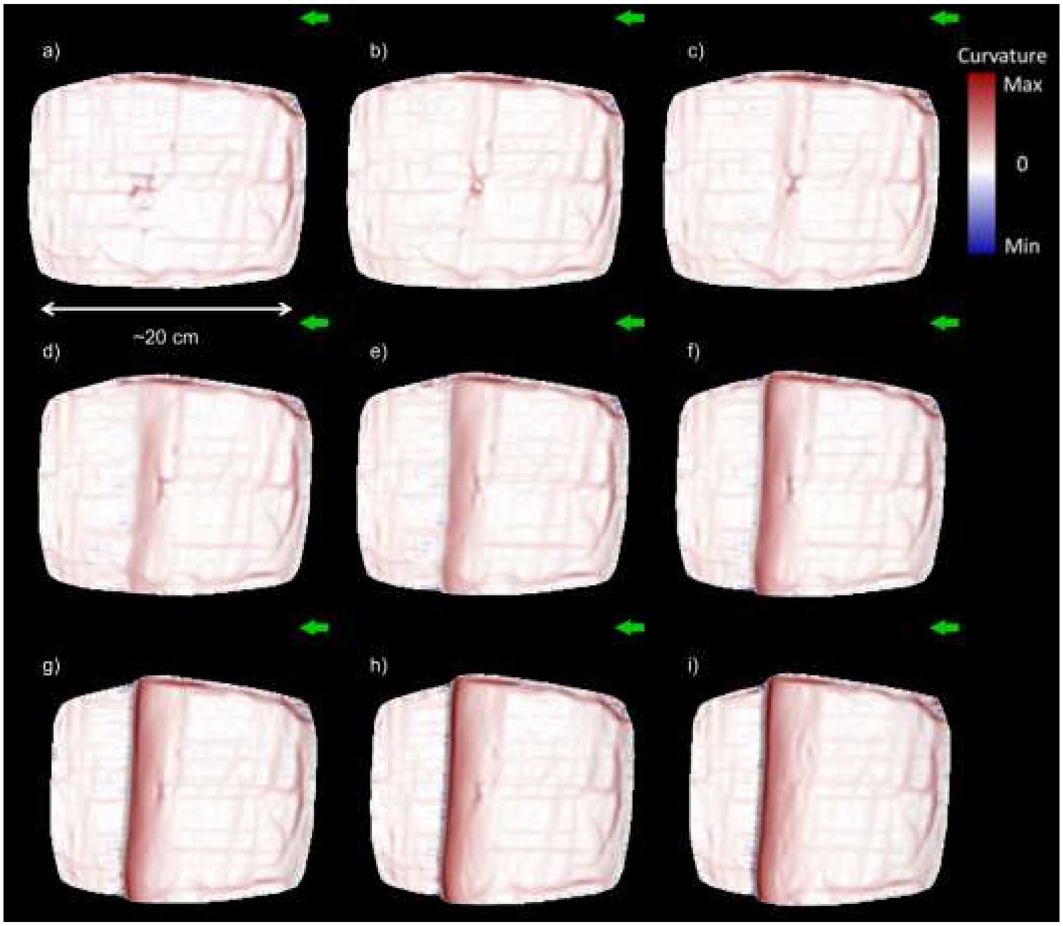

Fig. 17 – Most-positive curvature computed from undeformed to final (a, b, c, d, e, f, g, h, and i) of compressional 30° ramp experiment (Fig. 16). Subtle curvature anomalies parallel and perpendicular to the fault correlate to tool marks made in the initial clay model construction. Fracture intensity calculations occurred on the top of the anticline.

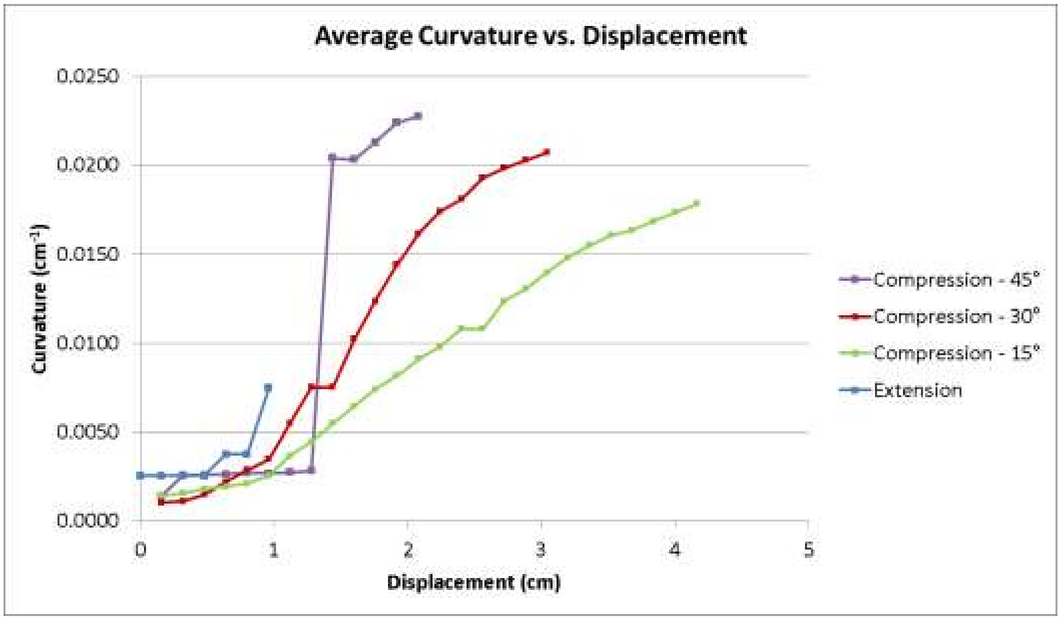

Fig. 18 – Curvature values increase as displacement increases.

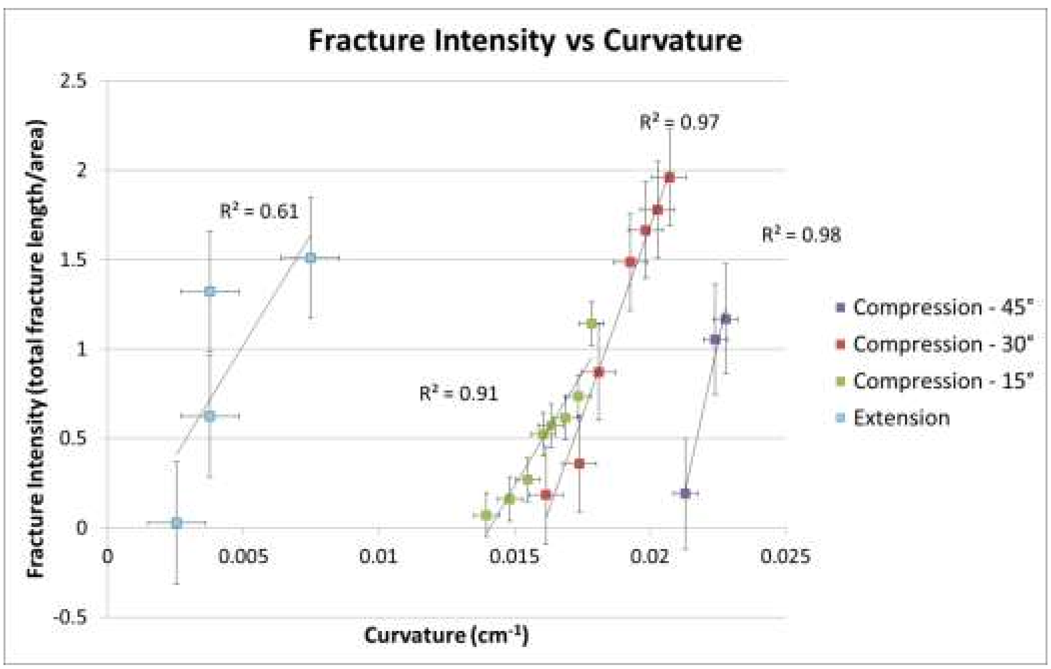

Fig. 19 – Linear relationship observed between fracture intensity and curvature with standard error bars for all four experiments.

Synthesis

<u>Curvature:</u> Curvature increased over time with systematic deformation occurring in the extensional, 15° compressional ramp, and 30° compressional

ramp experiments (Fig. 18). Deformation in the 45° compressional ramp was non-systematic, but followed a similar trend as that seen in the other two ramp experiments. Maximum curvature values varied based on the experimental setting with the extensional value ($7.5x10^{-3}$ cm^{-1}) being one order of magnitude lower than the compressional settings ($2.28x10^{-2}$ cm^{-2} to $1.78x10^{-2}$ cm^{-1}).

FI: Calculated FI increased with curvature and correlations show a strong linear relationship, however fracturing did not occur at the same curvature value in each experiment (Fig. 19). The extensional experiment showed fracturing initiation at a significantly lower curvature value ($2.53x10^{-3}$ cm^{-1}) than compressional experiments (Fig. 19) where fracturing initiated at values one order of magnitude higher than extensional experiments. ($2.13x10^{-2}$ cm^{-1}, $1.62x10^{-2}$ cm^{-1}, and $1.40x10^{-2}$ cm^{-1} for 45°, 30°, and 15° ramps, respectively). Differences in horizontal strain cause this disparity in fracturing. In the extensional experiment, horizontal strain occurred throughout the experiment since the basement plates were constantly moving apart, though I only measured displacement. However, in the compressional settings, an anticline had to develop and grow before horizontal strain was great enough on its crest to induce fracturing.

CORRELATION OF CURVATURE TO FRACTURES IN THE HUNTON GROUP, CENTRAL OKLAHOMA

The focus of this study is to use 3D-seismic data to identify fracture zones in the subsurface. This required the following steps: (1) Identifying fractures from horizontal-borehole-image logs. (2) Calculating curvature from bedding-planes identified in the horizontal-borehole-image logs to crosscheck 3D-seismic curvature calculations. (3) Correlating fracture density from the horizontal-borehole-image logs with the 3D-seismic curvature calculations. (4) Identifying geometries in the subsurface that correlate with high fracture densities from horizontal-borehole-image logs to provide a basis used to identify potential areas of high fracture density using only 3D-seismic data.

The subsurface database used in this study includes approximately nine mi^2 of proprietary pre-stack-time-migrated (PSTM) 3D-seismic data in the Central Oklahoma Platform, seven horizontal wells with image logs within the 3D-seismic survey (cumulative length of three miles) targeting the Hunton Group, and sonic logs of 14 vertical wells that also penetrate the Hunton Group. Pathfinder Exploration, LLC, kindly provided these data.

GEOLOGIC SETTING

Hunton Group

The Hunton Group (Late Ordovician to Early Devonian) is an important hydrocarbon reservoir throughout Oklahoma (Fig. 20). In the subsurface, it has been identified in multiple basins – Anadarko, Ardmore, Marietta, and Arkoma – and the southwestern part of the Cherokee Platform (Northcutt, 2000). Most of the subsurface reservoir rocks in the Hunton Group are dolomitized and many of the Hunton Group hydrocarbon fields correspond to a regional dolomite trend (Al-Shaieb et al., 2001). In addition, there are places where the Hunton Group is present in the Wichita and Arbuckle Uplifts (Northcutt, 2000).

The Hunton Group consists of three general parts: lower, middle, and upper. The lower part includes the Chimneyhill Subgroup and Keel Oolite, which represent skeletal limestones and shoaling, respectively (Northcutt et al., 2001). The middle part consists of the Haragan, Bois d'Arc and Henryhouse Formations, which represent a depositional sequence deposited on a gently inclined ramp and with a general composition including shale, argillaceous-limestone, and fossiliferous limestone. Shales mark parasequence boundaries with each parasequence shale-rich at the base and limestone-rich near the top (Al-Shaieb and Puckette, 2000). The upper part of the Hunton Group consists of the Frisco Formation (Northcutt et al., 2001). Stanley (2001) identified two lithofacies in the Frisco Formation, which included a mud-supported floatstone to wackestone deposited in bryozoan-crinoid thickets and a grain-supported intermound and capping-bed facies deposited from currents reworking the sediments.

Al-Shaieb et al. (2001) identified fractured reservoirs in the Hunton, which consisted of low-permeability, massive limestone with fluid flow along bedding planes and fractures causing dissolution. The dissolution creates wide joints and caves allowing for common collapse features due to weakening of the massive limestone. Al-Shaieb et al. (2001) also identified reservoirs in grain-rich dolowackestones that are more porous and allow for interparticle fluid flow with little dissolution. In addition to fractures, structural and stratigraphic traps exist in the Hunton Group, which make it a very productive hydrocarbon reservoir. Rottman (2000) suggests five scenarios where hydrocarbon traps form along the Woodford-Hunton contact. They include post-Hunton – pre-Woodford erosion, post-Hunton – pre-Woodford eroded horst block, thickness changes in the Hunton due to penecontemporaneous faulting or folding, post-Hunton – pre-Woodford graben filled with detritus, and faults cutting the Hunton Group.

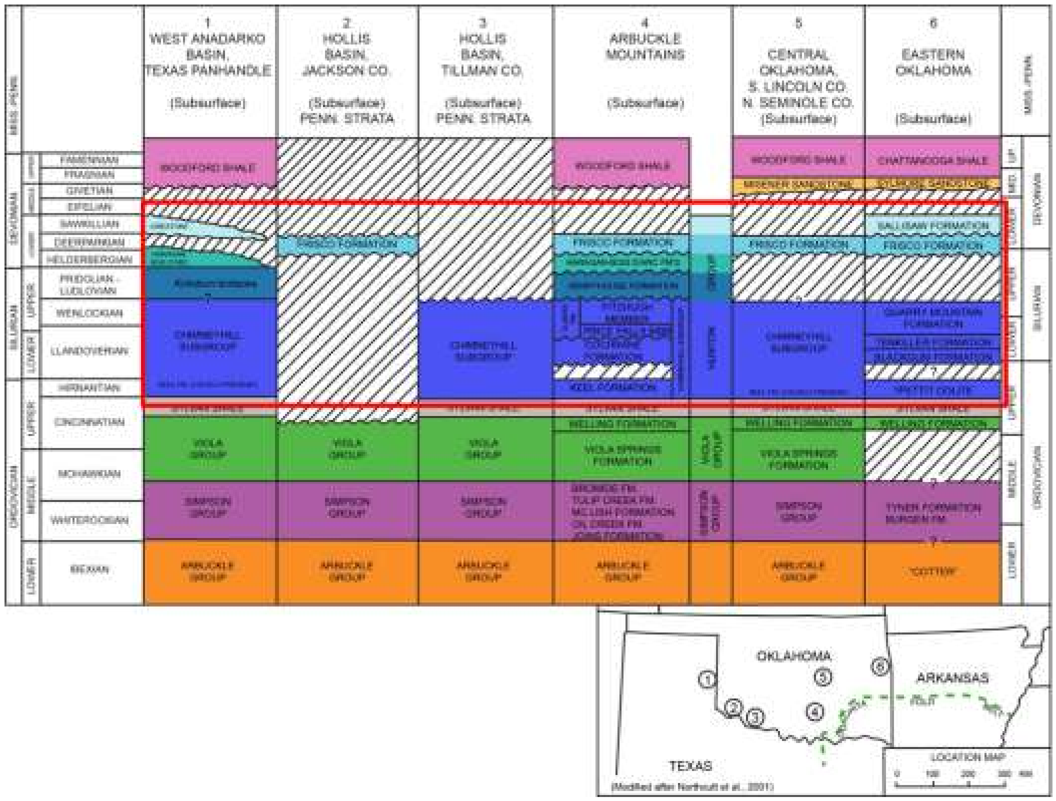

Fig. 20 – Regional stratigraphic column of Oklahoma showing Arbuckle Group through the Woodford Shale. Hunton Group members are shown in shades of blue and outlined by a red box. Diagonal lines represent areas of erosion or no deposition. After Northcutt et al. (2001).

SUBSURFACE ANALYSIS

Borehole Analysis

Methods

First, the horizontal-borehole images were loaded into commercial software and aligned to the azimuthal pad so fracture interpretations were oriented according to the cardinal directions (See Appendix B for complete image log description). Then, fractures were identified as sinusoids on the image log (Fig. 21) with assumed open and closed fractures colored dark and light, respectively. Bedding-planes were also identified in the horizontal-borehole-image logs. Because the boreholes were sub-horizontal, sinusoids indicating sub-parallel bedding-planes had much higher amplitude than fracture sinusoids identifying fractures (Fig. 21).

Next, fractures were ranked since not all fractures were imaged equally. The ranking system consisted of "A", "B", "C", and "D" fractures (Fig. 21) with "A" fractures being visible continuously across the entire image with no apparent breaks in the fracture. "B" fractures were identifiable across the image but had minor breaks visible in the fracture. "C" fractures were not continuous, and had portions missing partly due to imaging problems. "D" fractures consisted of multiple areas that looked like portions of the same fracture, but were difficult to combine as one fracture. Fracture auto-picking was an option, but not used due to unreliable results as clear "A" fractures were bypassed while areas with no definite fractures had multiple fracture picks. In order to avoid errors in fracture identification, each fracture was visually identified and manually picked.

After fracture interpretation, all fractures were counted along each wellbore. Following the methodology of fracture binning by Hunt et al. (2010) I placed the fractures in data bins 55 ft long which is one half of the 110 ft seismic bins in the 3D survey. I did this to scale the image log data to seismic resolution, but still maintain details from the image logs.

Lastly, curvature was calculated by plotting the bedding planes according to their horizontal position in the wellbore. A best-fit polynomial was calculated using least-squares regression and curvature was calculated along the resulting curve.

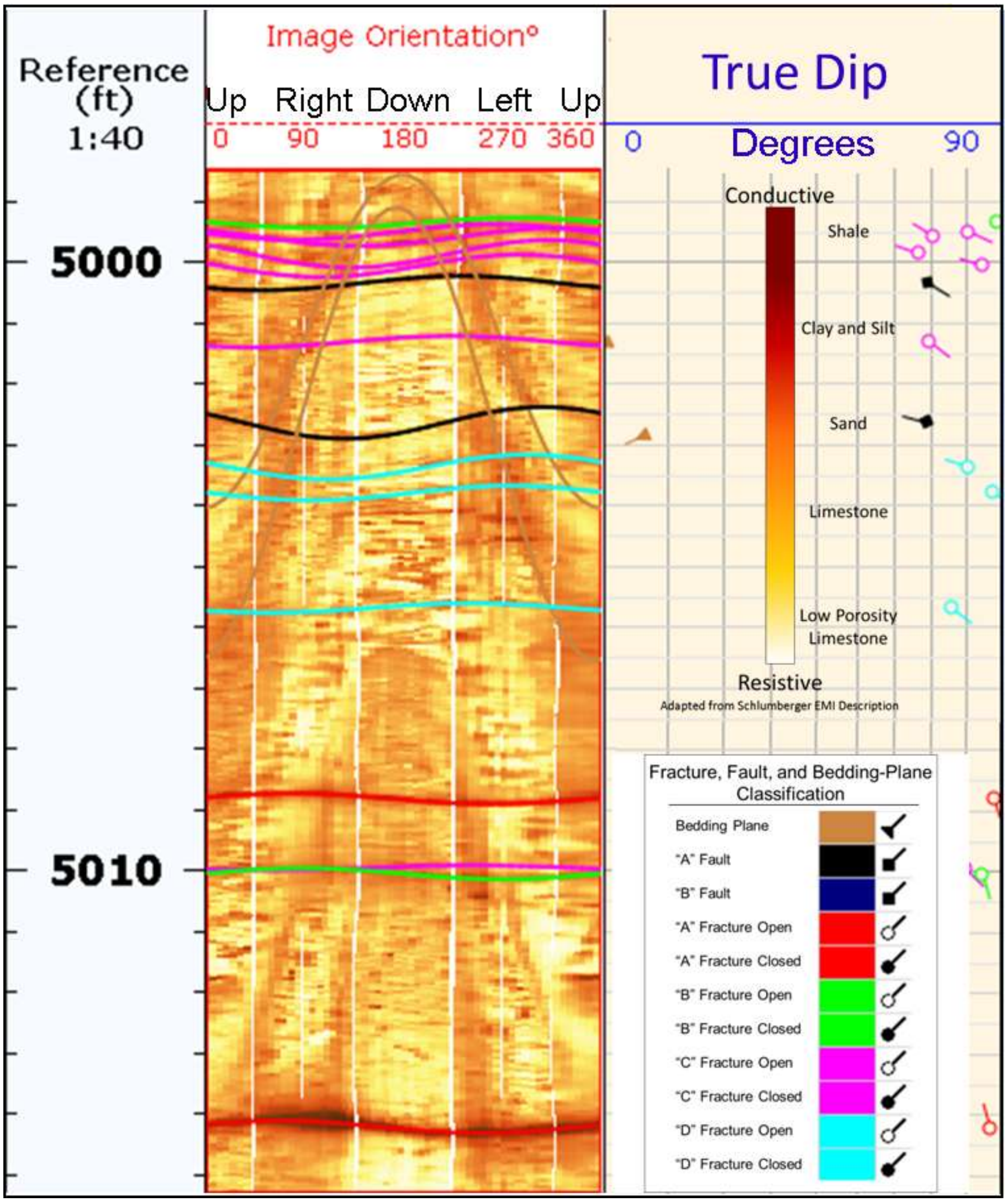

Fig. 21 – Image log showing fracture classifications for fracture type "A" to "D." Fractures were identified as sinusoids. Bedding-planes were sinusoids with higher amplitudes since the wells were drilled sub-parallel to bedding.

Fracture Analysis Results

I analyzed image logs from seven horizontal wells labeled Wells 1 to 7. Rose diagrams of the strike direction of all open fractures in each well are shown in Fig. 22. Fig. 23 shows the upper hemisphere of stereoplots for every well. Figs. 22 and 23 illustrate that Wells 1-4, and 6-7 have at least one fracture set striking in the same general southwest to northeast direction. Wells 2 and 6 have fracture sets that strike nearly perpendicular with the main fracture strike oriented in a southwest to northeast direction. Well 5 has a strike orientation nearly east to west, which is similar to the secondary fracture set in Well 4. “A”, “B”, and “C” ranked fractures are more tightly grouped than “D” fractures. Fracture density was calculated using the number of fractures per foot for each well and is shown per 55 ft bin in Fig. 24. Warm colors (red, orange, and yellow) indicate high fracture densities while cool colors (green and blue) show areas of low fracture density along the wellbore.

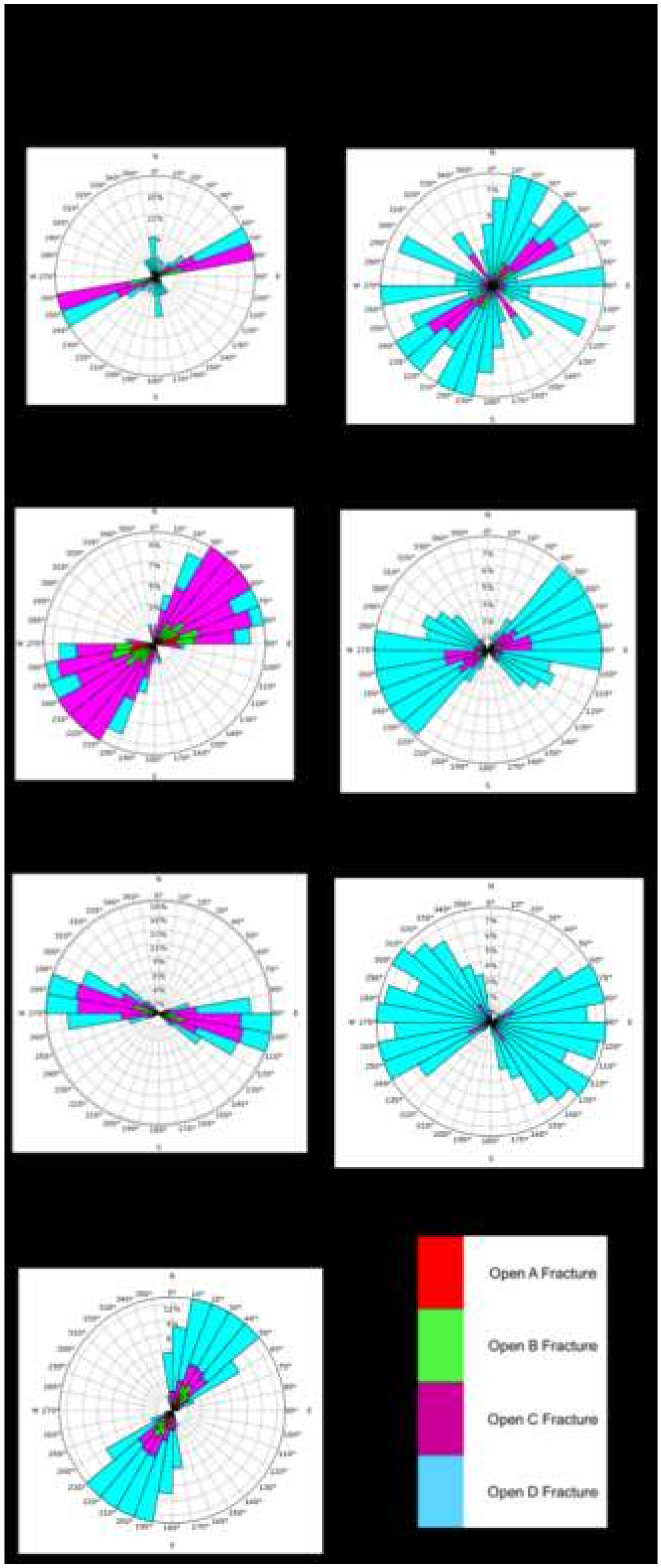

Fig. 22 – Rose diagrams for the fracture strike of each well in the project. Fractures are ranked A, B, C, and D and colored accordingly.

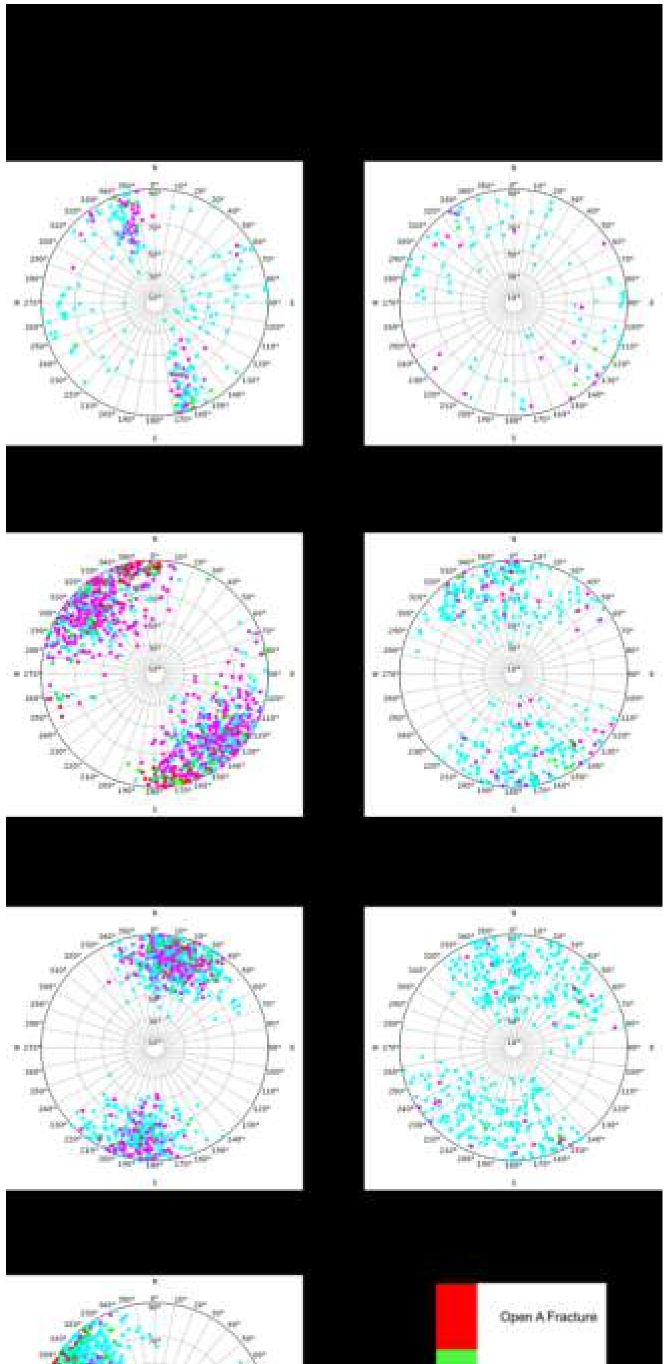

Fig. 23 – Stereoplots of each well, showing the fracture distribution from the upper hemisphere view. Fractures are ranked A, B, C, and D and colored accordingly.

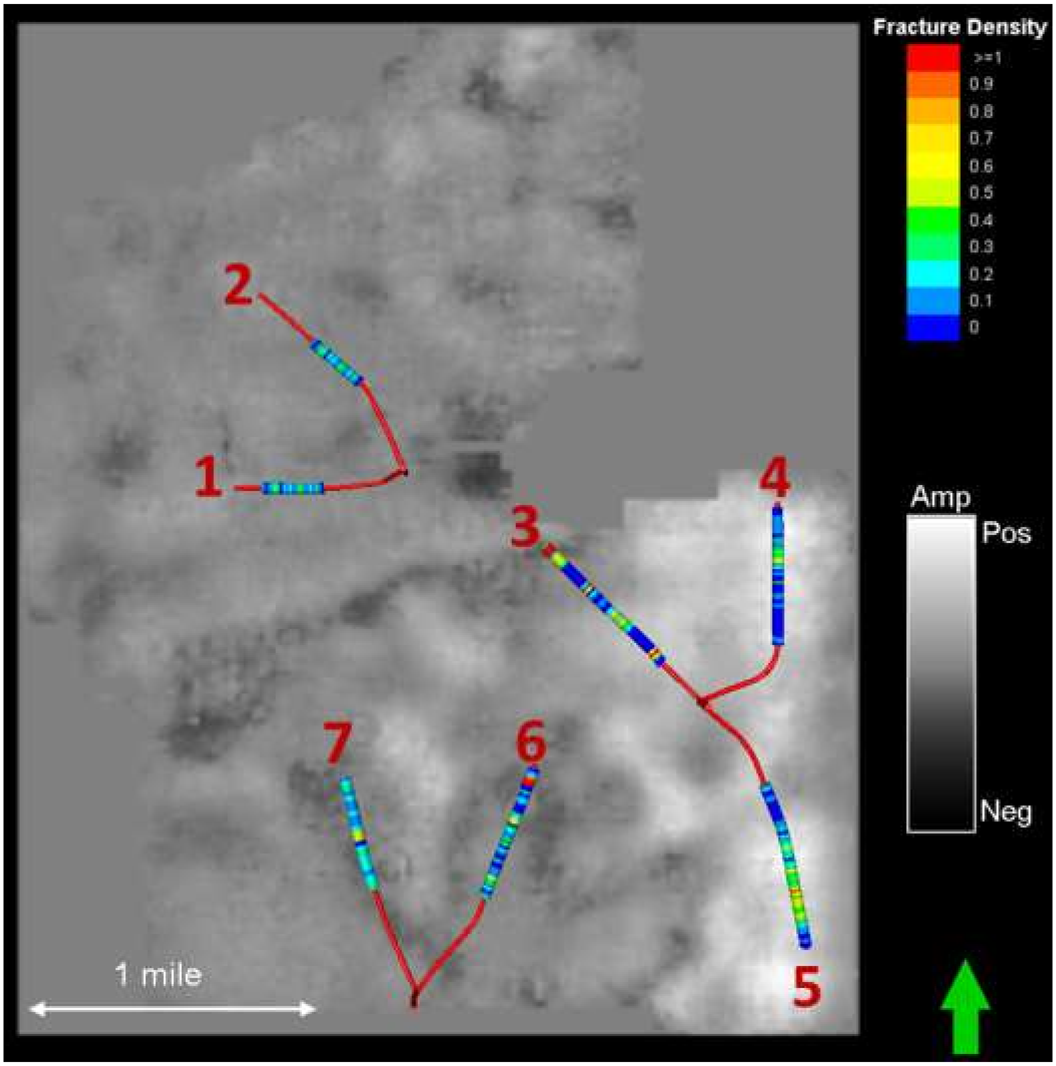

Fig. 24 – Fracture density as interpreted from the horizontal-borehole-image logs along the wellbores displayed on a time slice. Wells are numbered 1-7.

<u>*Curvature Analysis Results*</u>

Bedding-planes identified in Wells 3-7 enabled curvature to be calculated from the borehole similar to curvature calculations in the field (e.g., Hennings et al., 2000). Chopra and Marfurt (2007) describe curvature in two dimensions such that curvature is the radius of a circle tangent to a curve. Curvature in two dimensions, k, can be positive, negative, or zero. Anticlinal, synclinal, and linear structural geometries are illustrated by $k>0$, $k<0$, and $k=0$ respectively. Chopra and Marfurt (2007) define curvature in three dimensions, by fitting two circles tangent to a surface in orthogonal planes. The first circle is oriented to obtain the minimum radius (tightest curvature) while the second circle, in a plane orthogonal to the previous circle, will for a quadratic surface have the maximum radius. These two circles permit the calculation of the two principle curvatures, k_1 (most positive) and k_2 (most negative), of a quadratic surface. The eq. used to calculate two-dimensional (Chopra and Marfurt, 2010) curvature is:

$$k_{2D} = \frac{1}{R_c} = \frac{\frac{d^2z}{dx^2}}{[1+(\frac{dz}{dx})^2]^{3/2}} \tag{6}$$

where R_c is radius of curvature, d^2z/dx^2 is the second derivative of the curve, and dz/dx is the first derivative of the curve. Fig. 25 shows a field example of curvature.

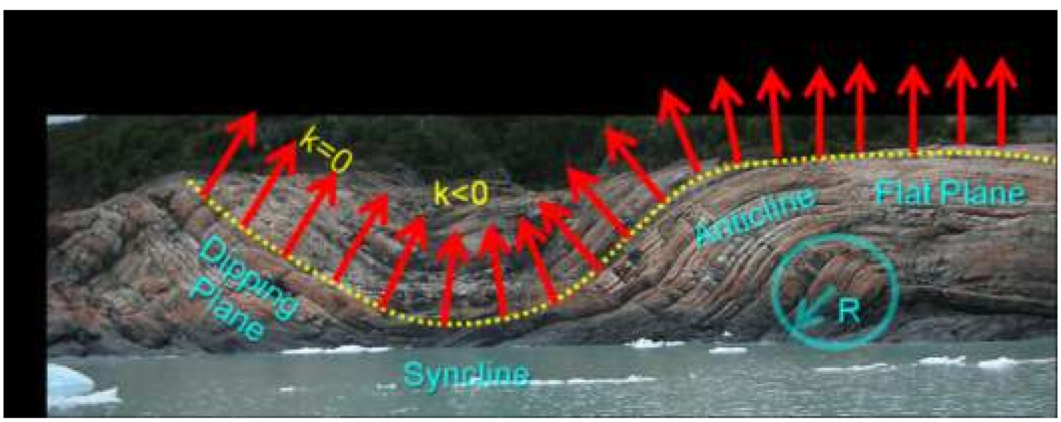

Fig. 25 – Annotated outcrop illustrating where curvature is positive (k>0), negative (k<0), or flat (k=0). The blue-green circle at the bottom right of the image indicates how the best-fit circle in the curved area is drawn and curvature (k) is equal to one over the radius (R). After Chopra and Marfurt (2010).

In order to compare curvature from the borehole to seismic data, Euler curvature (or apparent curvature in a given direction) was calculated $k_e^{(\Psi)} = k_1$

$\cos^2(\Psi - \Psi_2) + k_2 \sin^2(\Psi - \Psi_2)$, where k_1 and k_2 are the most positive and most negative principal curvatures, Ψ_2 is the strike of the most negative curvature, and Ψ is the azimuth from north of the horizontal well to be analyzed. Fig. 26 illustrates how Euler curvature differs from k_1 curvature. An anticline is shown in the subsurface with positive curvature having highest values west to east. A horizontal well shown in blue, is drilled at an angle Ψ from north along the vertical plane oriented in a northwest direction. Curvature values computed from the orientation of the horizontal well will be less intense than those in the direction of principal k_1 curvature. Bedding-plane curvature was compared to Euler curvature and found to have similar trends in Wells 3-7 (Figs. 27-31).

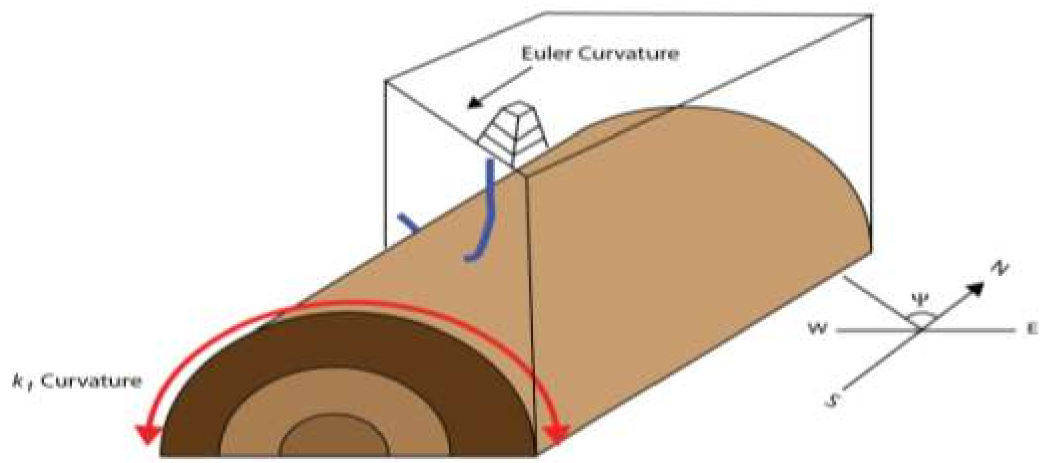

Fig. 26 – Comparison between Euler and k_1 curvature. The blue line is a horizontal well drilled at an angle ψ from north. Red line is direction of k_1 curvature.

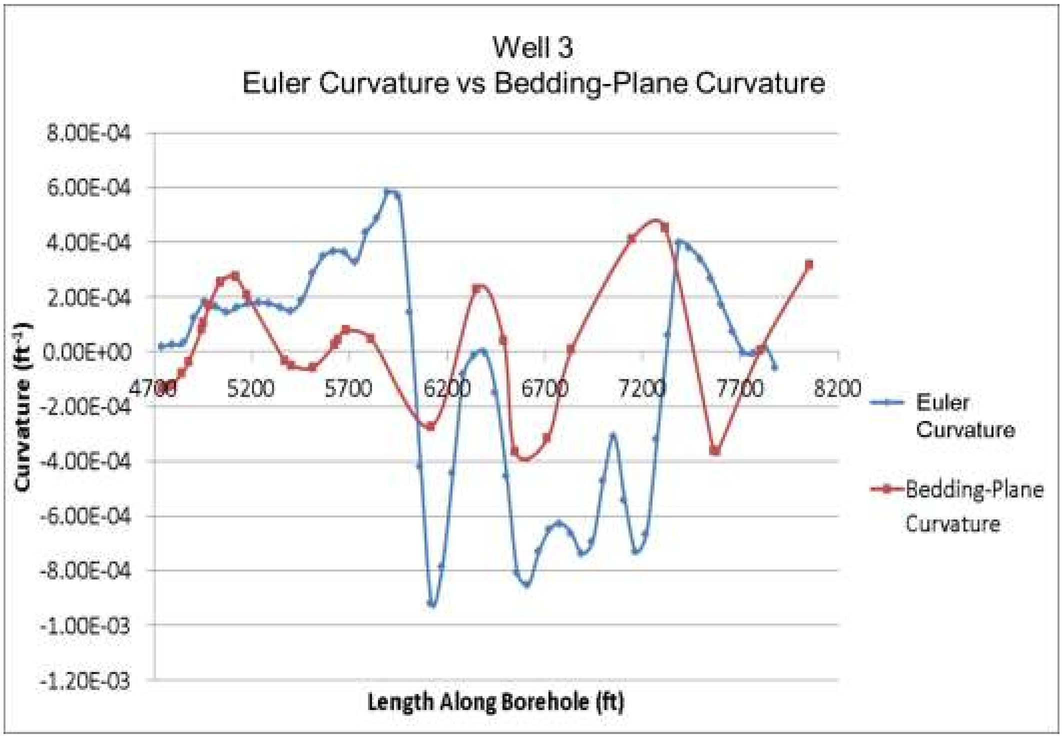

Fig. 27 – Bedding-Plane Curvature from Well 3 has similar trends as Euler Curvature.

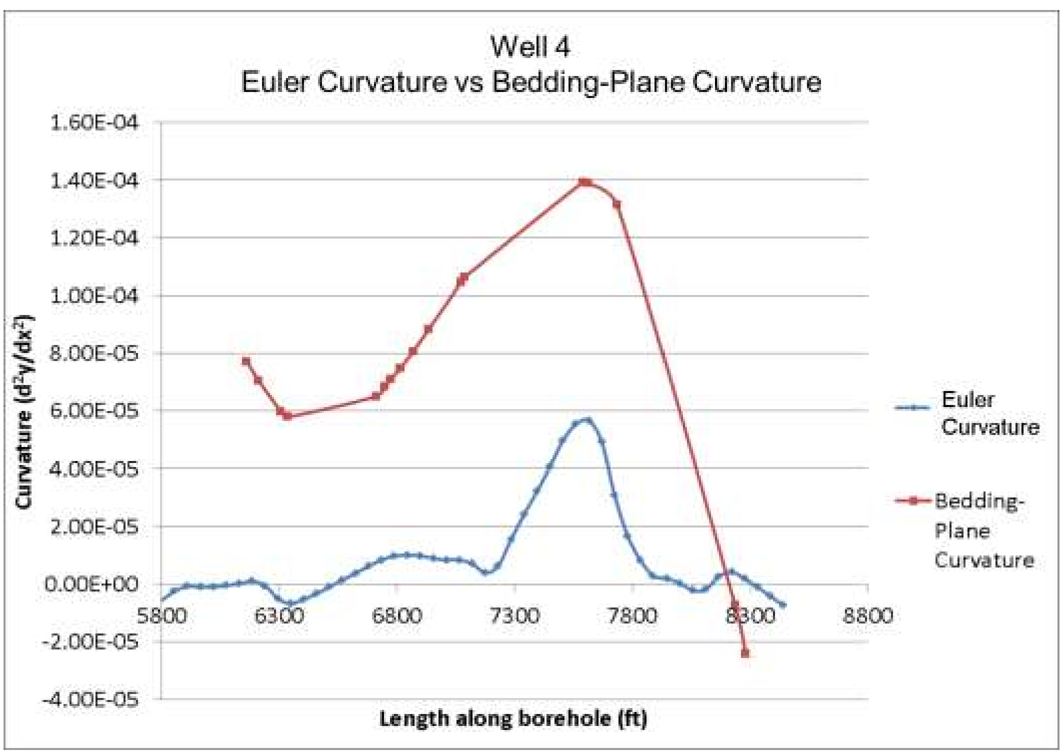

Fig. 28 – Bedding-Plane Curvature from Well 4 appears to follow similar trends as Euler Curvature.

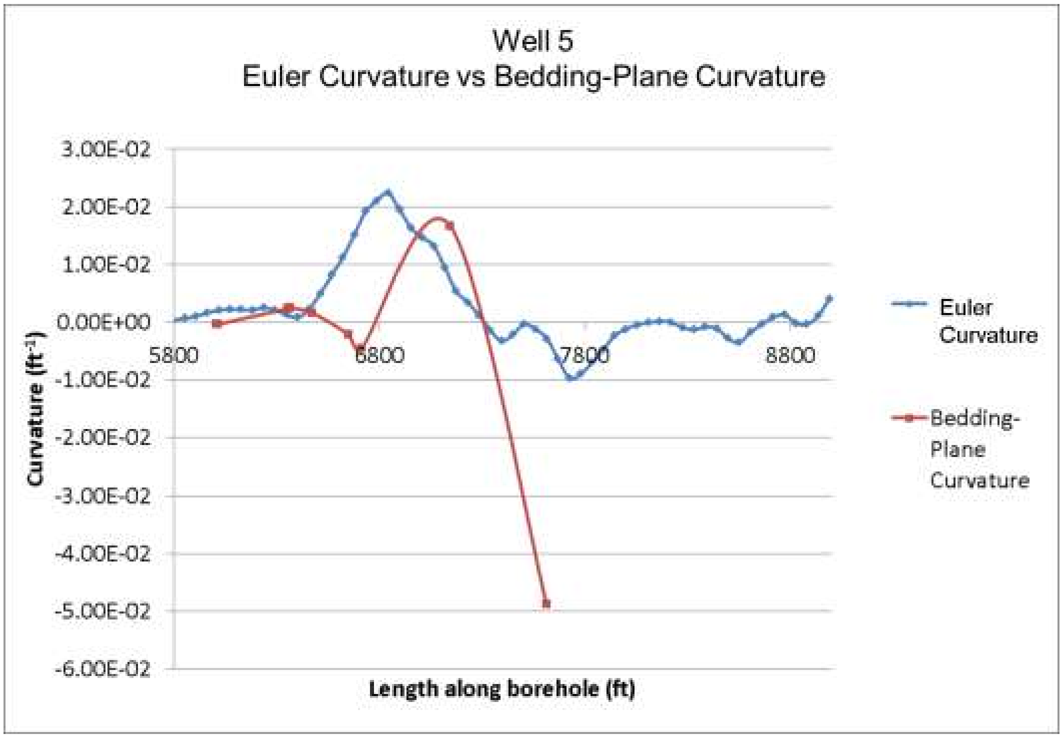

Fig. 29 – Bedding-Plane Curvature from Well 5 appears to follow similar trends as Euler Curvature.

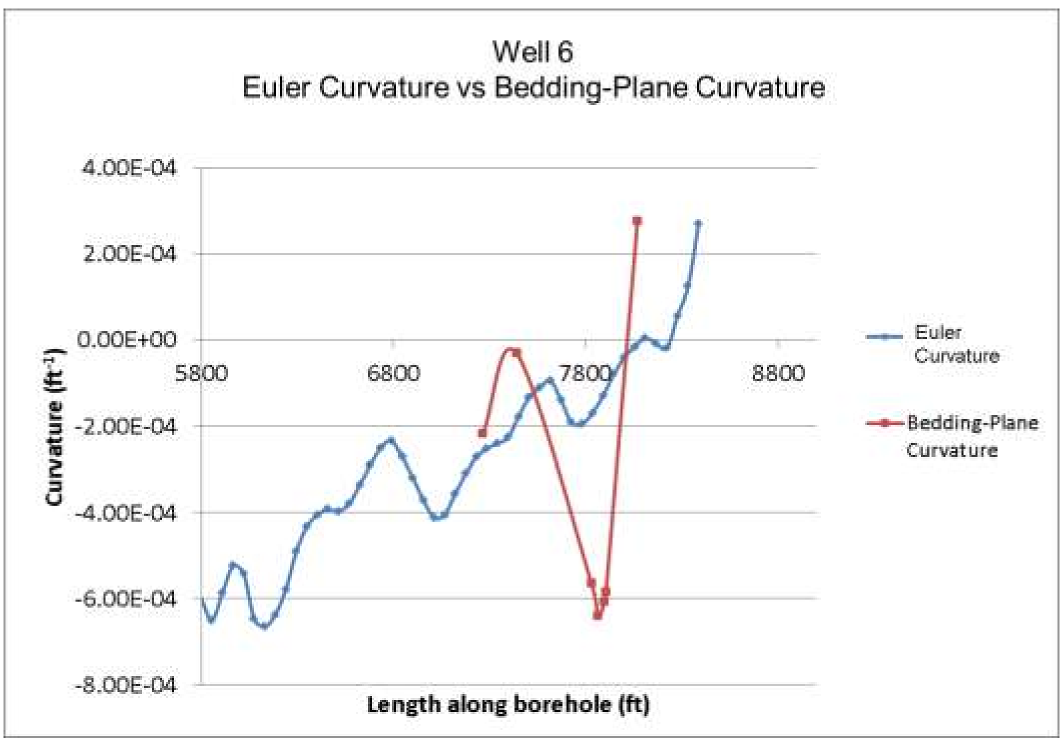

Fig. 30 – Bedding-Plane Curvature from Well 6 appears to follow similar trends as Euler Curvature.

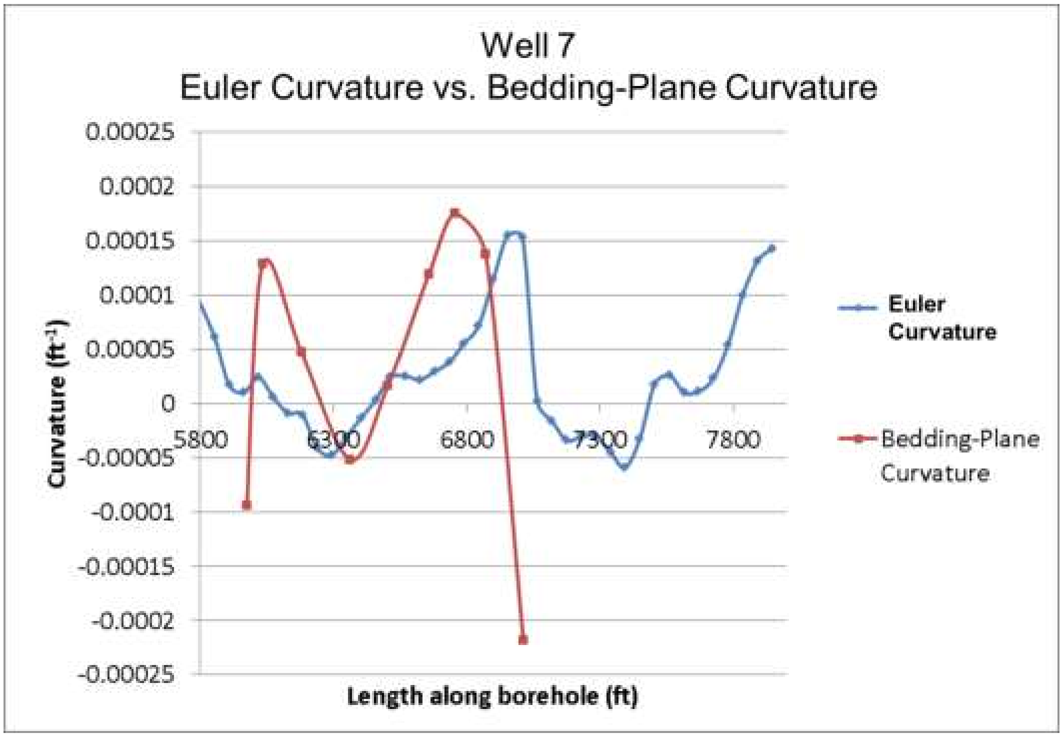

Fig. 31 – Bedding-Plane Curvature from Well 7 appears to follow similar trends as Euler Curvature.

Borehole Synthesis

Fracture Density: Fracture strike orientations are relatively consistent in Wells 1-4 and 6-7 in that one fracture set is oriented in a general southwest to northeast direction. Well 5 has a strike orientation that is consistent with a secondary fracture set in Well 4. In Wells 2, 4, and 6 two fracture sets are observed. Fracture strike orientation in Wells 2 and 6 is nearly perpendicular suggesting different mechanisms of fracturing, while Well 4 appears to have a conjugate fracture set with the fractures oriented northwest to southeast being the secondary set.

Curvature: Similar trends between bedding-plane and Euler curvature suggest that curvature is a good measure of structural curvature in the subsurface. Azimuths every 15° from -90° to 90° were used to calculate Euler curvature. The closest azimuth to the borehole direction was used for each well.

Seismic Analysis

Methods

The original pre-stack-time-migrated (PSTM) data suffer from acquisition footprint, which biases sensitive calculations such as curvature and coherence by adding a grid pattern to the seismic data. Acquisition footprint is most likely due to small survey size and limited fold during seismic acquisition and was removed using a footprint suppression" workflow described in detail by Davogustto (2011) (Fig. 32). Footprint suppression removed noise in the center with some removal along the edges of the 3D-seismic survey, but residual noise remains in the survey, especially along the edges of the survey where the fold is low relative the center.

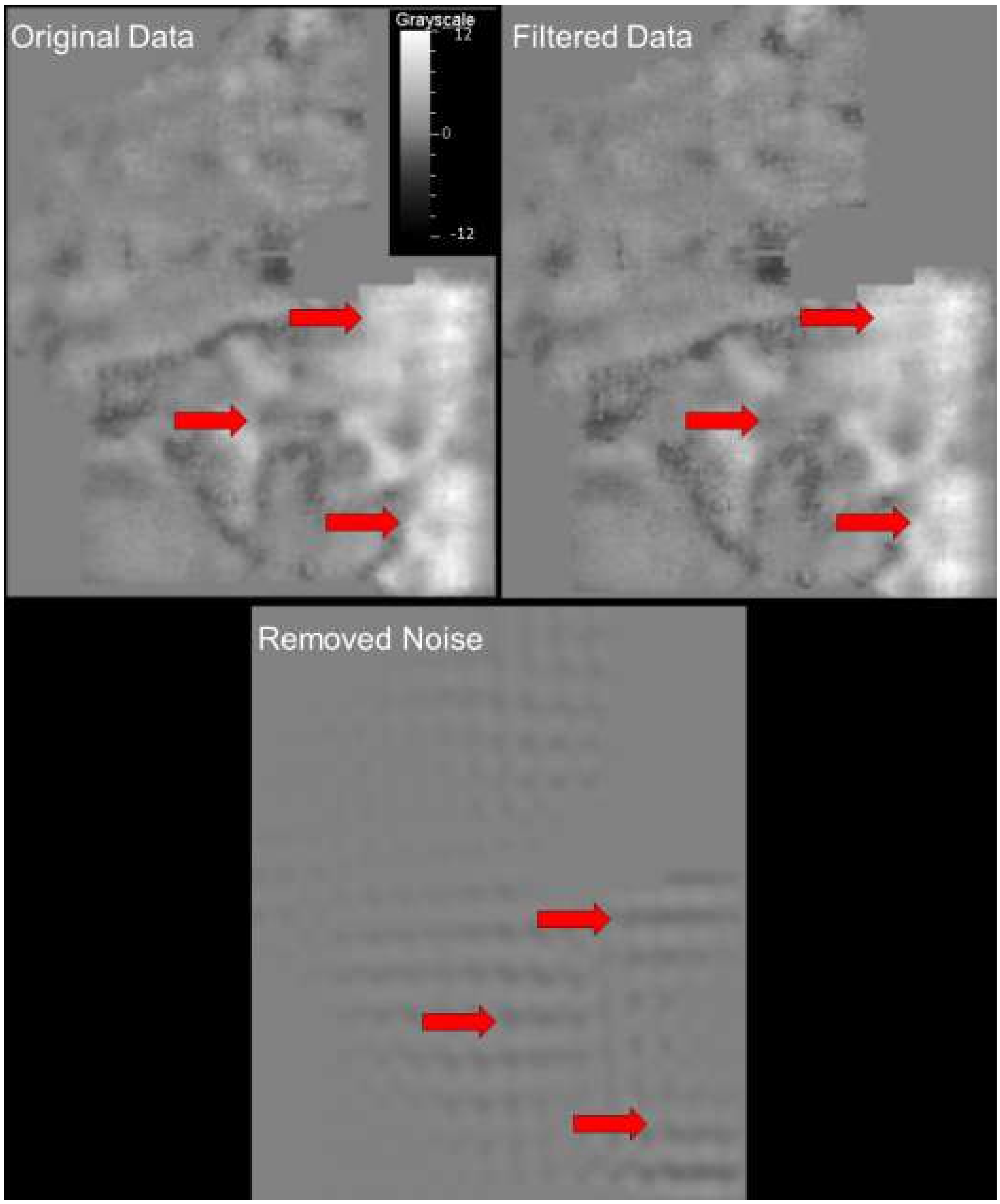

Fig. 32 - Initial footprint in PSTM seismic data (top-left). Footprint removed from data (bottom). Filtered data (top-right) with red arrows showing before, after, and what was removed.

The present seismic interpretation is based on three horizons – Hunton Group, Sylvan Shale, and Viola Limestone, which were identified from synthetic-well ties from the vertical wells in the 3D-seismic area. The seismic data were depth converted, and horizontal well paths were loaded into the project to enable visual and quantitative correlation between seismic data and wellbore locations. Fig. 33 shows the Hunton horizon, as interpreted from the 3D-seismic volume with a vertical exaggeration of 1:5 to enhance geologic structure in the area.

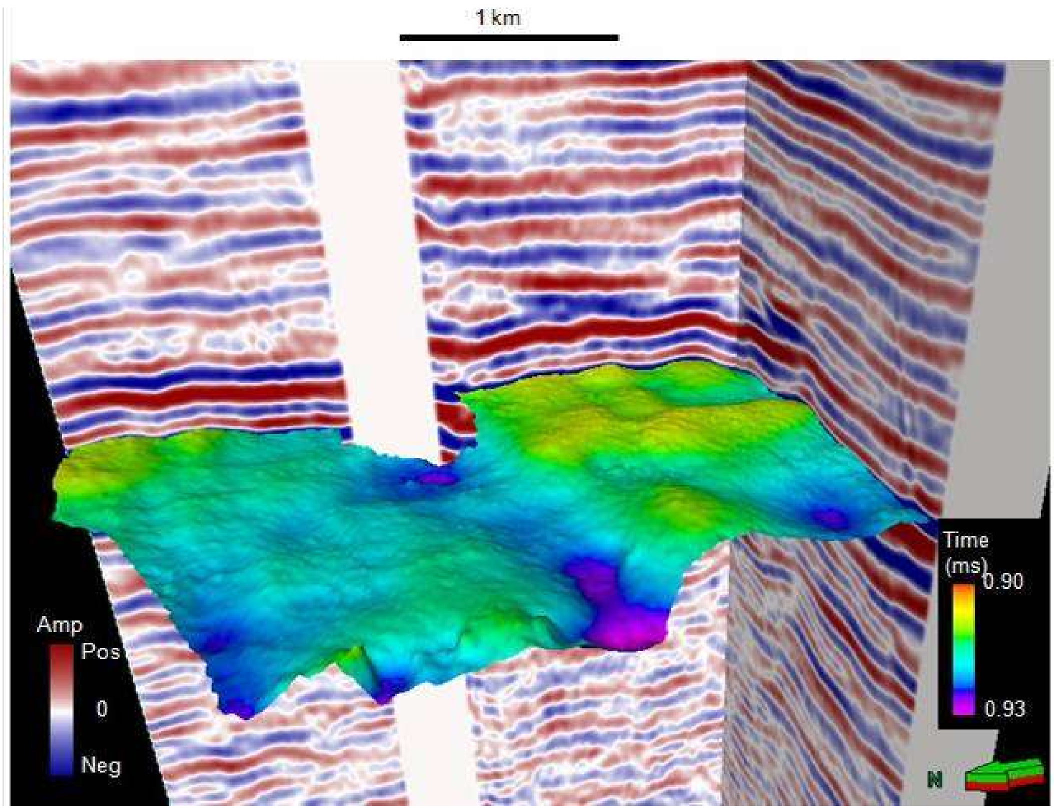

Fig. 33– Hunton Group horizon interpreted from 3D-seismic data.

After horizon interpretation, volumetric curvature was calculated to identify subsurface structures and applied to the interpreted Hunton Group Horizon. Fig. 34 illustrates horizon slices along the top of the Hunton Group through most positive, negative, long-wavelength, and short-wavelength and most principal curvatures using both filters. Long-wavelength curvature is assumed to relate to regional structures, such as large-scale folds, whereas short-wavelength curvature represents local features like karst topography, collapse features, and in my case, acquisition footprint (Chopra and Marfurt, 2007).

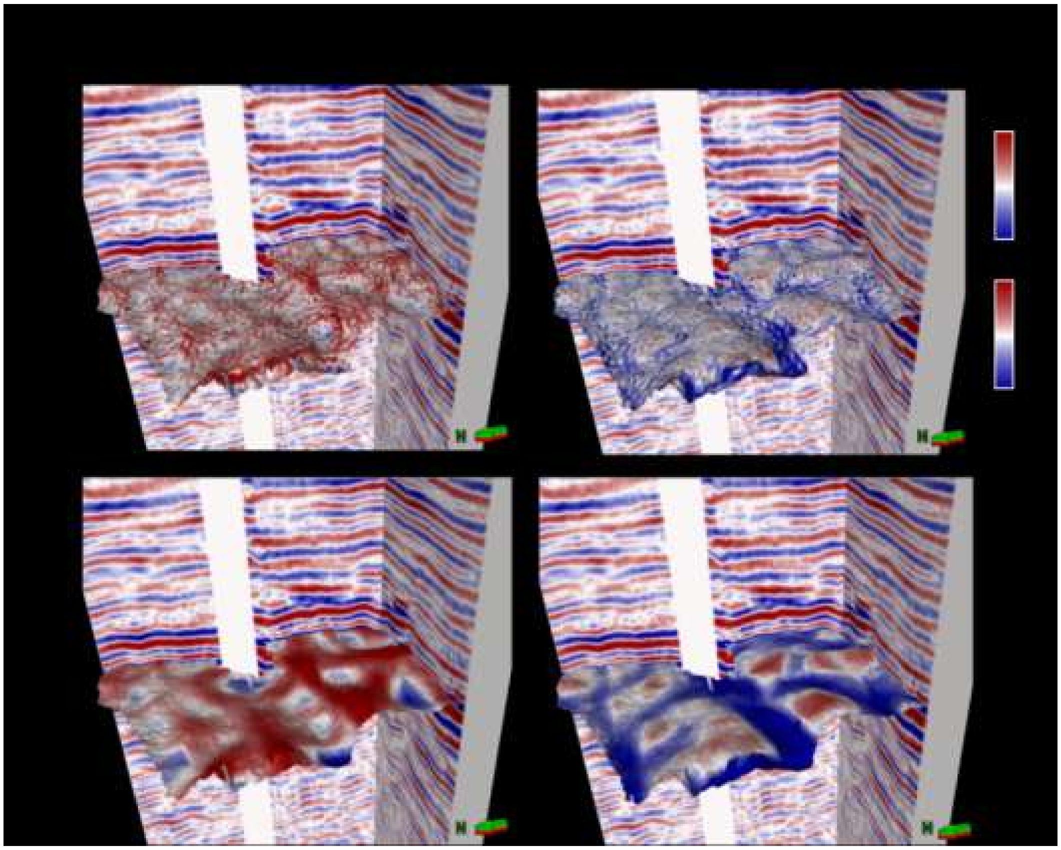

Fig. 34 – Left column is most positive curvature; right column is most negative curvature; top row is short-wavelength curvature; and bottom row is long-wavelength curvature.

Coherence was calculated next to identify lateral discontinuities in the 3D-seismic data. Seismic coherence measures lateral similarity or continuity between seismic traces. Chopra and Marfurt (2007) define coherence as the energy of the coherent part (average for semblance, KL-filtered for eigenstructure) of seismic traces divided by the average acoustic energy of input seismic traces. Fig. 35 shows coherence or similarity cross-correlation between two seismic traces where one trace is held constant while only a 40 ms window of another is shown.

Sliding the 40 ms window along the entire first trace enables cross-correlation between to the two traces. Areas where correlation is either high or low are coherent or incoherent respectively. Faulted or fractured zones typically do not exhibit high lateral continuity, but unfaulted areas often appear continuous. Fig. 36 displays the coherence attribute with areas of high coherence in white, low coherence in gray-black, and horizontal wellbores shown in red.

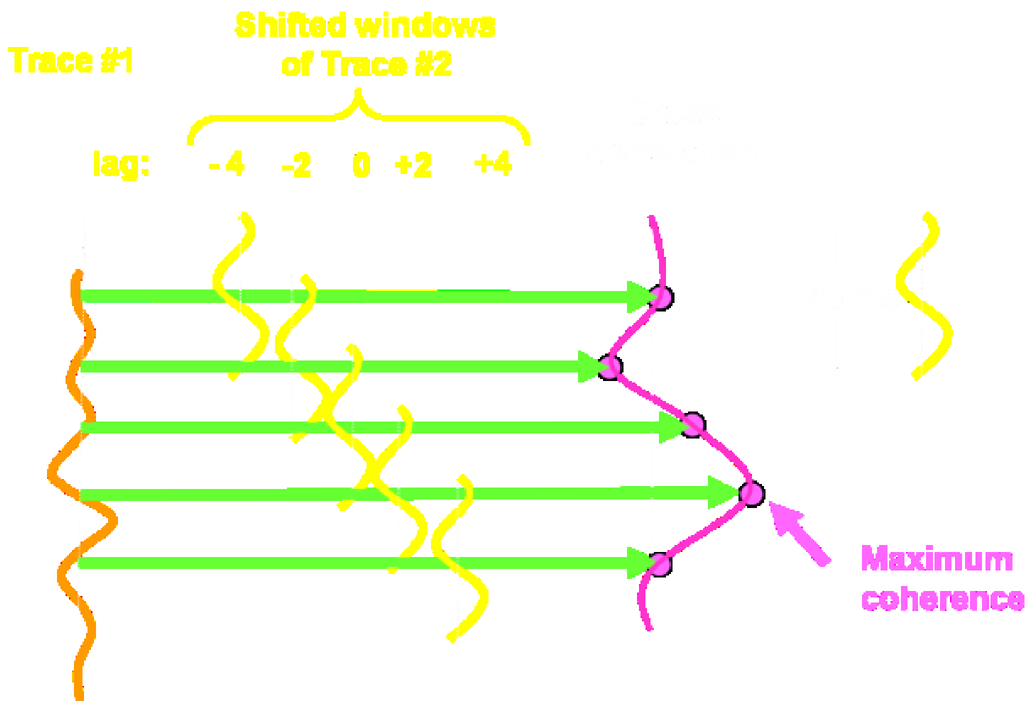

Fig. 35 – Two seismic traces where one is held constant while a window of the other is slid along the first while doing a cross correlation between the two. The area of highest cross correlation is the area of maximum coherence. Image courtesy Kurt Marfurt.

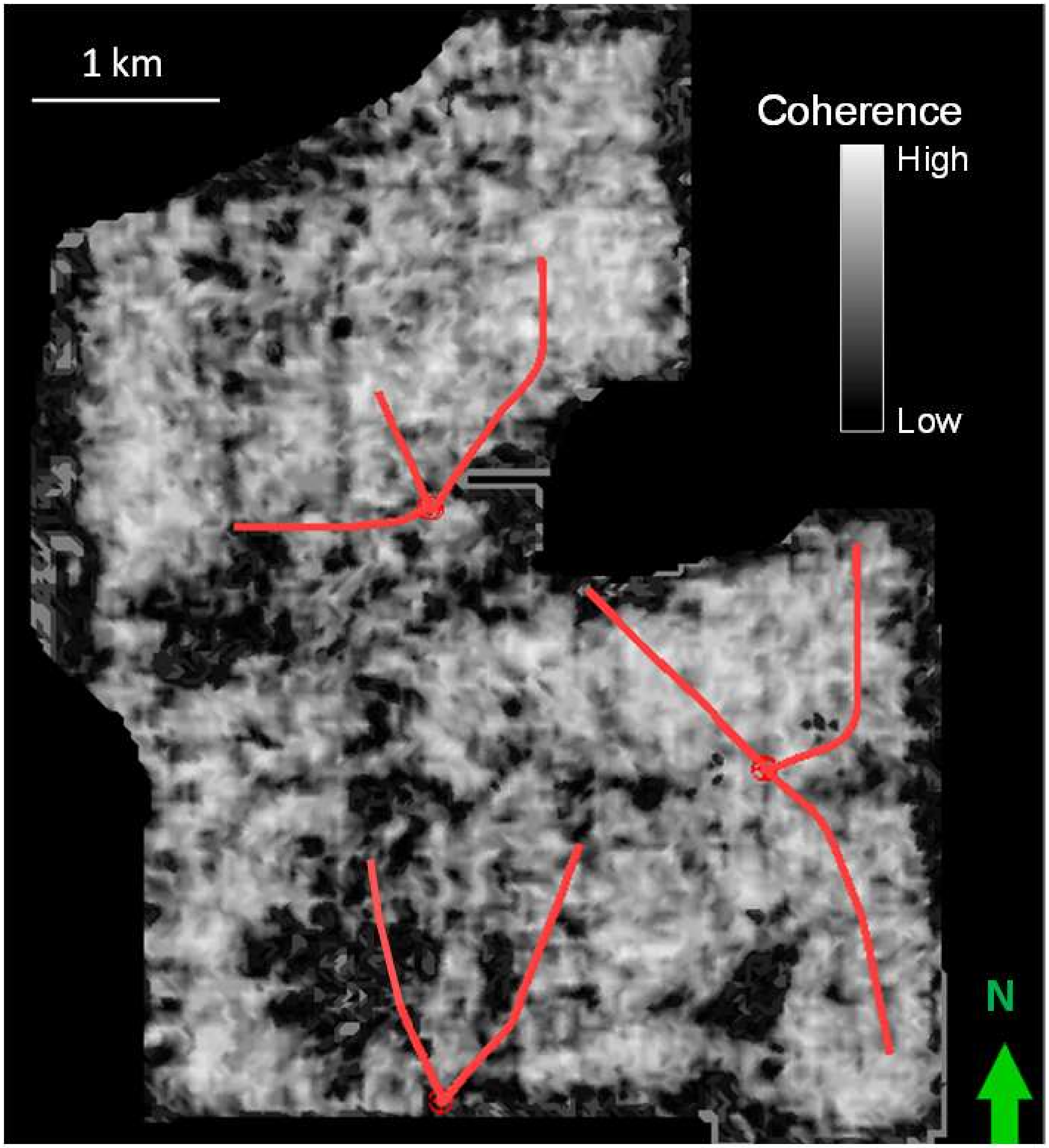

Fig. 36 - Coherence attribute with light colored areas being coherent, and dark colors incoherent. The red lines are horizontal wellbores overlaid on the seismic data.

Coherence measures lateral continuity of seismic horizons and curvature identifies layer bending such as anticlines and synclines. Chopra and Marfurt (2007) show that blended or mixed displays of two seismic attributes enable the interpreter to show both images at the same time for every calculated point. Applying this idea to coherence and curvature provides improved fault- and fracture-zone identification (Fig. 37).

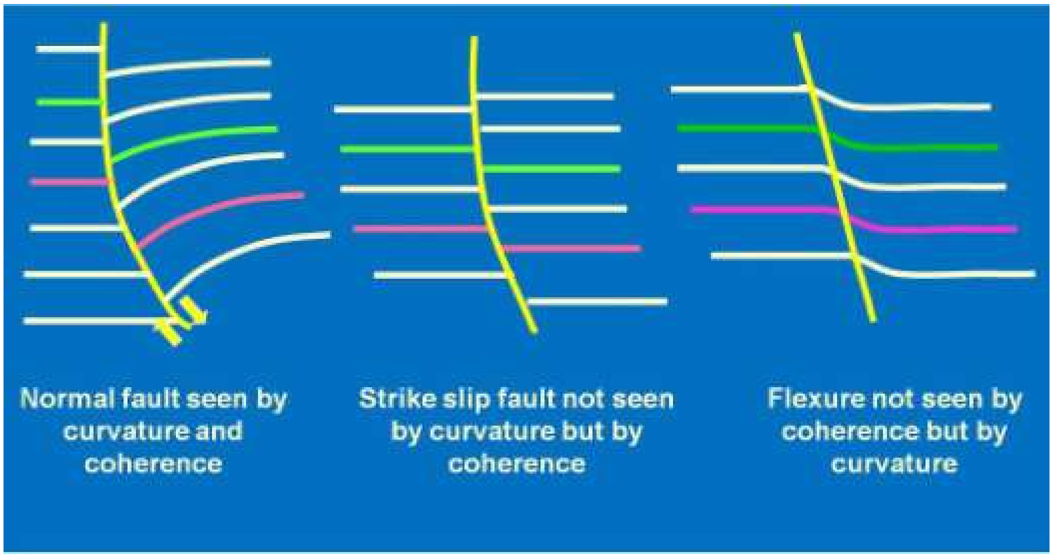

Fig. 37 – Normal fault (left) imaged by curvature and coherence. Strike-slip fault (middle) identified by coherence. Flexure (right) where no fault exists, detected by curvature.

On the left, a normal fault has flat horizons in the footwall, curved horizons in the hanging wall, and a significant amount of throw. Because the horizons are continuous up to the fault and discontinuous across it, the coherence attribute will identify it. The flexed portion of the hanging wall will be visible in the curvature attribute since the layers are bent. A similar analysis would apply to a reverse fault. The strike-slip fault has planar horizons and small vertical offset (center, Fig. 37), but it is enough to make the horizons discontinuous across the fault. Again, the coherence attribute will "see" the strike-slip fault, but because the horizons are flat, there is no curvature anomaly and k=0. Fig. 37 (right) shows multiple horizons have been flexed but are not displaced; thus, the coherence attribute will miss this structure, but curvature will be calculated in the flexed regions. Therefore, blending curvature and coherence, increases the probability of identifying fault- and fracture-zones, particularly on curved structures where hinge zones may have significant fracturing due to bending. Fig. 38 (wellbores in red) co-renders the curvature and coherence attributes with coherent areas set to be transparent (Fig. 39) allowing one to recognize areas of high curvature and low coherence. Attribute blending shows where fracture and fault zones are likely to exist based on well paths overlain on a horizon-slice.

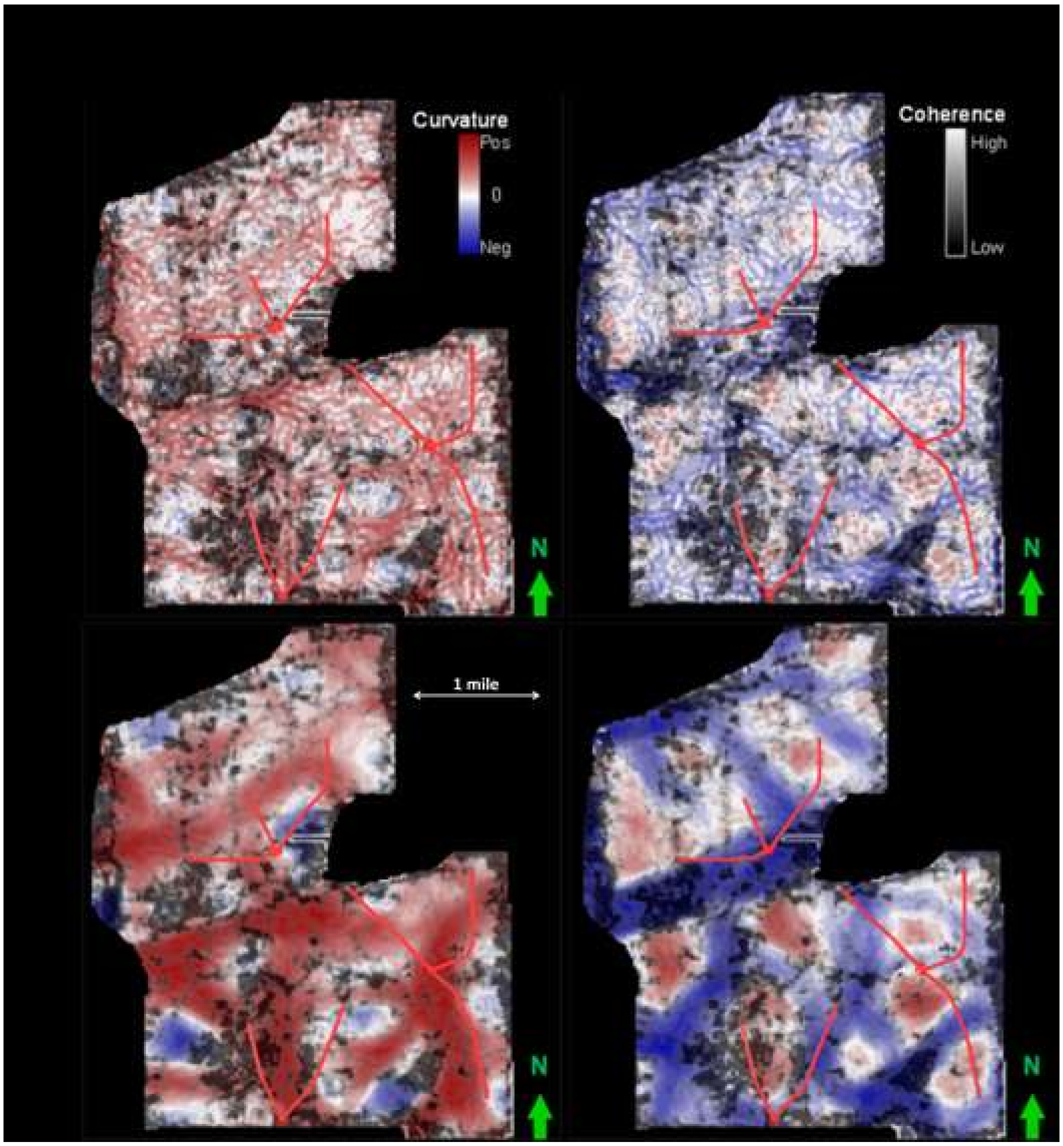

Fig. 38 – Curvature and coherence are blended together to enable visual identification of potential fracture zones in the subsurface.

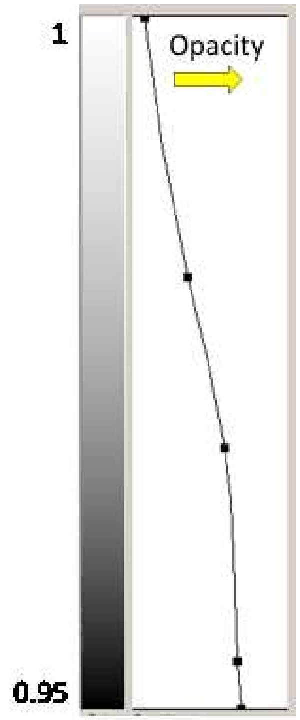

Fig. 39 – Coherence colorbar and opacity curve used in attribute blending.

Fracture Zone Analysis Results

Seismic-fracture-zone analysis consisted of several steps. Initially, results of image-log-fracture analysis were grouped into 55-ft data bins along the wellbore. Preliminary comparisons between curvature and fracture density were obtained visually by overlaying the horizontal-well-fracture-density data on a k_1-curvature-horizon slice of the Hunton Group (Fig. 40). Yellow arrows indicate areas of high fracture density (red, orange, and yellow) that visually correspond to high curvature (red).

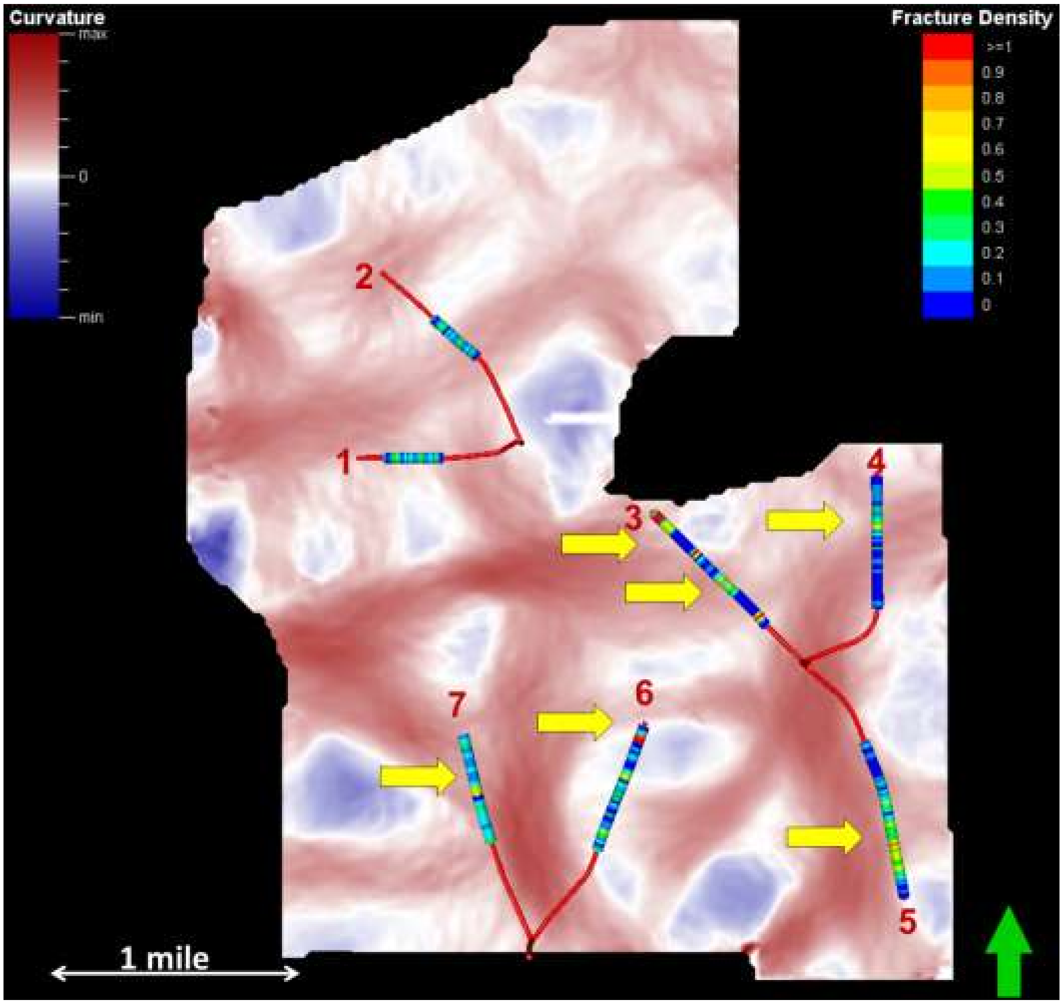

Fig. 40 – k_1 curvature applied to Hunton Group horizon. Positive structures (red) visually compare (yellow arrows) to high fracture density in Wells 3 - 7.

Next, curvature values were extracted along each wellbore providing curvature values for every 55-ft data bin. Initially, curvature values were extracted manually from the surface of the Hunton Group horizon, but horizontal wells are not always parallel to the reflector surface of the Hunton Group horizon. Therefore, it was determined that values along the borehole rather than the top of the Hunton Group horizon were more reliable for correlation with fractures from the borehole (Fig. 41).

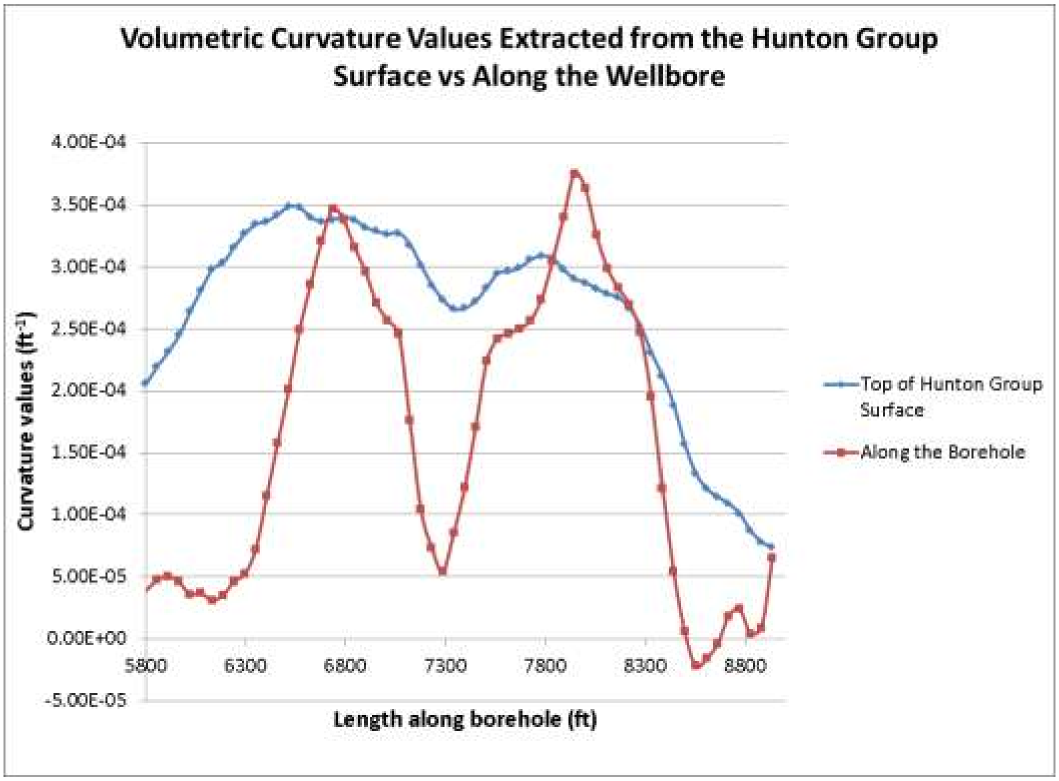

Fig. 41 – Comparison between volumetric-curvature values applied to the seismically mapped top of the Hunton Group horizon and volumetric-curvature values applied to the borehole. Both exhibit similar trends, but since the borehole is not always parallel to the top of the Hunton Group surface curvature values from the borehole were used in correlation between curvature and fracture density.

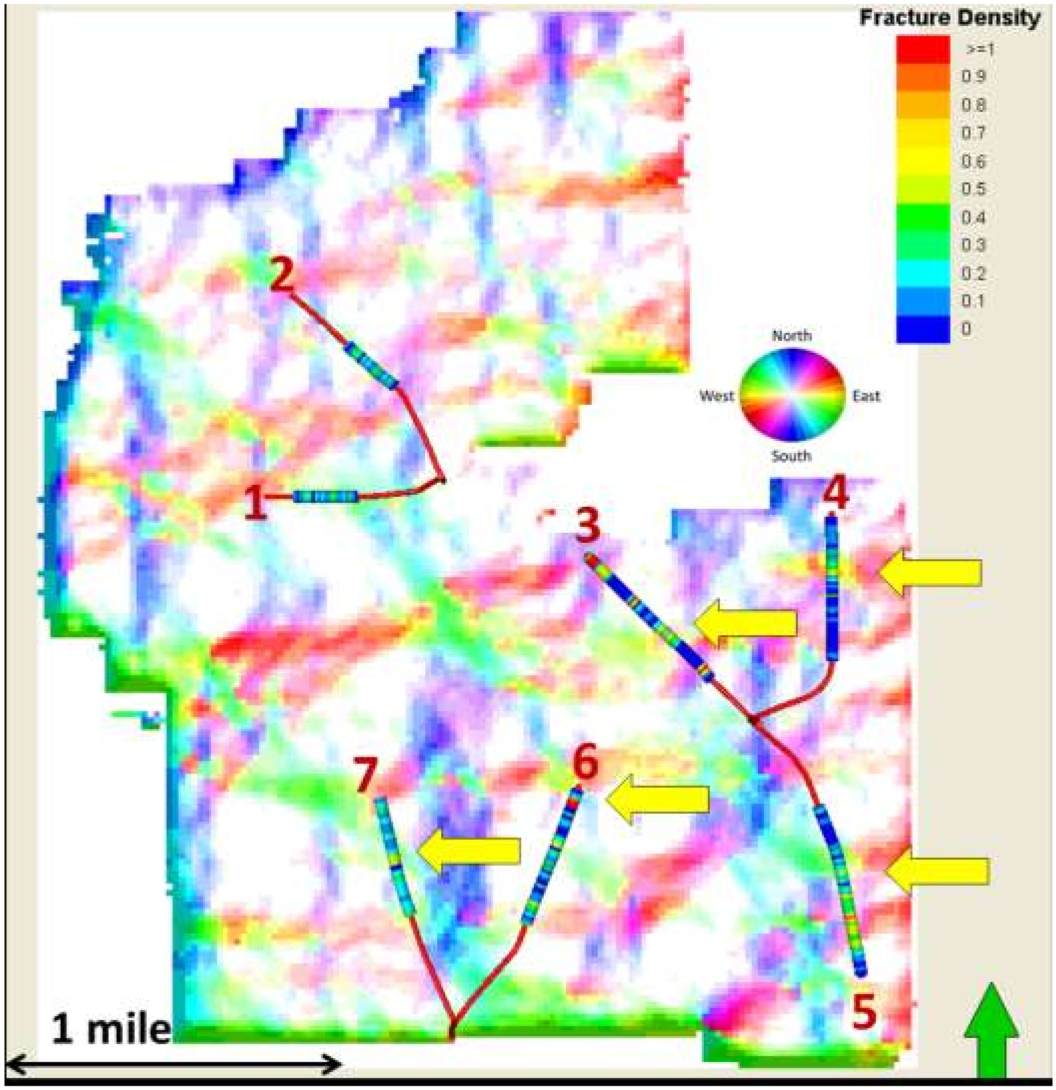

Fig. 42 – k_1 curvature plot with k_1 strike colored by strike azimuth with areas of high fracture density in horizontal wells that correspond to general east to west striking lineaments indicated by yellow arrows.

In the next step, I identified the strike direction for high curvature values by plotting the k_1 strike direction on the k_1 curvature attribute with color denoting the direction as shown by the time slice (Fig. 42) with the horizontal wells colored by fracture density. Lineaments striking in a general east to west direction visually correspond with high fracture density in Wells 3 – 7. Wells 1 and 2 do not appear to cross lineaments with similar orientations. In order to examine possible correlations between fracture sets and the strike of curvature lineaments, I used a workflow developed by Guo et al. (2010) that computes an azimuthally-limited weighted average of curvature lineaments.

In Fig. 43, a 3D-seismic survey is shown with two fracture sets, one striking northwest to southeast and the other southwest to northeast (Nissen et al., 2009). Azimuthal intensity is calculated by taking the total strike length and dividing it by the total area of the search window for a given azimuth. This technique is similar to fracture intensity calculations performed on the clay models, but filters curvature lineaments by azimuth. In Fig. 43, if an azimuthal intensity calculation were performed in the northeast direction, the red circle would have high azimuthal intensity relative to the blue circle since more red fractures fall within the red circle. In contrast, if azimuthal intensity were calculated in the northwest direction, the blue circle would have high azimuthal intensity relative to the red circle since more blue fractures are located in the blue circle.

Figs. 44 and 45 show azimuthal intensity calculated on the 3D-seismic data for azimuths 30° and -30°. Red, yellow, and green indicate areas of high curvature in the given azimuth, while blue colors show little to no azimuthal intensity. I calculated azimuthal intensity every 15° from 0° to 180° azimuth.

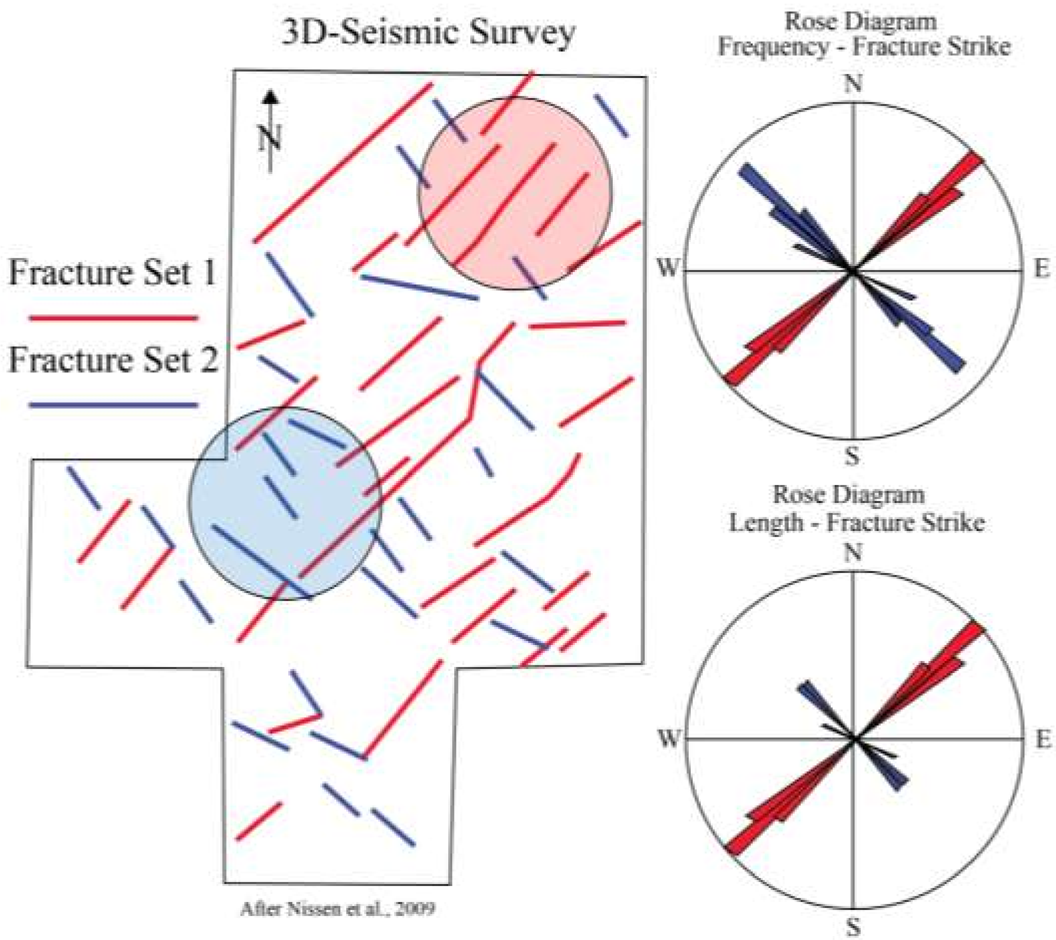

Fig. 43 – Schematic with two fracture sets in a 3D-seismic survey. The top rose diagram shows frequency of fracture strike, colored by fracture set. The bottom rose diagram shows length of fracture strike colored by fracture set. The two circles in the 3D-seismic survey are colored according to the relative fracture strike intensities. After Nissen et al. (2009).

Next, I cross-correlated azimuthal intensity values with fracture density from horizontal-borehole-image logs and found that correlations, r, exist where fractures in image logs have similar strike orientation as the calculated azimuthal intensity (Table 5). In Excel ®, I used fracture density and azimuthal intensity as the respective x and y data. Then correlation, r, was calculated using n data points of fracture density, the interpreted slope (*m*) from subsequent scatter plot, and the calculated y-intercept (*b*) by:

$$r = \frac{n\sum(xy) - \sum x \sum y}{\sqrt{[n\sum(x^2) - (\sum x)^2][n\sum(y^2) - (\sum y)^2]}} \tag{7}$$

After identifying areas of high azimuthal intensity, I correlated positive curvature values to fracture density in these same areas and found linear correlations, r, between fracture density and positive curvature again using Excel ® (Table 6).

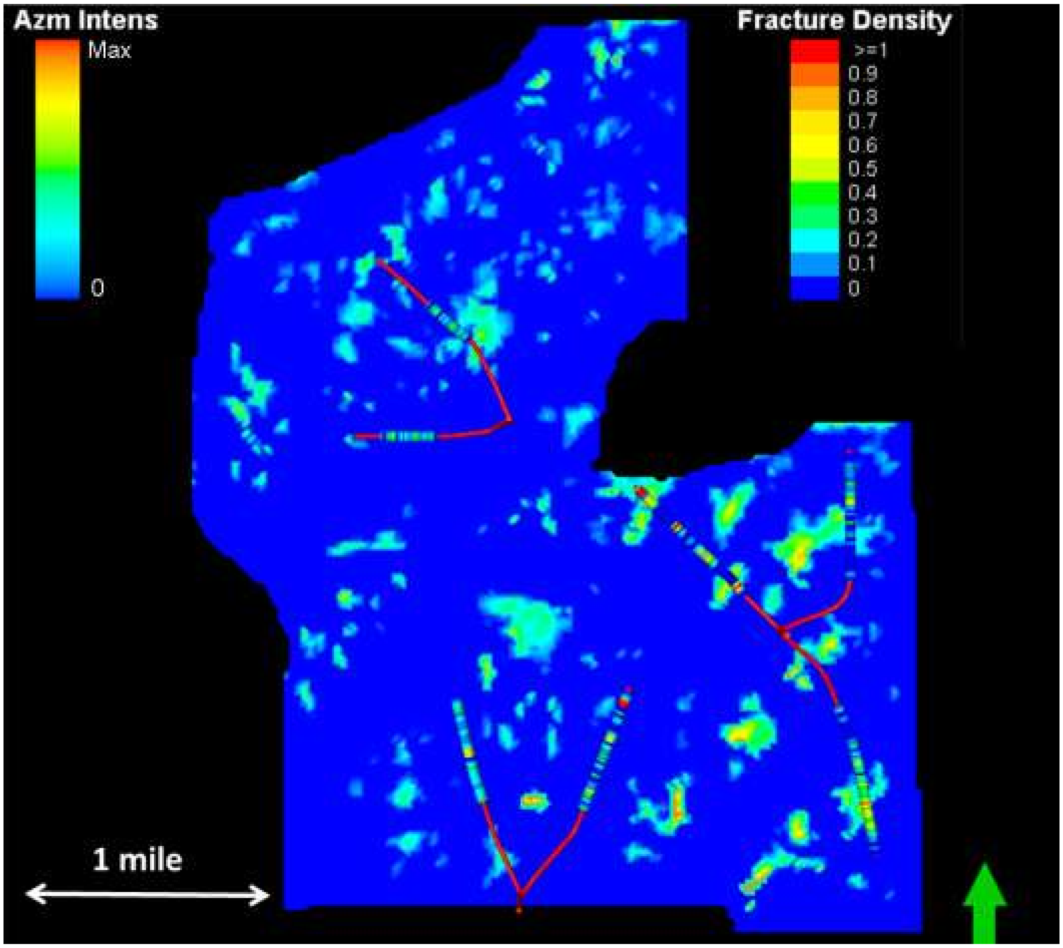

Fig. 44 – Azimuthal intensity for 30°. Red, yellow and green indicate high azimuthal intensity and blue indicates low to 0 azimuthal intensity in the respective direction.

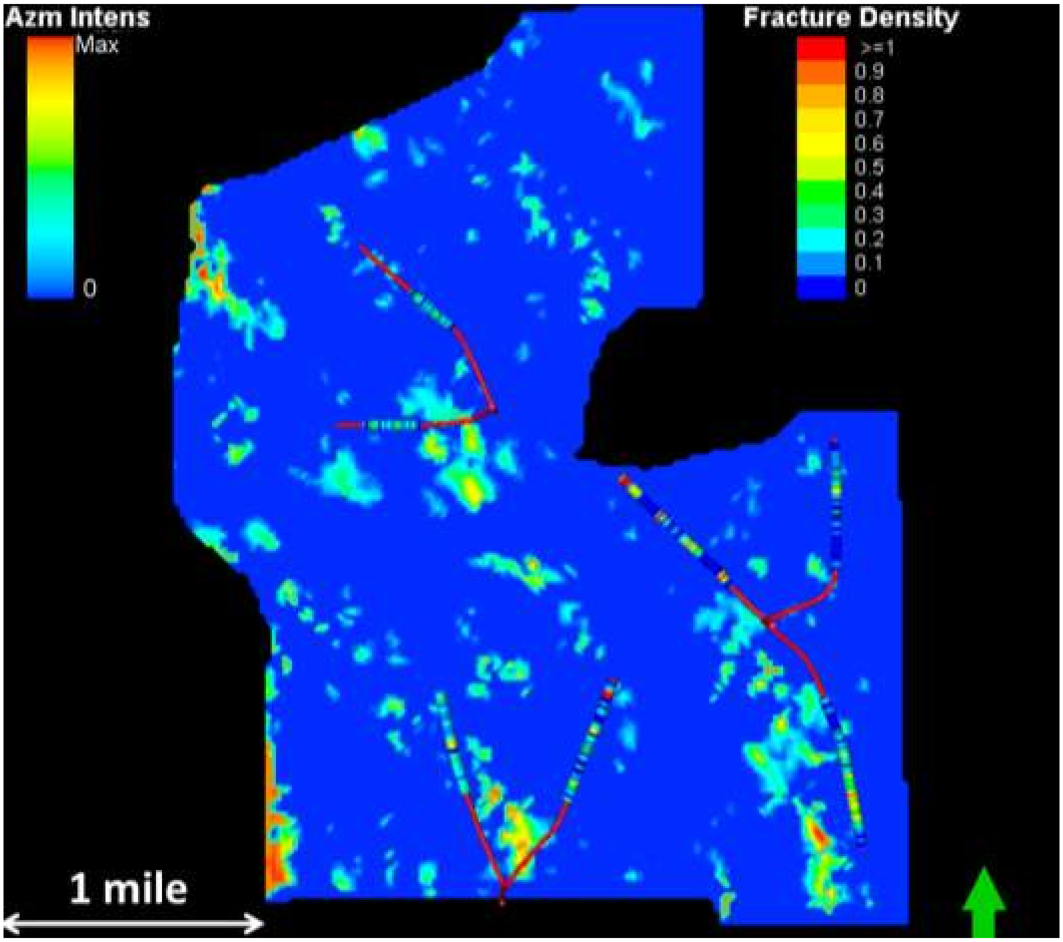

Fig. 45 – Azimuthal intensity for -30°. Red, yellow and green indicate high azimuthal intensity and blue indicates low to 0 azimuthal intensity in the respective direction.

Table 5 – Azimuthal Intensity Correlations to Fracture Density

Table 5			
Well Number	Correlation (r)	Azimuth	Measured Length Along Wellbore (ft)
1	No correlation	---	---
2	0.69	45	5800 - 6290
3	0.77	75	5400-6230
3	0.88	45	7275-7605
4	0.80	75	7120-7560
5	0.70	45	7890-8495
5	0.57	-75	6405-6955
6	0.66	-75	7065-7505
7	0.69	-75	5800-6185

Table 6 – Curvature Correlations to Fracture Density

Table 6				
Well Number	Correlation (r)	Curvature	Azimuth	Measured Length Along Wellbore (ft)
1	No correlation	N/A	---	---
2	0.61	Positive	45	5800 - 6290
3	0.72	Positive	75	5400-6230
3	0.66	Positive	45	7275-7605
4	0.67	Positive	75	7120-7560
5	0.75	Positive	45	7890-8495
5	0.53	Positive	-75	6405-6955
6	0.67	Positive	-75	7065-7505
7	0.74	Positive	-75	5800-6185

After correlating positive curvature to high fracture density, I attempted to identify anticlines and synclines in the subsurface to assist fracture zone identification. Bergbauer et al. (2003) showed that cross plotting values of k_1 and k_2 curvature indicate different geometric shapes. The shapes created are as follows: $k_1>0$ and $k_2>0$ is a dome; $k_1>0$ and $k_2=0$ is an anticline; $k_1>0$ and $k_2<0$ is a saddle; k_1=0 and k_2<0 is a syncline; k_1<0 and k_2<0 is a bowl; and k_1=0 and k_2=0 are planes. I used this method to filter curvature according to shape.

Fig. 46 illustrates the relationship between geometric shapes and principle curvature values. Fracture densities per 55-ft-bin spacing in all wells are plotted on a k_1-k_2 graph (Fig. 47). The anticlinal zone ranging between dome and saddle geometry accounts for 57% of all fractures while the synclinal zone between saddle and bowl geometries accounts for 43% of all fractures. The minor disparity between fractures in the anticlinal and synclinal zones probably reflects the choice of drilling preferentially in structural highs (anticlines).

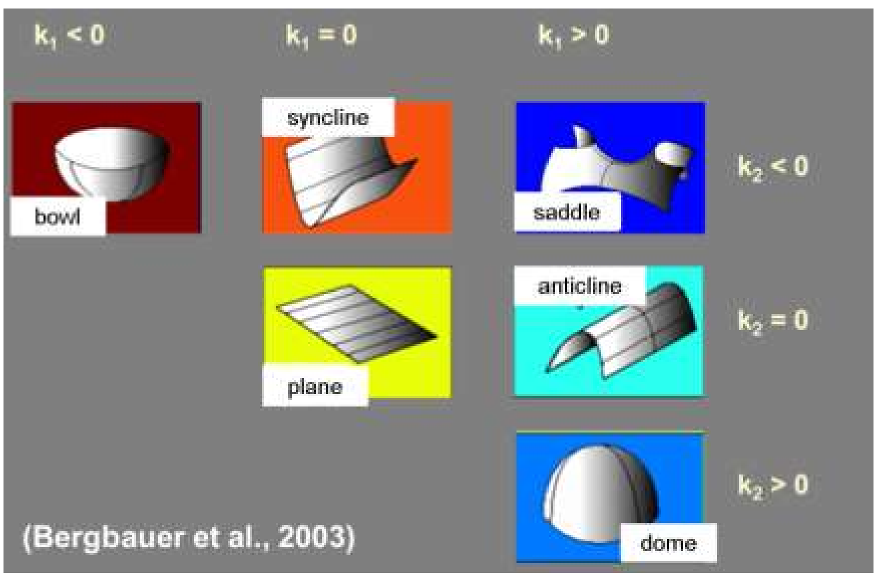

Fig. 46 – Geometric shapes indicated by k_1 and k_2 values

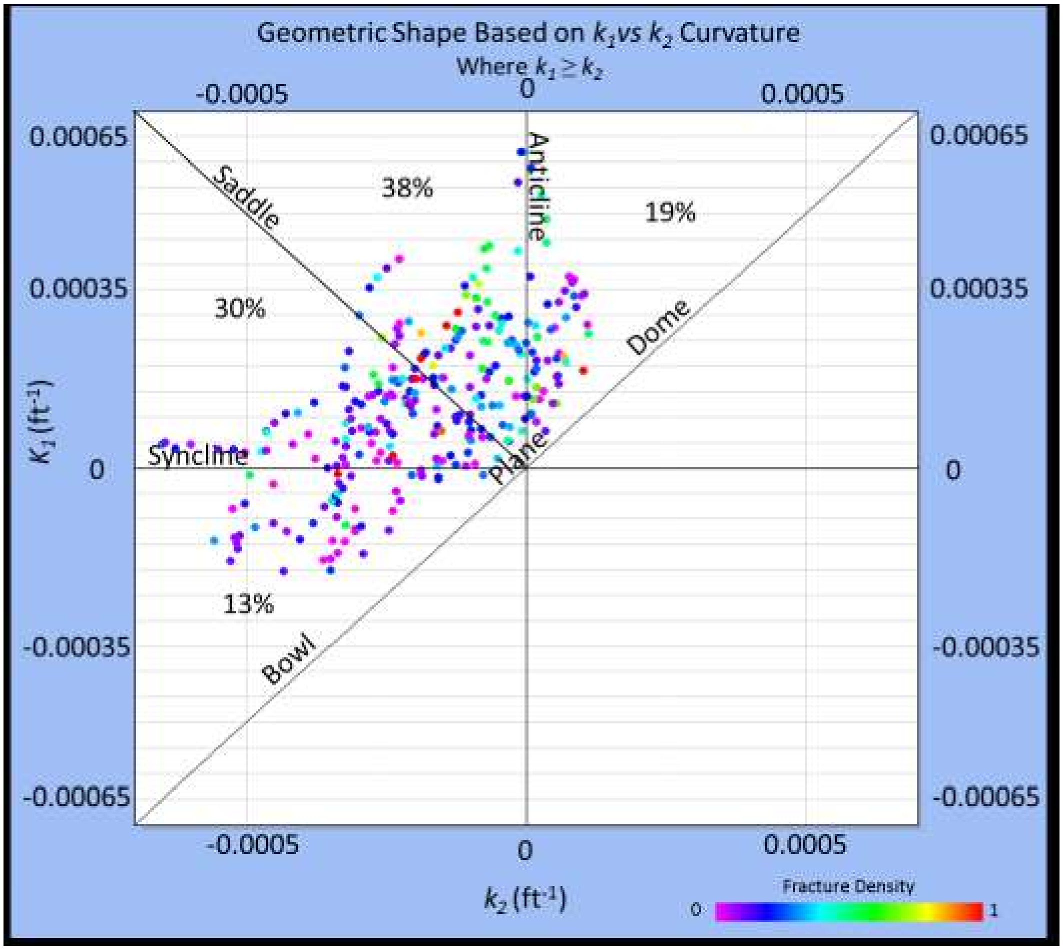

Fig. 47 – Geometric shapes in the subsurface identified by cross-plotting positive and negative curvature values.

<u>Seismic synthesis</u>

<u>Azimuthal Intensity:</u> Areas of high fracture density in the horizontal-borehole-image logs that correlated with azimuthal intensity also correlated with high curvature values. Correlations between azimuthal intensity and fracture density suggested that azimuthal intensity of most positive curvature identifies folding generated tensile fracture zones in the subsurface.

<u>Geometric Shapes:</u> Calculations from both k_1 and k_2 curvatures assisted in the identification of subsurface structures. Low disparity between fracture percentages in anticlinal and synclinal zones suggests that strain on the edges of

subsurface folds is higher than the center of the folds as predicted by the flexural slip model (Fig. 1).

Additional Analyses

Lithology

Curvature is an important indicator of fractures in the subsurface. However, lithology of the subsurface rocks is another principal component that controls fracturing, particularly in limestones and dolomites. Fractures and faults are often more common in dolomite since it is more brittle than limestones (Cantrell et al., 2001). Ericsson et al. (1998) identified lithology and curvature as controlling factors in determining locations of high fracture density in carbonates from the Arabian Gulf. They verified this through 3D-seimsic-curvature analyses, horizontal-borehole-image logs, and core samples.

To test for the lithologic facies in the current study, I used acoustic-impedance inversion. Singleton and Keirstead (2011) show that acoustic-impedance inversion applies derived lithologic properties from well logs to 3D-seismic data allowing for qualitative-lithologic interpretation away from the borehole. I used 14 vertical wells with sonic logs to compute the acoustic-impedance inversion and then applied those values to the previously interpreted Hunton horizon.

Acoustic-impedance inversion values extracted along the wellbores were correlated with fracture density. Wells 4 and 5 correlated linearly with acoustic-impedance inversion with high impedance values correlating with high fracture densities (Fig. 48 and 49). The correlation, r, for Wells 4 and 5 were 0.56 and 0.59, respectively. Fig. 50 shows the acoustic-impedance results applied to the

Hunton Group horizon with yellow to green indicating low impedance and blue to purple showing high impedance values.

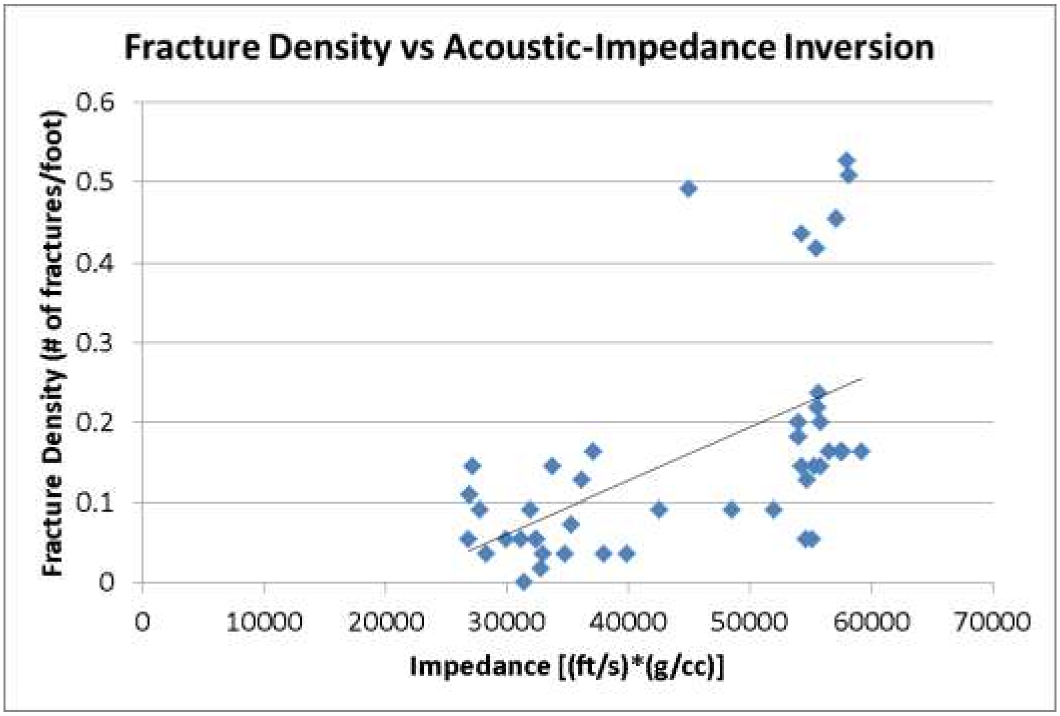

Fig. 48 – Linear relationship between fracture density and impedance in Well 4.

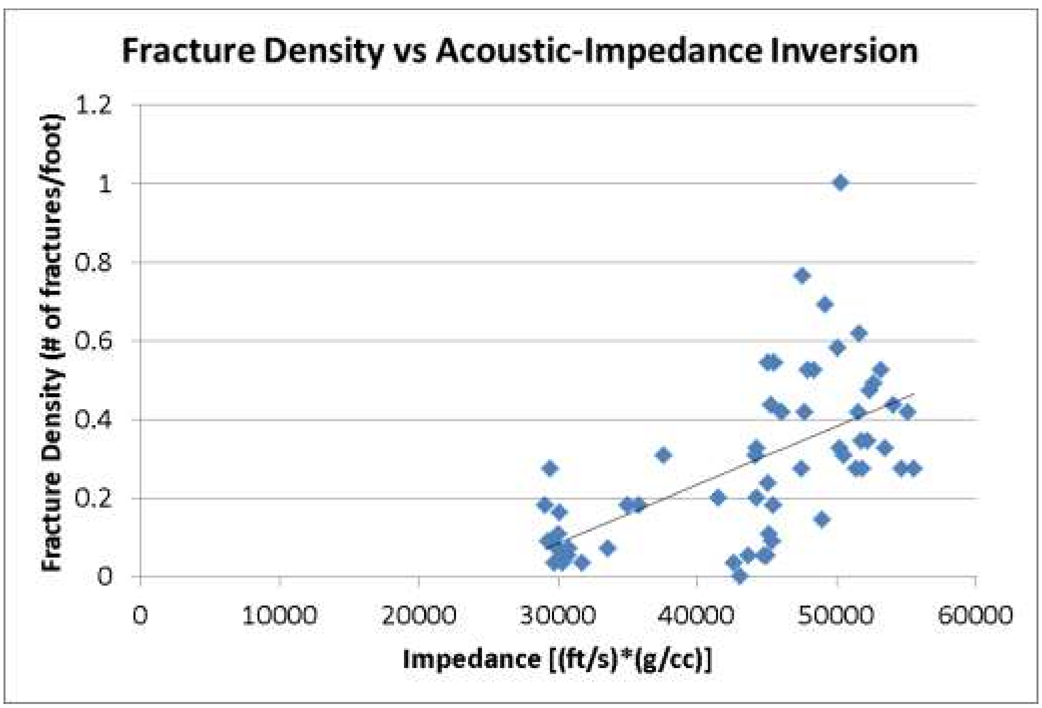

Fig. 49 – Linear relationship between fracture density and impedance for Well 5.

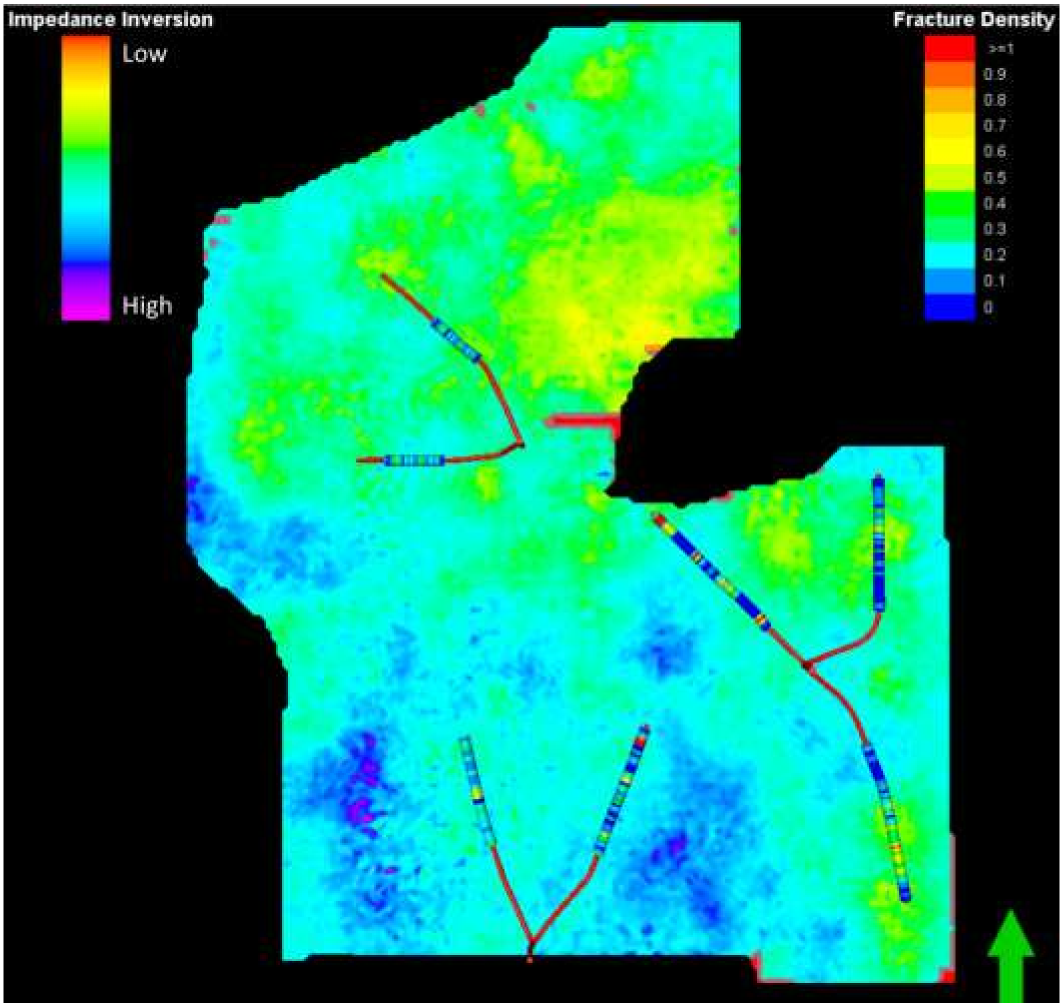

Fig. 50 – Acoustic-impedance inversion values applied to the Hunton Group horizon. Low impedance values are shown by warm colors (yellow and green) while high impedance values are shown by dark colors (blues and purple).

<u>*Layer Thickness*</u>

Another factor that has been linearly related to fracture spacing is layer thickness (e.g., Narr and Suppe, 1991; Gross, 1993; Engelder et al., 1997; Ji et al., 1998). I tested this hypothesis using an isochron map from the top of the Hunton Group horizon to the top of the Sylvan horizon. The mean Hunton Group thickness was 8.98 ms with a standard deviation of 1.81, indicating that the Hunton Group is of a similar thickness throughout the survey (Fig. 51). Correlating Hunton Group thickness and fracture density showed no significant correlation in any well. This lack of correlation suggests that any significant fracturing due to layer thickness is below seismic resolution.

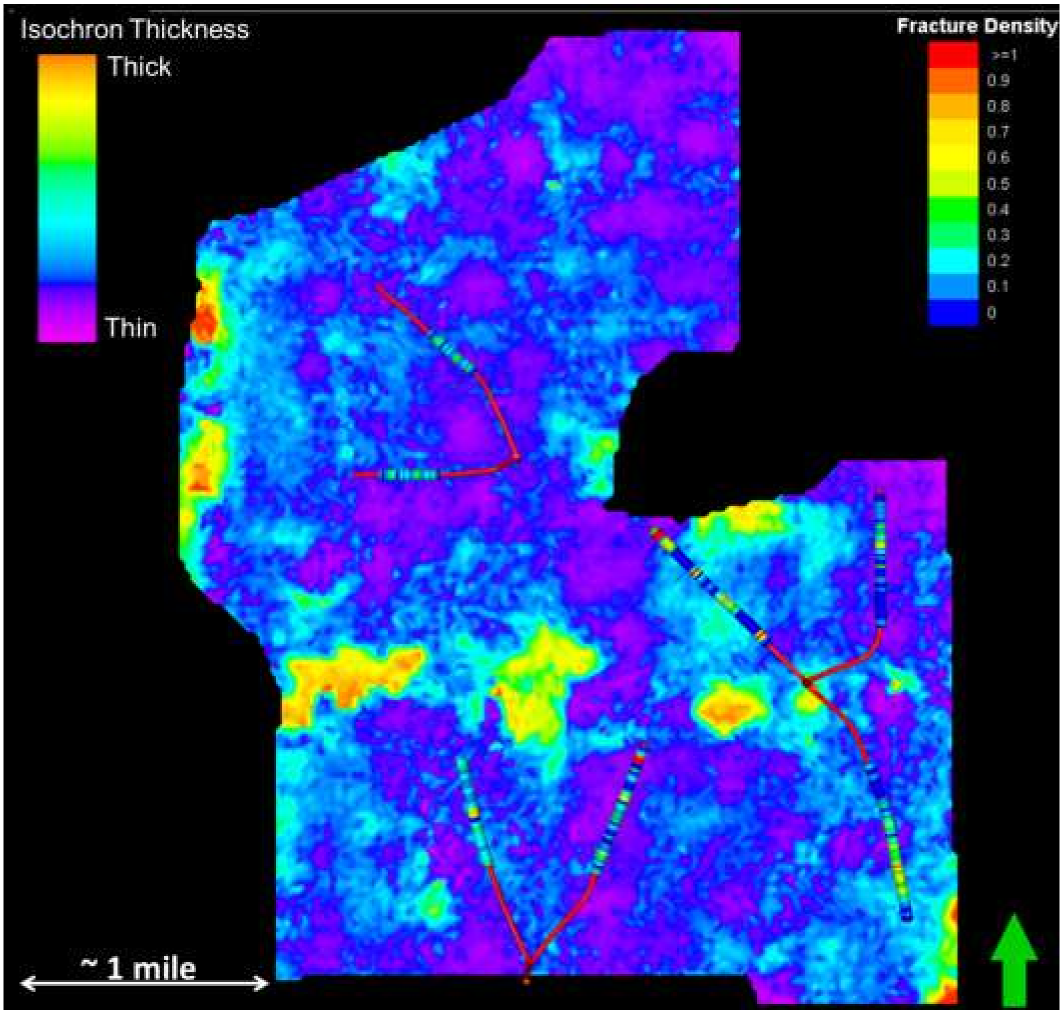

Fig. 51 – Isochron map of the Hunton Group horizon where thick areas are shown by warm colors (e.g., red, yellow, orange) and thin areas are shown by dark colors (e.g., purple and blue).

<u>Coherence</u>

Fig. 37 illustrates how curvature and coherence identify flexure and faulting in a seismic survey. Coherence values from the 3D-seismic data were extracted along the horizontal wellbores and cross-plotted with fracture densities. Well 3 had a linear correlation, r, of -0.64 indicating that as fracture densities increase, coherence decreases suggesting that lateral discontinuity of seismic traces indicates fracture zones. None of the other wells correlated with the coherence attribute.

Scaled Production

The relative effect of fractures on porosity and permeability in the hydrocarbon reservoir was shown by production data in the wells. The production data is proprietary and the numbers are scaled for oil, gas, and water production. However, the acronyms of bbl and BOE will be used as though the scaled production were accurate. Total production for oil, gas, and water was scaled between 0 to 100 with 100 being the highest amount produced in any well. Then, total scaled production per foot was calculated for the areas in the wells where image logs were acquired and interpreted. These two zones are called the imaged and interpreted zones in Table 7. Differences between the two zones will be discussed in the limitations portion of the discussion. Table 7 compares all seven wells and their scaled production of water (bbl), gas (BOE), and oil (bbl).

Table 7 – Comparison of scaled oil, gas, and water production per foot for the imaged and interpreted zones in the image logs.

Table 7						
				Total Scaled Production		
Well	Imaged Zone (ft)	Interpreted Zone (ft)		Water (bbl)	Gas (BOE)	Oil (bbl)
Well 1	3892	1225		26	22	100
Well 2	1033	490		22	15	30
Well 3	3398	3398		45	49	39
Well 4	4006	2612		39	43	77
Well 5	3753	3125		100	100	92
Well 6	3422	2634		100	30	10
Well 7	3024	2138		10	10	20
	Scaled Production/Imaged Zone (bbl or BOE/ft)			Scaled Production/Interpreted Zone (bbl or BOE/ft)		
Well	Water (bbl)	Gas (BOE)	Oil (bbl)	Water (bbl)	Gas (BOE)	Oil (bbl)
Well 1	0.007	0.006	0.026	0.021	0.018	0.082
Well 2	0.021	0.015	0.029	0.044	0.031	0.061
Well 3	0.013	0.014	0.011	0.013	0.014	0.011
Well 4	0.010	0.011	0.019	0.015	0.017	0.029
Well 5	0.027	0.027	0.024	0.032	0.032	0.029
Well 6	0.029	0.009	0.003	0.038	0.011	0.004
Well 7	0.003	0.003	0.007	0.005	0.005	0.009

Discussion: Fracture Density and Seismic Attributes

The goal of this study was to use clay models, horizontal-borehole-image logs, and 3D seismic data to correlate curvature with fracture density to enable fracture-zone identification in the subsurface. To my knowledge, only Hunt et al. (2010) and Ericsson et al. (1998) have used horizontal-borehole-image logs to correlate curvature to fracture density in the subsurface. Results from this project show that curvature and fracture density are linearly related.

Theoretical calculations following the bending-plate equations of Manaker et al. (2007) suggest a linear relationship between curvature and strain (assumed fracture intensity). I cross-plotted damage intensities against curvature calculations from numerical simulations done by Busetti (2009) and found a linear correlation between assumed fractures and curvature (Fig. 11). Both theoretical calculations and results from Busetti (2009) indicated that in my experiments and subsurface analyses, fracture densities would be linearly related to curvature.

In clay-model experiments, results showed strong linear relations between fracture intensities and curvature (Fig. 19). These results suggest that curvature was the primary factor in fracture generation in the clay models in controlled, laboratory settings. Assuming results from clay models show fracture patterns similar to real rocks as suggested by Reches (1988), then clay-model results imply that curvature and fracture intensity are linearly related when subsurface deformation involves basement reverse faulting or layer extension.

Horizontal wellbores were important in the study because they minimized lithology and layer thickness effects in the borehole since they provided thousands of feet of data within the targeted Hunton Group of relatively similar thickness (Fig. 51). Fracture strike (Fig. 22) in Wells 1, 2, 3, 4, and 6 suggest similar fracture-generation mechanisms since principal fracture sets are oriented roughly in the same direction. The strike of the fractures in Wells 5 and 7 are approximately +20° and -50° different from the strike of the principal fracture set in the other wells. From data in Table 7, Well 5 is the best producing well, while Well 7 is the worst producing well.

Different fracture strikes in Wells 5 and 7 suggest that fractures were generated by different fracture mechanisms than the other wells or similar fracture mechanisms occurred in all wells, but local changes in principal-stresses were caused by subsurface geometries. Since the focus of this study was relating fracture density to curvature, it was assumed that the fractures were primarily tensile and were generated by similar processes and local principal stresses varied due to subsurface geometries.

In Figs. 27-31, Euler curvature was compared to curvature calculated from bedding planes in the borehole. Since the curvature values were similar from both 3D-seismic calculations and bedding-planes, correlations between layer curvature and fracture density appear to be indicative of subsurface fracture zones. The similarities between the Euler and bedding-plane curvature also suggest that 3D-seismic curvature is a good indicator of subsurface structures.

Curvature was visually related to fracture density in the wellbores by coloring curvature-strike orientation by azimuth on the k_1 curvature attribute (Fig. 42). The general east-west strike appeared to relate to areas of high fracture density as shown by the arrows in Fig. 42. This result indicated that curvature azimuth was an important factor in determining fracture density in the subsurface. Azimuthal intensity correlations with fracture density in Wells 2 through 7 show linear relationships (Table 5). These same areas in Wells 2 through 7 also showed correlation to k_1 curvature values (Table 6). Linear relationships from both azimuthal intensity and k_1 curvature are similar to results from theoretical calculations, numerical models, and clay models suggesting that curvature is a controlling factor in fracture generation.

The principal curvatures of k_1 and k_2 were used to identify geometric shapes in the subsurface. I classified anticlinal zones as the area between saddle and dome geometries, while synclinal zones were classified as any area between saddle and bowl geometries. Anticlinal zones accounted for 57% of all the fractures while synclinal zones accounted for 43%. The disparity is most likely due to preferential drilling in the tops of anticlines rather than the bottom synclines. However, the area between anticlines and domes accounts for 19% of the fractures while the area between synclines and bowls accounts for 13% of the fractures indicating that fractures are generated in both anticlines and synclines. The flexural-slip model predicts this where both anticlines and synclines have increased extensional strain on the edge of the fold (Fig. 1).

In addition to curvature, lithology and faulting are also related to fractures as shown by the acoustic-impedance inversion and coherence correlations with fracture density. The acoustic-impedance inversion correlation in Wells 4 and 5 could be attributed to higher amounts of dolomite in those wells. Cantrell et al. (2001) indicated that dolomite is more brittle than limestone, which implies that more fracturing would exist in dolomite than in limestone. Wells 4 and 5 have higher acoustic-impedance inversion values than the rest of the wells suggesting a different lithology, which I interpret as more dolomitic.

Well 3 appears to terminate in a highly fractured or potentially faulted area as seen in Fig. 52. Additionally, Well 3 was the only well where fracture density and the coherence attribute exhibited a negative-linear relationship. The coherence attribute shown again in Fig. 52 shows a linear trend of a large fault zone or small-scale fault indicated by a yellow arrow. Since there was no visible offset in the 3D-seismic data, it is assumed that if it is a fault, it is below seismic resolution (Fig. 53).

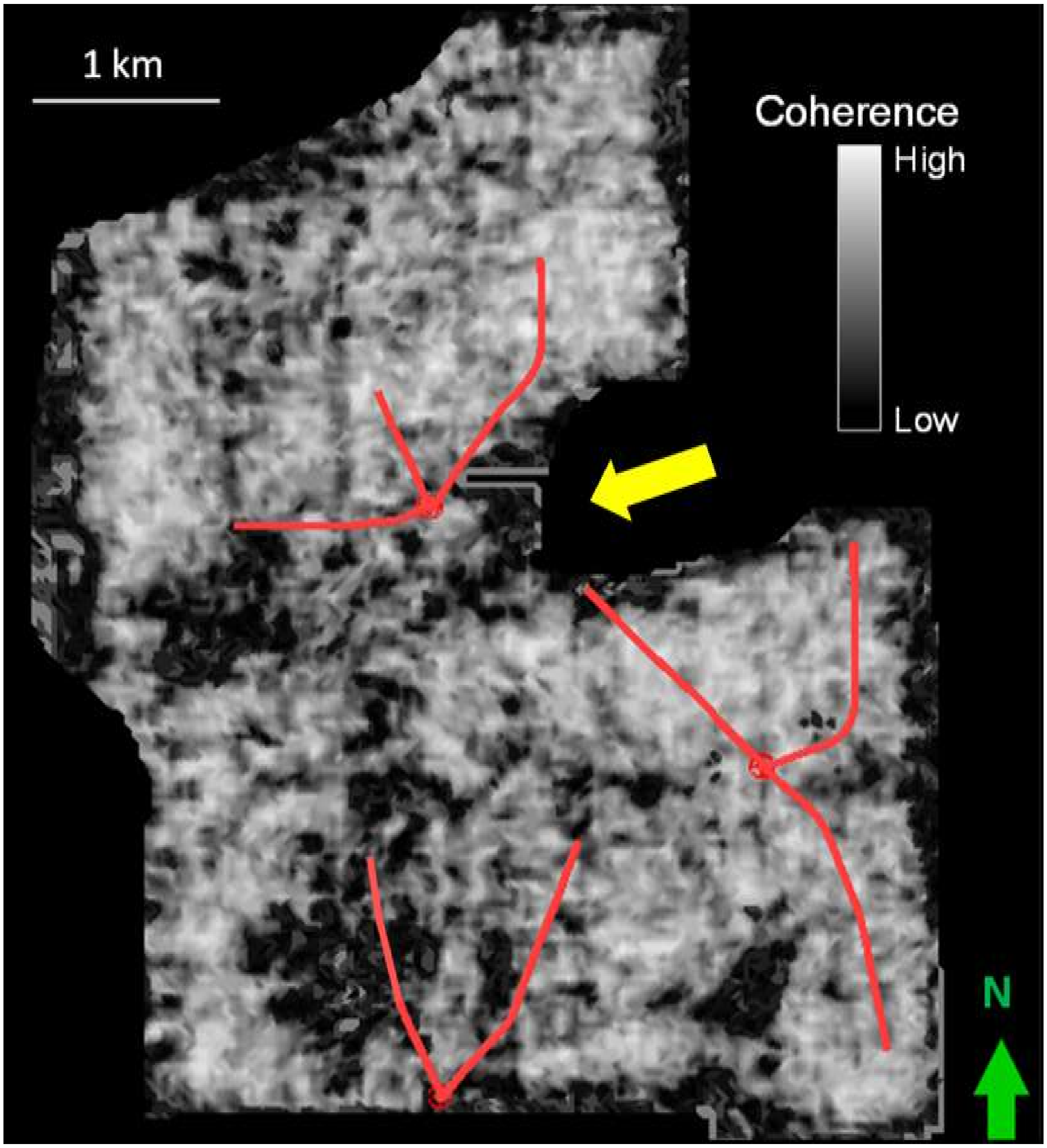

Fig. 52 – Coherence attribute with a yellow arrow indicating the direction of the potential fracture zone/small-scale fault zone.

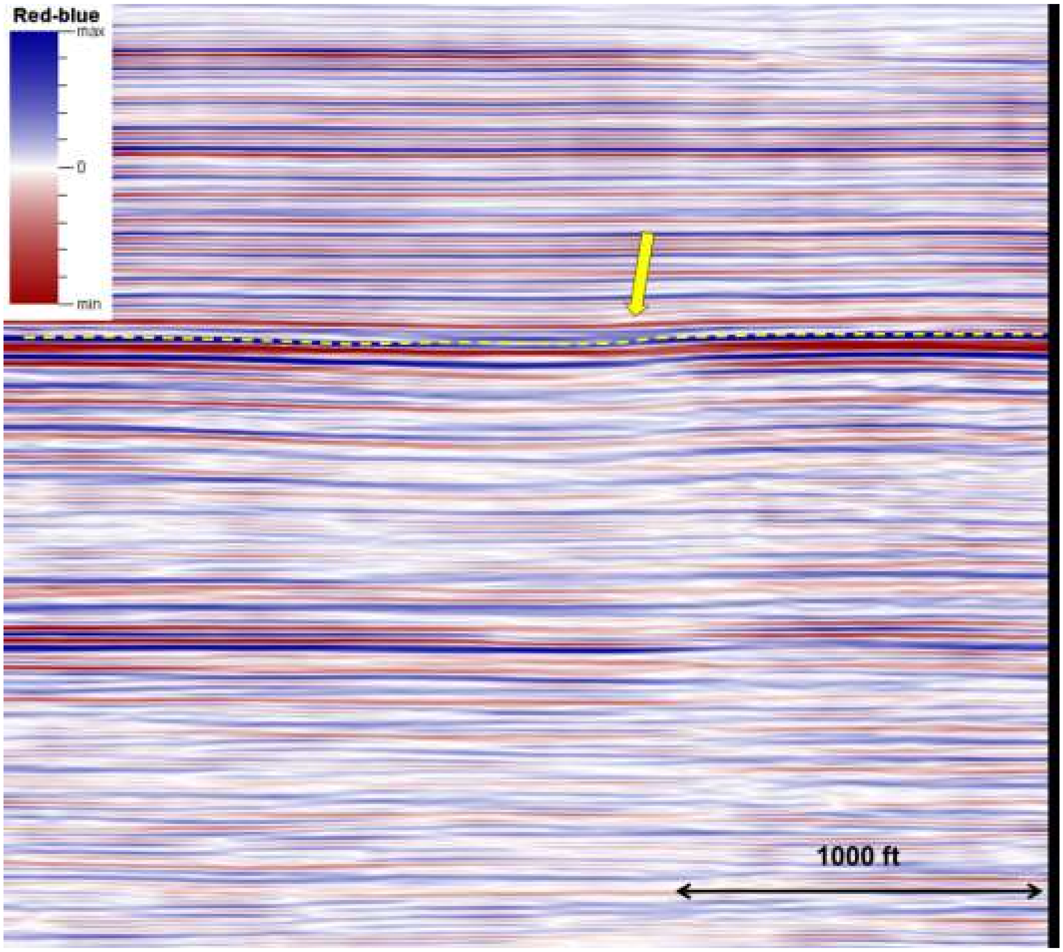

Fig. 53 – Hunton Group horizon in yellow dashed line with area of potential fault zone shown by yellow arrow.

The scaled production data (Table 7) show that Wells 1, 3, 4, and 5 are the best overall producing wells in the study. They all produced nearly 40 bbl of oil or more with Well 1 producing 100 bbl. Wells 3, 4, and 5 produced 40 BOE of gas or more with Well 5 producing 100 BOE. In Well 1, no relationships were seen between fracture density and any other analysis in the study suggesting that fracturing may not play a critical role in hydrocarbon production in this well. However, Well 1 was the only well drilled sub-parallel to the general east-west fracture strike seen in the other wells implying that the well may have been drilled along a single fracture plane. In Wells 3, 4, and 5, correlations existed between curvature and fracture density (Tables 5 and 6). In addition, fracture densities in Wells 4 and 5 correlate with the acoustic-impedance inversion calculations and in Well 3 fracture density correlates with the coherence attribute. These relations suggest that fracturing does play an important role in hydrocarbon-reservoir porosity and permeability.

The results of this study suggest curvature and fracture density are related. Several factors out of my control are limitations to the study. The 3D-seismic data was created from three small surveys which were merged together. Land access and cost constrains resulted in a relatively low fold and narrow azimuth data volume. Edge effects of the seismic were present in the data and overlapped portions of Wells 3, 4 and 5. Some of the raw image-log data in segments of Wells 1, 2, 4, 5, 6 and 7 were unusable because of missing caliper, hole deviation, and relative bearing measurements. Wells 1 and 2 were treated with acid before image logs were acquired potentially removing small fractures from the borehole. Completion technique in the wells is unknown and may have affected production data either positively or negatively. Lastly, the operator indicated that lithology changes between dolomite and limestone affect production with dolomite being more productive than limestone. I tested for lithology in the 3D-seismic survey, but would need core and additional well-log data in order to accurately identify specific changes between dolomite and limestone.

CONCLUSION

I developed a process to identify potential fracture zones from 3D-seismic data. The principal findings are summarized below.

(1) In a laboratory setting, clay-model experiments show strong linear relations between fracture intensity and curvature suggesting that fractures in subsurface structures can be generated by high curvature values.

(2) Curvature calculated from bedding planes in the horizontal-borehole-image logs followed similar patterns as 3D-seismic-curvature calculations. This indicates that 3D-seismic curvature is a strong indicator of subsurface layer structure.

(3) Azimuthal intensity of volumetric curvature related with fracture density in specific zones along the horizontal boreholes. These same areas had relationships between fracture density and k_1 curvature. Relationships between both azimuthal intensity and k_1 curvature in the same areas suggest that fractures are generated by curvature with a specific strike. Identifying this strike indicates where curvature has potentially generated tensile fractures

(4) Relationships between curvature and fracture density from 3D-seismic data and horizontal-borehole-image logs suggest that curvature may serve as a proxy for fracture density in the subsurface.

(5) Lastly, curvature is an important tool to use in subsurface fracture identification as indicated by relationships between fracture densities and curvature values. Furthermore, when other tools such as acoustic-impedance

inversion, coherence, and layer-thickness analyses are used in conjunction with layer curvature, subsurface-fracture identification may be augmented.

REFERENCES

Al-Dossary, S., and Marfurt, K. J., 2006, 3D volumetric multispectral estimates of reflector curvature and rotation: Geophysics, v. 71, p. P41-P51.

Al-Shaieb, Z., Puckette, J., and Blubaugh, P., 2001, The Hunton Group: sequence stratigraphy, facies, dolomitization, and karstification: Oklahoma Geological Survey Circular 105, p. 17 - 29.

Al-Shaieb, Z., and Puckette, J., 2000, Sequence stratigraphy of Hunton Group ramp facies, Arbuckle Mountains and Anadarko Basin, Oklahoma: Oklahoma Geological Survey Circular 101, p. 131 - 137.

Bergbauer, S., 2007, Testing the predictive capability of curvature analyses, *in* Jolley, S.J., Barr, D., Walsh, J.J. and R.J. Knipe, eds., Structurally complex reservoirs: Geological Society (London) Special Publication 292, p. 185 - 202.

Bergbauer, S., Mukerji, T., and Hennings, P., 2003, Improving curvature analysis of deformed horizons using scale-dependent filtering techniques: AAPG Bulletin, v. 87, p. 1255 - 1272.

Bergbauer, S., and Pollard, D., 2003, How to calculate curvatures of geological surfaces: Journal of Structural Geology, v. 25, p. 277 - 289.

Busetti, S., 2009, Fracturing of layered reservoir rocks, Ph.D. dissertation, University of Oklahoma, Norman, 272 p.

Chopra, S., and Marfurt, K. J., 2010, Integration of coherence and volumetric curvature images: The Leading Edge, v. 29, p. 1092 - 1107.

Chopra, S., and Marfurt, K. J., 2008, Emerging and future trends in seismic attributes: The Leading Edge, v. 27, p. 298 - 318.

Chopra, S., and Marfurt, K. J. 2007, Seismic attributes for prospect identification and reservoir characterization: Tulsa, Oklahoma, Society of Exploration Geophysicists, 464 p.

Cloos, E., 1968, Experimental analysis of Gulf Coast fracture patterns: AAPG Bulletin, v. 52, p. 420 - 444.

Davogustto, O., 2011, Removing footprint from legacy seismic data volumes, M.S. Thesis, University of Oklahoma, Norman, (in prep).

Eisenstadt, G., and Sims, D., 2005, Evaluating sand and clay models: Do rheological differences matter?: Journal of Structural Geology, v. 7, p. 1399 - 1412.

Einstein, H. H., and Dershowitz, W. S., 1990, Tensile and shear fracturing in predominately compressive stress fields – a review: Engineering Geology, v. 29, p. 149-172.

Elmohandes, S. –E., 1981, The central European graben system: rifting imitated by clay modelling: Tectonophysics, v. 73, p. 69-78.

Engelder, T., Gross, M.R., Pinkerton, P., 1997, An analysis of joint development in thick sandstone beds of Elk Basin Anticline, Montana-Wyoming, *in* Hoak, T. E., Klawitter, A. L. and P. K. Blomquist, eds., Fractured reservoirs: characterization and modeling: Rocky Mountain Association of Geologists, p. 4-21.

Ericsson, J. B., H. C. McKean, and R. J. Hooper, 1998, Facies and curvature controlled 3D fracture models in a Cretaceous carbonate reservoir, Arabian Gulf, *in* G. Jones, Q. J. Fisher, and R. J. Knipe, eds., Faulting, fault sealing and fluid flow in hydrocarbon reservoirs: Geological Society (London) Special Publication 147, p. 299 - 312.

Fischer, M. P., and Wilkerson, M. S., 2000, Predicting the orientation of joints from fold shape: Results of pseudo three-dimensional modeling and curvature analysis: Geology, v. 28, p. 15 - 18.

Gibbs, A. D., Jaffri, F., and Murray, T., 1997, New techniques for fracture distribution and prediction from kinematic modeling of 3-D strain fields (abstract): AAPG Annual Meeting Program, v. 6, p. 40.

Gross, M.R., Fischer, M.P., Engelder, T., and Greenfield, R.J. 1995, Factors controlling joint spacing in interbedded sedimentary rocks; integrating numerical models with field observations from the Monterey Formation, USA, *in* Ameen, M. S. ed., Fractography: fracture topography as a tool in fracture mechanics and stress analysis: Geological Society (London) Special Publication, v. 92, p. 215-233.

Guo, Y., Zhang, K, Marfurt, K.J., 2010, Seismic attribute illumination of Woodford Shale faults and fractures, Arkoma Basin, Oklahoma: 80th Annual International Meeting, Society of Exploration Geophysicists, Expanded Abstracts, p. 1372-1375.

Handin, J., Friedman, M., Logan, J. M., Pattison, L. J., and Swolfs, H. S., 1972, Experimental folding of rocks under confining pressure; buckling of single-layer rock beams: Geophysical Monograph, v. 16, p. 1-28

Hart, B. S., 2006, Seismic expression of fracture-swarm sweet spots, Upper Cretaceous tight-gas reservoirs, San Juan Basin: AAPG Bulletin, v. 90, p. 1519 - 1534.

Hennings, P. H., Olson, J. E., and Thompson, L. E., 2000, Combining outcrop data and 3-D structural models to characterize fractured reservoirs with outcrop fracture and fault data for reservoir characterization: AAPG Bulletin, v. 84, p. 830 - 849.

Hildebrand-Mittelfeldt, N., 1979, Deformation near a fault termination, Part I. A fault in a clay experiment: Tectonophysics, v. 57, p. 131-150.

Hunt, L., Reynolds, S., Brown, T., Hadley, S., Downton, J., and Chopra, S., 2010, Quantitative estimate of fracture density variations in the Nordegg with azimuthal AVO and curvature: A case study: The Leading Edge, v. 29, p. 1122 - 1137.

Jamison, W. R., 1997, Quantitative evaluation of fractures on Monkshood Anticline, a detachment fold in the foothills of western Canada: AAPG Bulletin, v. 81, p. 1110 - 1132.

Ji, S., Zhu, Z., and Wang, Z., 1998, Relationship between joint spacing and bed thickness in sedimentary rocks: effects of interbed slip: Geology Magazine, v. 135, p. 637-655.

Lisle, R. J., 1994, Detection of zones of abnormal strains in structures using Gaussian curvature analysis: AAPG Bulletin, v. 78, p. 1811 - 1819.

Cantrell, D. L., Swart, P. K., Handford, R. C., Hendall, C. G., and Westphal, H., 2001, Geology and production significance of dolomite, Arab-D reservoir Ghawar Field, Saudi Arabia: GeoArabia, v. 6, p. 45-59.

Manaker, D. M., Turcotte, D. L., and Kellogg, L. H., 2007, Damage formation associated with bending under a constant moment: Tectonophysics, v. 433, p. 81-95.

Mitra, S., and Islam, Q. T., 1994, Experimental (clay) models of inversion structures: Tectonophysics, v. 230, p. 211 - 222.

Murray, G. H., 1968, Quantitative fracture study – Sanish Pool, McKenzie County, North Dakota: AAPG Bulletin, v. 52, p. 57 - 65.

Narhari, S. R., Al-Kandari, A. L., Kidambi, V. K., Al-Ashwak, S., Al-Qadeeri, B., and Pattnaik, C., 2009, Understanding fractures through seismic data: North Kuwait case study: The 79th Annual International Meeting of the Society of Exploration Geophysicists, Expanded Abstracts, v. 28, p. 547 - 551.

Narr, W., and Suppe J., 1991, Joint spacing in sedimentary rocks: Journal of Structural Geology, v 13, p. 1037-1048.

Nissen, S. E., Carr, T. R., Marfurt, K. J., and Sullivan, E. C., 2009, Using 3-D seismic volumetric curvature attributes to identify fracture trends in a depleted Mississippian carbonate reservoir: Implications for assessing candidates for CO^2 sequestration, *in* M. Grobe, J. C. Pashin, and R. L. Dodge, eds., Carbon dioxide sequestration in geological media—State of the science: AAPG Studies in Geology 59, p. 297 - 319.

Northcutt, R. A., Johnson, K. S., and Hinshaw, G. C., 2001, Geology and petroleum reservoirs in Silurian, Devonian, and Mississippian rocks in Oklahoma: Oklahoma Geological Survey Circular 105, p. 1-15.

Northcutt, R.A., 2000, History of oil and gas exploration and development in Oklahoma: Oklahoma Geological Survey Special Publication 2000-2, p. 9 -19.

Reches, Z., 1988, Evolution of fault patterns in clay experiments: Tectonophysics, v. 145, p. 141-156.

Rottman, K., 2000, Defining the role of Woodford-Hunton depositional relationships in Hunton stratigraphic traps of western Oklahoma, *in* K.S. Johnson, ed., Platform carbonates of the southern midcontinent: Oklahoma Geological Survey Circular 101, p. 139 - 146.

Schultz-Ela, D. D., and Yeh, J., 1992, Predicting fracture permeability from bed curvature, *in* J. R. Tillerson and W. R. Wawersik, eds., 33rd U.S. symposium on rock mechanics: Santa Fe, New Mexico, A.A. Balkema, p. 579 - 589.

Singleton, S., and Keirstead, R., 2011, Calibration of prestack simultaneous impedance inversion using rock physics: The Leading Edge, v. 30, p. 70-78.

Stanley, T. M., 2001, Stratigraphy and facies relationships of the Hunton Group, northern Arbuckle Mountains and Lawrence Uplift, Oklahoma: Oklahoma Geological Survey Guidebook, v. 33, 73 p.

Stearns, D. W., 1968, Certain aspects of fractures in naturally deformed rocks, *in* R. E. Rieker, ed., National Science Foundation advanced science seminar in rock mechanics: Special report, Bedford, Massachusetts, Air Force Cambridge Research Laboratories, p. 97 - 118.

Van der Pluijm, B., and Marshak, S., 2004, Earth Structure, New York, WW Norton & Company, 672 p.

Weinberger, R., Reches, Z., Eidelman, A., and Scott, T.E., 1994, Tensile properties of rocks in four-point beam tests under confining pressure, *in* P. P. Nelson, S.E. and Laubach, eds., Rock mechanics models and measurements: challenges from industry; proceedings of the 1st North American Rock Mechanics Symposium, the University of Texas at Austin, Brookfield, Vermont, Rotterdam, p. 435 - 442.

Withjack, M. O., and Jamison, W.R., 1986, Deformation produced by oblique rifting: Tectonophysics, v. 126, p. 99 - 124.

Wu, H., and Pollard, D. D., 1995, An experimental study of the relationship between joint spacing and layer thickness: Journal of Structural Geology, v. 17, p. 887 - 905.

APPENDICES

APPENDIX A: CLAY MODELING

CLAY MODEL ANALYSIS

Multiple structural studies use wet-clay models (e.g., Cloos, 1968; Elmohandes, 1981; Withjack and Jamison, 1986) to imitate tectonic movements in the Earth. Eisenstadt and Sims (2005) showed that it is best to use clay when modeling layer bending rather than using sand because when both are bent, clay folds and fractures while sand creates faults. Mitra and Islam (1994) indicated that clay models are not exact scale models because clay is homogeneous, the strain rate in experiments is higher than natural processes, cohesiveness of clay produces mechanical behavior that does not exactly replicate that of rocks, and boundaries in experiments are free surfaces that result in edge effects. However, because this study focuses on understanding the relationship between curvature and fracture intensity, exact scale models are not important. Rather, it is imperative to understand the process of deformation that leads to fracturing.

CLAY EXPERIMENT FIGURES

Here I show the 15° and 45° ramp sequence of pictures (Figs. 54 and 55). Each sequence begins with the initial-undeformed stage and progresses to the final-deformed stage. The anticline generated in the center of the clay cake in each experiment progressively grows with time as shown by the increased curvature in the center of the laser scan.

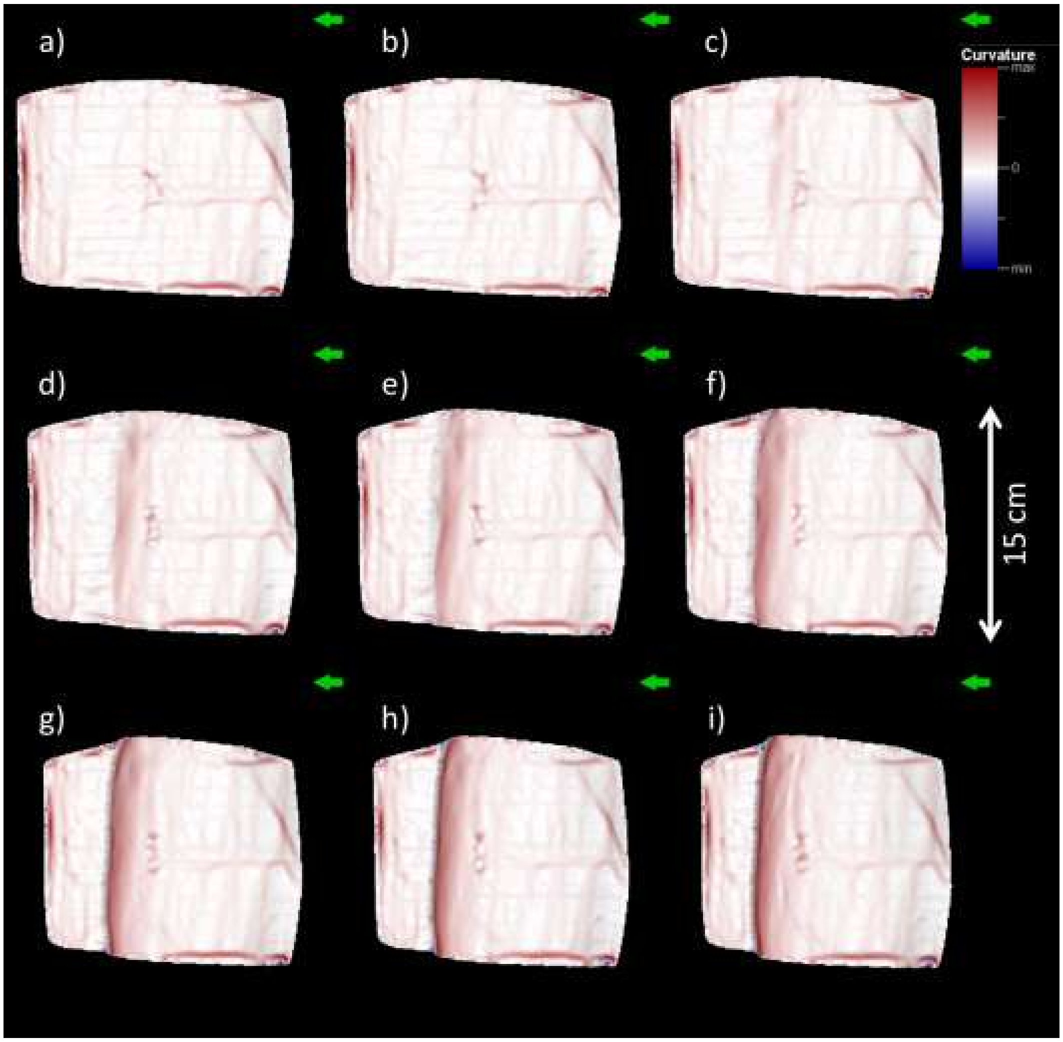

Figure 54 – Most-positive curvature computed from undeformed to final (a, b, c, d, e, f, g, h, and i) of compressional 15° ramp experiment (Fig. 16). Subtle curvature anomalies parallel and perpendicular to the fault correlate to tool marks made in the initial clay model construction. Fracture intensity calculations occurred on the top of the anticline.

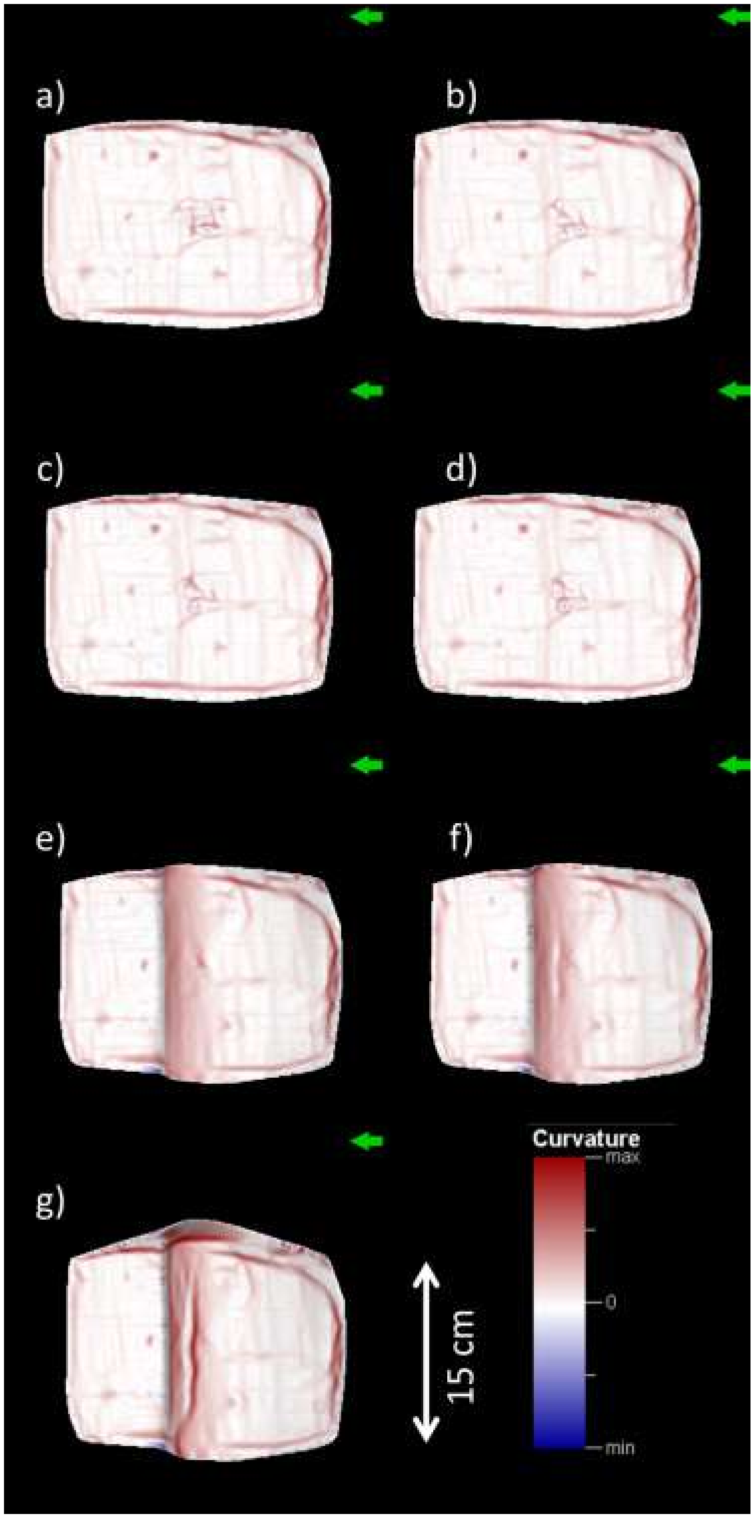

Figure 55 – Most-positive curvature computed from undeformed to final (a, b, c, d, e, f, and g) of compressional 45° ramp experiment (Fig. 16). Subtle curvature anomalies parallel and perpendicular to the fault correlate to tool marks made in the initial clay model construction. Fracture intensity calculations occurred on the top of the anticline.

APPENDIX B: FRACTURE DETECTION

HORIZONTAL-BOREHOLE-IMAGE LOGS

Image-logs are generated when a logging tool with four to six pads moves along the wellbore wall measuring resistivity through the targeted zone (Fig. 56). According to Schlumberger's description of their Formation Micro Imager (FMI) tool, 192 micro-resistivity measurements generate the image in the borehole from special focusing circuitry to ensure currents enter the intended formation. Two main frequencies generate data with low-frequency signals gathering lithological data and high-frequency signals generating images. These data allow vertical and azimuthal resolution as much as 0.2 in (0.5 cm) along the borehole and capture approximately 80% of the borehole in an image. The image-log tool provides an "unwrapped" image of the borehole (Fig. 57). Fractures, faults and other planar surfaces that cut through the borehole are viewed in the unwrapped image as a sinusoidal curve (Fig. 58) from which strike and dip direction are derived with the assumption that the tool is oriented correctly. The image log also helps to identify lithology based on resistivity responses (Fig. 58).

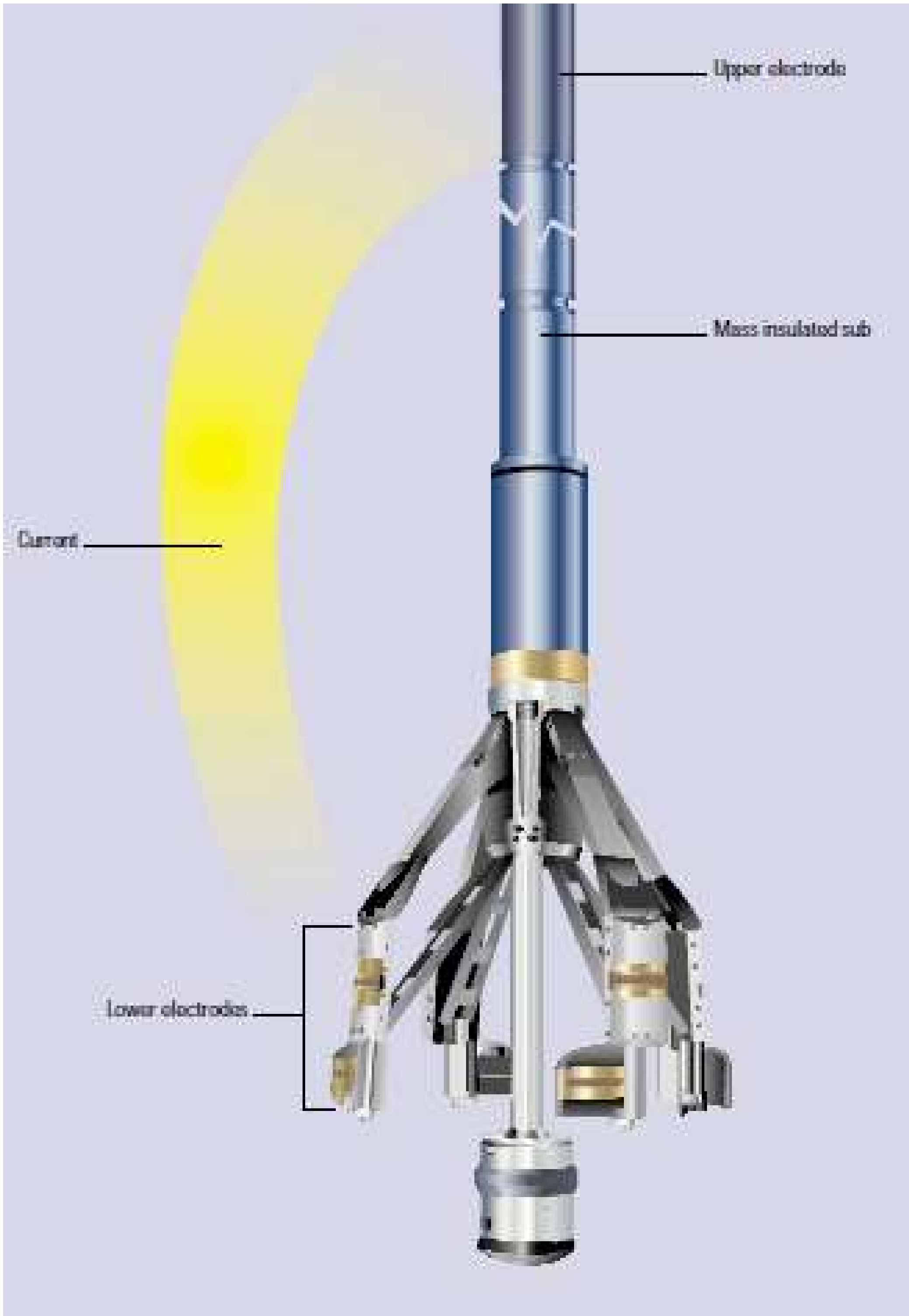

Fig. 56 – FMI logging tool used to generate image logs. This particular tool has 4 pads or lower electrodes that move along the wellbore. Image courtesy Schlumberger.

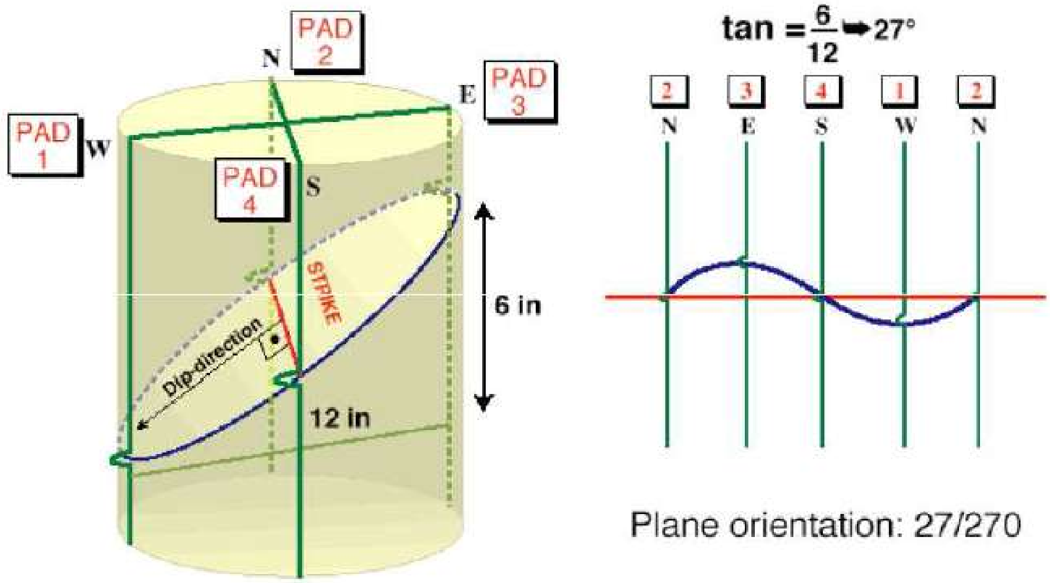

Fig. 57 - Planar feature cuts across the borehole. The "unwrapped" image appears as a sinusoid (right). Using the orientation of the borehole, strike and dip can be calculated. Image courtesy Schlumberger

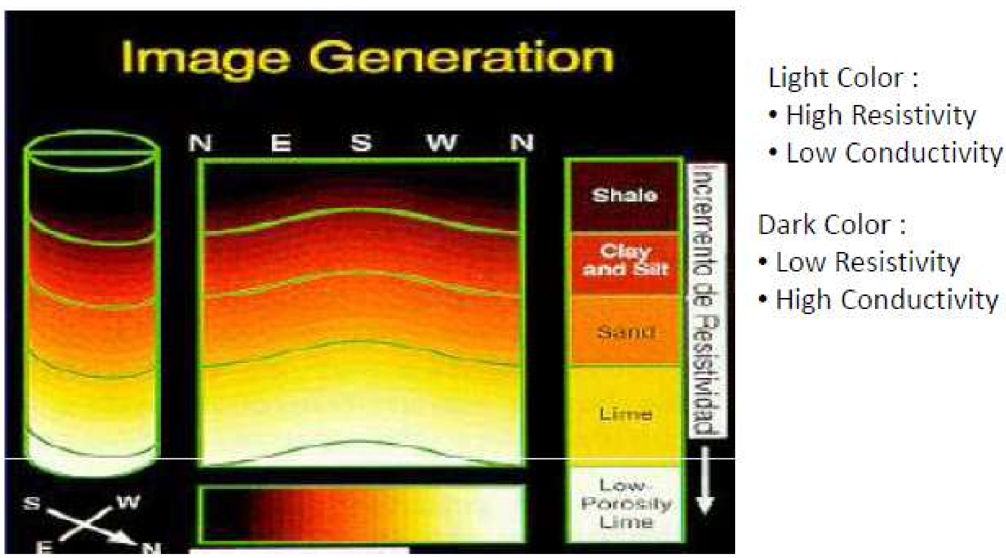

Fig. 58 – Resistivity in image log. High resistivity corresponds to lighter colors and lithologies such as limestones, while lower resistivity is associated with darker colors and shale and silt lithologies. The horizons dip to the north . Image courtesy Schlumberger.